Cavity optomechanics with optically trapped particles

A DISSERTATION PRESENTED
BY
PAU MESTRES JUNQUE
TO
ICFO-THE INSTITUTE OF PHOTONIC SCIENCES

IN PARTIAL FULFILLMENT OF THE REQUIREMENTS
FOR THE DEGREE OF
DOCTOR OF PHILOSOPHY
IN THE SUBJECT OF
PHOTONICS

SUPERVISOR: PROF. ROMAIN QUIDANT

UNIVERSITAT POLITECNICA DE CATALUNYA
BARCELONA, CATALUNYA
MAY 2017

Abstract

Optical trapping and manipulation have emerged as powerful tools to investigate single microscopic objects in a controlled environment. Using the momentum carried by light, forces can be exerted to confine and manipulate objects in a wide range of conditions ranging from liquid environments to high vacuum. In this thesis I implement different optical manipulation schemes to trap nano-objects and coupled them to optical cavities, giving rise to a cavity optomechanical interaction between the trapped object and the cavity mediated by the light's radiation-pressure.

In a first experiment I implement a mobile optical tweezer (MobOT) with nanometer precision to place a levitated silica nanosphere at the standing wave of a high Finesse Fabry-Perot cavity aiming to cool its center of mass motion to the ground state at room temperature. To attain this goal I design a two step cooling process that starts with a parametrical modulation of the optical trapping potential which pre-cools the center of mass motion along the three axis. Then driving the cavity with a red-detuned laser furthers cool the particle motion along the cavity axis via the optomechanical interaction. To monitor the particle motion in the optical trap, I implement a highly robust and sensitive detection scheme that collects the trap forward scattered field and sends it to a set of three balanced photodiodes. According to a semiclassical model I present, this approach can resolve the nanoparticle motion down to a single phonon excitation provided a shot noise limited balance detector.

I also study the use of plasmonic nanoapertures as a novel optomechanical system that increases by 10^8 the single photon optomechanical coupling strength between the trapped nanoparticle and the cavity. These experiments are performed in the overdamped regime and result into a large optomechanical interaction that allows direct measurement of dynamical modulation of the trapping potential due to the motion of the trapped object. Different detuning regimes are studied aiming to improve the optical trapping performances at low laser intensities. These findings are supported by finite element simulations.

Finally I have also made use of optical traps to perform non-equilibrium thermodynamic processes with an optically trapped microparticle in a virtual thermal bath. The virtual bath consists of an electrical white noise force. The agreement between the temperatures obtained from equilibrium and non-equilibrium measurements demonstrates the accuracy of this method. Supported by theory and simulations, our experiments highlight the importance of properly choosing the sampling rate and noise bandwidth for the validity of the method. We apply this technique to study non-equilibrium isothermal compression-expansion cycles at different temperatures ranging from room temperature to 3000K. We calculate some thermody-

namic functionals for these processes such as work, heat and entropy. We show that work distributions verify the Crooks fluctuation theorem, and that they fit well to a generalized Gamma Function.

Abstracte

L'atrapament i manipulació òptiques han esdevingut tècniques importants en la investigació d'objectes microscòpics en condicions controlades. Gràcies al moment lineal de la llum, es poden exercir forces per confinar y manipular aquests objectes en un ampli ventall de condicions que van des de líquids a alt buit. En aquesta tesi he implementat diferents tècniques de manipulació òptica per atrapar i acoblar nano-partícules a cavitats òptiques, donant lloc a una interacció optomecànica a traves de la pressió de radiació de la llum.

En un primer experiment he implementat una pinça òptica mòbil amb precisió nanomètrica per tal de posicionar una nano-esfera de SiO_2 a l'ona estacionaria de una cavitat òptica Fabry-Perot d'alta finesa amb l'objectiu de refredar el seu centre de massa fins a l'estat fonamental. Per aconseguir aquest objectiu he dissenyat un procés de refradament en dos passos. Primer aconseguim un pre-refredament de centre de masses en les tres direccions modulant paramètricament el potencial òptic. Després, fent us de la cavitat il·luminada amb un làser desplaçat cap al vermell, aconseguim un refredament addicional en la direcció de l'eix òptic de la cavitat gràcies a la interacció optomecànica. Per registrar el moviment de la partícula a la trampa òptica, implemento un sistema de detecció interferomètrica robust i sensible que recull els fotons dispersats per la nano-partícula i els envia a tres fotodíodes balancejats. D'acord amb un model semiclàssic que presento, aquest mètode es capaç de resoldre el moviment de la nano-partícula fins al nivell de un sol fonó sempre i quan es disposi de detectors amb soroll electrònic inferior al soroll quàntic de la trampa òptica.

També estudio l'ús de nano-apertures plasmòniques com a nou sistema optomecànic que incrementa en un factor 10^8 la força d'acoblament optomecànic d'un sol fotó entre la partícula i la cavitat. Aquests experiments són realitzats en condicions sobre-esmorteïdes i aconsegueixen una interacció optomecánica prou gran com per resoldre la modulació dinàmica del potencial òptic causada pel desplaçament de la partícula atrapada. En aquest sistema estudiem diferents condicions de des-sintonització per tal de millorar el rendiment d'aquestes trampes amb potències de làser baixes. Aquests resultats els contrastem amb simulacions d'elements finits.

Finalment també he fet servir trampes òptiques per estudiar processos termodinàmics fora de l'equilibri amb una micropartícula en un bany tèrmic virtual. Aquest bany tèrmic consisteix en una força electrònica amb un espectre blanc. La concordança entre les temperatures obtingudes a través de mesures en processos d'equilibri i de no-equilibri demostra precisió d'aquest mètode. Amb l'ajuda d'un model analític i de simulacions, els nostres experiments remarquen la importància d'escollir adequadament la freqüència de mostreig i del

soroll per tal de garantir la validesa d'aquest mètode. Fent us d'aquesta tècnica estudiem cicles de compressió i expansió isotèrmics en el no-equilibri a temperatures que van des dels 300K als 3000k. Calculant diferents funcionals termodinàmics com el treball i el calor demostrem que les distribucions de no-equilibri satisfan el teorema de fluctuació de Crooks i que s'ajusten a adequadament a una funció Gamma generalitzada.

Contents

A la meva familia

Acknowledgments

There is many people who deserve my deepest gratitude for going along with me during all these years. First and foremost I want to thank my supervisors Dmitri Petrov and Romain Quidant who guided and supported me during all this period. Learning from their expertise is what allowed me to succeed in my experiments.I feel indebted to Dmitri for accepting me for a summer fellowship in 2010 and giving me my first opportunity to do experimental science. I also thank him for sharing with me his time and passion for the work in the lab and teaching me that sometimes experiments do not work out, and one should not feel too frustrated about it. To Romain I am indebted for giving me the chance to work with his ambitious optomechanics projects as well as his always positive and encouraging support to my decisions. I also greatly benefited from his support to present our work at international conferences, where I could discuss ideas and learn from many experts of our field.

When I started my PhD. at Dmitri's group I was very lucky to share office with a great group people such as Monica Marro and Saurab Raj. Also in the tweezers group I was fortunate to share the most enthusiastic discussions about thermodynamics with the equally talented and unabashed scientists that are Iñaki Martinez, Edgar Roldan and Antonio Ortiz. I shall neither forget the moral support of Raul Rica during all these years, specially during the cursed days of TERS, and his *savoir faire* in all situations.

When I moved to Romain's group I was lucky enough to fall temporarily under the mild supervision of two exceptional postdocs: Marco Spasenovic, who had made the first steps designing the cavity experiment, and Johann Berthelot, who always provided me nice samples to do plasmonic experiments. I am also in deep gratitude to Alexandros Tavernarakis, who taught me everything I needed to know about optomechanics and how to lock high Finesse cavities. To them I owe at least half of my experimental skills.

I would also like to thank the Plasmon-Nano-optics group members and specially Gerard Planes, Vincenzo, Francesco Ricci, Andreas Schell and Irene Alda with whom I worked more tightly, Luis Miguel for his valuable scientific perspective outside the academia and Nadine Meyer who has been brave enough to continue with my experiments and proof read this manuscript.

I also want to express my gratitude to professors Darrick Chang, Simon Groeblacher and Ivan

Favero for serving as experts in my thesis committee.

When things in the lab did not go as expected I could always enjoy the support of my old university friends Linus Manubens, Bernat Espigulé, Jofre Espigulé, Juan Polo, Jaume Alonso, Margarida Triadú, Oriol Tintó, Pau Santos, Xavier Viader, Pau Pulido, Ernest Alzina, Gerard Ariño and Carlos Escorihuela for the annual paellas, Christmas dinners and random beers. I also want to specially thank Nicolas Morell for all these years of hardcore climbing motivation and Oliver Hijano, Eliot Hijano and Jordi Tura for the never-ending nights spent in ELO hell.

I also want to thank my family, without them I would not be where I am. Gràcies pares predicar sempre amb l'exemple, donar-me l'educació que m'ha permés arribar fins aquí i la paciencia durant aquests 28 anys. Gràcies Claudia per ser una bona germana. Gràcies també als avis, tius i cosins per acompanyar-me durant tots aquest anys.

At last but not least I want to thank Clara Bofill for her heartwarming company during all these years. Gràcies per la teva paciencia, amor i comprensió durant tots aquests anys. Les teves paraules m'han ensenyat més de mi mateix del que podria escriure en mil-i-una tesi.

0

Introduction

Understanding nature directly from the study of its building blocks is the main goal of science and its peers. Investigating the simplest systems and combining them to more complex phenomena, gives us the possibility to describe and predict the concepts of nature not only qualitatively but also quantitatively. While we aim to describe systems using the most universal laws, our physical theories have a limited range of applicability. For example classical physics can accurately describe macroscopic systems at room temperature but fails to describe the behaviour of single atoms and systems at extreme low energies. Similarly quantum mechanics describes well the behaviour of systems consisting of few atoms at low temperatures but is impractical to describe macroscopic systems at room temperature. Although a priori this might seem a formal problem, it is a fact is that macroscopic systems do not feature certain quantum effects such as superposition.

The existence of this two distinguishable regimes arises several fundamental questions reminiscent from the Schrödinger's feline *gedankenexperiment* such as do the laws of quantum physics still hold for macroscopic objects? Does gravitation set a limit to quantum effects for large masses? Can we achieve a state superposition of a living organism?

Matter-wave interferometry experiments have shown agreement with the quantum predictions for particles up to 10^4mass units. However, this figure is orders of magnitude lower from where competing theories predict deviations from quantum physics. Extending these experiments to larger masses requires the capability to find larger systems that can work sufficiently decoupled from the environment in order for genuine quantum effects to emerge.

Optomechanical systems consisting of a mechanical resonator coupled to an electromagnetic field are ideal candidates towards manipulation and control of the mechanical motion in the quantum regime. There currently exist many different configurations of optomechanical systems including micro-disks, membranes, cantilevers, etc. Such systems typically operate with mechanical frequencies comprised between kHz $\sim$ GHz and electromagnetic fields from the microwave to the optical regime. A figure of merit that quantifies the decoupling of the mechanical resonator with the environment is the so-called $Q \times f$ product (Q being the mechanical Q-factor and f its frequency). While f can be tuned by the geometry and mode of the resonator, Q is mostly limited by the clamping of the device to its substrate and material losses. As a result, only f $\sim$GHz resonators at cryogenic temperatures have been brought to the mechanical quantum regime, and these remain still limited in terms of the Q needed for some proposals.

Levitated Optomechanics

To suppress clamping losses a recent approach followed by different groups consists on using an optically levitated nanoparticle as a mechanical oscillator. Together with the large detuning of the trapping laser to internal transitions and the frequency mismatch between the lattice modes and the center of mass motion, the predicted $Q \times f \sim 10^{18}$ is so large that allows for ground state cooling at room temperature. Additionally, such all-optical approach already presents a geometry compatible with matter-wave interferometry experiments.

Current efforts towards ground state cooling at room temperature using optically levitated nanoparticles have been split in two approaches: the use of an active feedback and the use of passive cavity cooling. On the one hand the active feedback continuously monitors the

particle position along the three axes and then parametrically modulates the potential at twice the mechanical frequencies to extract energy from the centre of mass motion. On the other hand, the cavity approach relies on trapping a levitated nanoparticle in the cavity standing wave while using a detuned laser to damp its motion along the cavity axis via optomechanical interaction. Although both approaches have shown great potential, due to intrinsic limitations of each method they have been unable to reach ground state.

The main goal of this thesis has been to build an experimental platform that overcomes these limitations aiming to reach and measure the mechanical ground state of an optically levitated nanoparticle. Our approach has consisted on implementing and combining both state-of-the art optomechanical cooling techniques to compensate for each other weaknesses.

Plasmonics and Optomechanics

Despite the clear benefits of this optical levitation approach, combining a microscopic resonator with a macroscopic cavity leads to an intrinsically weak optomechanical coupling strength. Experimentally this is circumvented by using electromagnetic fields with large number of photons in the so-called linearised optomechanical regime. In this regime the mechanical oscillator cannot resolve the individual cavity photons since optical losses are larger than the coupling of a resonator phonon with a cavity photon. As a result this configuration excludes the use of optically trapped particles for single photon cavity optomechanics, where non-linear quantum effects become observable.

To increase the optomechanical interaction of an optically trapped nanoparticle and a cavity we need to shrink the later in order to maximise the ratio between the particle size the cavity mode volume. Recent advances in nano-optics have shown how plasmonic nanostructures can be used to confine optical fields at sub-wavelength scales and used to trap nm-sized objects. However, these plasmonic trap systems have never been characterized from the optomechanics perspective, namely as a mechanical oscillator coupled to an optical resonator.

Therefore plasmonic nano-apertures as a novel geometry for cavity optomechanics with

optically trapped particles have been studied.

Stochastic thermodynamics

Aside from our study of cavity optomechanics, we have used optical tweezers to study non-equilibrium stochastic thermodynamics processes in a liquid environment. Optical traps have been one of the main experimental driving forces in the field of stochastic thermodynamics due to the fact that they only have six mesoscopic degrees of freedom (3 positions and 3 momenta) which are uncoupled. Together with a high position and time resolution, such features allow to accurately measure the energy exchange between the system and the surrounding thermal bath with $\sim k_b T$ resolution. Additionally, the dynamics of an optically trapped particle is analogous to the classical scheme of a piston filled with an ideal gas. As a result optical tweezers emerge as an ideal platform to reproduce heat engines in the micro- and nano-scales.

As for their macroscopic counterparts, microscopic heat engines can convert thermal energy into work by operating between two thermal baths at different temperatures. For the case of water solutions however, fusion and evaporation temperatures set an upper and lower bound to the temperatures of these thermal bath. To extend the upper bound of accessible temperatures of such systems, we have studied the use of additional random forces coupling to the particle centre of mass as an additional heat source for both equilibrium and non-equilibrium processes.

Thesis Outline

The manuscript is organised as follows:

- Chapter 1 covers the fundamental theory of optical trapping. We provide a derivation from first principles of the optical forces acting on a particle and its resulting dynamics. Then we describe how the scattered photons also generate a detection signal which can

be calibrated using different methods. A short overview of the most common optical trapping geometries for micro and nanoparticles is also provided. The basics of this chapter will be used through the thesis.

- Chapter 2 is devoted to the study of random forces as an effective thermal bath. This approach allows to study non-equilibrium stochastic thermodynamic processes at different temperatures in optical traps shedding light into how energy is exchanged on the mesoscale between a single degree of freedom and the bath. The theory related to stochastic thermodynamics is also provided. The main achievements are the demonstration that noise sources with a flat spectrum profile where the system responsivity is high can be considered as thermal baths. This is then used to find the non-equilibrium work distributions for isothermal compressions/expansion in an optical trap.

- Chapter 3 focuses on optically levitated nanoparticles coupled to a Fabry-Perot resonator as a cavity optomechanical system. In the first part of the chapter we give detailed description of the system taking into account the detection and cooling limitations imposed by the standard quantum limit (SQL). In the second part we present the current state of or levitation cavity optomechanics setup aiming to reach and measure ground state in terms of sensitivity and optical cooling rates. We also discuss about the advantages and disadvantages of the different cooling approaches. The main contributions are the construction of a setup that achieves resolved sideband cooling of a particle trapped in an optical tweezer and the design and implementation of mobile optical traps (MobOT)

- Chapter 4 analyses plasmonic nano-cavities as a nanoscale optical trapping system also featuring an optomechanical interaction. Applying previously developed concepts and simulations, we show that such cavity miniaturisation allows to boost the optomechanical coupling strength to unprecedented values and observe optomechanical effects even in the overdamped regime. The main contributions are the demonstration of optomechanical interaction between optically trapped nanoparticle and a

plasmonic nano-cavity with the highest experimental single photon optomechanical coupling rate, allowing to directly measure the modulation of optical potential in a plasmonic nano-cavity.

One repays a teacher badly if one always remains nothing but a pupil.

Friedrich Nietzsche, Thus Spoke Zarathustra

1

Theory of Optical Trapping

The effects of radiation pressure were first reported by the German astronomer Johannes Keppler in 1609[60]. He noticed that comets presented two tails pointing away from the sun: an ion tail carried away by the solar wind and a dust tail pushed by the radiation pressure. Few centuries later, James Clerk Maxwell could demonstrate with his set of equations that "electromagnetic waves exerted a pressure in the direction of propagation equal to the energy contained in that volume". Yet it was not until 1901 that Lebedev experimentally verified its existence using a carefully calibrated torsion balance. Thanks to the discovery of lasers later in the 70's Arthur Ashkin was able to show how to use light's radiation pressure to manipulate matter in a controlled manner[5,6,7]. Using a strongly focused laser beam he was able to trap[6] and accelerate[5] micron sized particles in a liquid environment.

1.1 Introduction

If we want to understand the physical mechanism behind optical traps, then we need to find and characterize the forces exerted by a focused optical beam onto a small particle. We will start by considering a simple analytic model that, based on the dipole approximation, captures most of the properties of optical trapping. Then we will consider a more general description of the optical potential to see when corrections should be considered. Finally we describe the equations of motion and dynamics occurring in optical traps and how these can be used for calibration of the optical potential.

Optical Forces in the Rayleigh and Paraxial Approximations

In this section we present a description of the electromagnetic response of a dielectric nanoparticle followed by its interaction with a focused optical beam. For a more detailed treatment see references[17] and[90].

Polarizability

Matter is formed by discrete electric charges: electrons and protons. When illuminated by an electromagnetic wave at frequency ω, these electric charges are driven into an oscillatory motion by the incident electric field. For a simple atom under the illumination of a monochromatic field polarised along the x axis :

$$\vec{E} = E_o Re\{e^{-i\omega t}\}\vec{u}_x \tag{1.1}$$

e can write the electron equation of motion as a damped harmonic oscillator (Lorentz Model):

$$m\ddot{x} + m\gamma_e\dot{x} + m\omega_o^2 x = -eE \tag{1.2}$$

Where e is the electron charge, m the reduced mass of the electron ($m \approx m_e$), ω_o the frequency of its optical transition and the dissipation term γ_e accounts for the effects that cause decoherence with the driving field (radiation of accelerating charges, absorption, collisions...). Assuming that the electron oscillates with the electric field, the solution of Eqn.(1.2) writes as[17]

$$\text{x(t)} = x_o E_o Re\{e^{-i\omega t}\} \tag{1.3}$$

with

$$x_o = \frac{e/m}{\omega^2 - \omega_o^2 + i\gamma_e\omega} \tag{1.4}$$

The dipole moment of the atom is $\vec{d} = e \cdot x(t)\vec{u}_x$, and since the dipole is field induced, we can rewrite $\vec{d}$ as:

$$\vec{d} = \alpha(\omega)\vec{E} \tag{1.5}$$

where the linear response is accounted by the polarizability $\alpha(\omega)$ is defined as:

$$\alpha(\omega) = \frac{e^2/m}{\omega^2 - \omega_o^2 + i\gamma_e\omega} \tag{1.6}$$

The concept of polarizability can be extended to homogeneous objects larger than single atoms, such a nanoparticle. It only requires the dipole approximation (Eq.1.1) to hold (i.e. particle radius $r_p \ll \lambda$). In this case, the polarizability becomes a magnitude of the bulk material and thus proportional to the volume of the nanoparticle. In the case of a sphere the polarizability writes as[17]:

$$\alpha_o(\omega) = 4\pi r_p^3 \frac{\epsilon_p(\omega) - \epsilon_m(\omega)}{\epsilon_p(\omega) + 2\epsilon_m(\omega)} \tag{1.7}$$

Where $\epsilon_p(\omega)$ and $\epsilon_m(\omega)$ are the frequency dependant permitivities of the particle and sur-

rounding medium respectively. This last expression also assumes that the optical field is far detuned from internal resonances, and the dependence on the frequency comes from the refractive index of the bulk material. As we will see later on, the polarizability is a critical parameter that determines how strong the light-matter interaction is for the nanoparticles we work with.

Stiffness

Now we want to consider the Lorentz force acting on a dipole when the electric field is non-uniform[52]:

$$\vec{F} = (\vec{d} \cdot \nabla)\vec{E} \tag{1.8}$$

For the motion of small dielectric spheres, the fast oscillations of the optical field cannot be resolved. As a result, only the time average force is observed:

$$\langle \vec{F} \rangle = \frac{1}{4} Re[\alpha] \nabla E^2 + \frac{1}{2} Im[\alpha] E^2 \nabla \phi \tag{1.9}$$

where the terms in r.h.s. are the so called gradient and scattering forces respectively.

The gradient force is conservative and points towards the maximum of intensity of the electric field, whereas the scattering force is non-conservative and pushes the particle along the direction of local propagation field vector $\vec{k}$ ($\phi = \vec{k} \cdot \vec{r}$). When dealing with dielectric particles, typically $Im[\alpha_o(\omega)] \approx 0$, thus it becomes necessary to include the electrodynamics correction to account for the de-phasing and interference between the incident and scattered fields[52]. Due to these effects, α differs from its static value α_o[17]:

$$\alpha = \frac{\alpha_o}{1 - (2/3) i k^3 \alpha_o} \tag{1.10}$$

Now we can finally rewrite these two force contributions as as a function of the field intensity:

$$\vec{F}_{grad}(r) = [\frac{2\pi r_p^3}{c}\frac{\epsilon_p - \epsilon_m}{\epsilon_p + 2\epsilon_m}]\nabla\langle I(r)\rangle = \frac{\alpha'}{4}\nabla I_o(r) \tag{1.11}$$

$$\vec{F}_{scat}(r) = [\frac{8\pi}{3c}(k\cdot r)^3 r_p^3\left(\frac{\epsilon_p - \epsilon_m}{\epsilon_p + 2\epsilon_m}\right)^2\langle I(r)\rangle]\nabla\phi = \frac{\alpha''}{2}I_o(r)\nabla\phi \tag{1.12}$$

where we have used the identity $I_o = c\epsilon_o E_o^2/2$. Note that we have written the terms of α explicitly to show the dependences on the r_p and λ.
In our experiments we will mostly use Gaussian beams, which present a Gaussian intensity profile for the intensity:

$$\langle I_o(r,z)\rangle = \frac{2P}{\pi w_o^2(1+(z/z_o)^2)}e^{-\frac{2r^2}{w_o^2(1+(z/z_o)^2)}} \tag{1.13}$$

where P is the optical power in the beam and is related with the intensity at the focus as

$$P = \int_{-\infty}^{\infty}\int_0^{2\pi} I d\rho d\psi = \frac{c\epsilon_o\pi w_o^2 E_o^2}{4} \tag{1.14}$$

Combining Eqs.(1.11, 1.12 and 1.13) we find the following values for the optical forces:

$$F_{grad}(\rho,z) = -\alpha' I_o(\rho)\begin{bmatrix}\frac{r\cdot z_o^2}{w_o^2(z^2+z_o^2)}\\ 0\\ z[(\frac{z}{z_o})^2 + (1-\frac{2r}{w_o})][\frac{z_o^2}{z^2+z_o^2}]\end{bmatrix} \tag{1.15}$$

and

$$F_{scatt}(r,z) = \alpha'' I_o(r)k\begin{bmatrix}(\frac{r}{z(1+(z_o/z)^2)}\\ 0\\ 1+\frac{r^2 z_o^2}{(z^2+z_o^2)^2} - \frac{r^2+2zz_o}{2(z^2+z_o^2)}\end{bmatrix} \tag{1.16}$$

If we consider particle displacements $|r| \ll \lambda$ we can expand the optical potential in

terms of r/λ and keep the leading ones to obtain:

$$F_{grad}(\rho, z) \approx -\begin{bmatrix} \kappa_r & (1 - \frac{2r^2}{w_o^2} - 2\frac{z^2}{z_o^2})r \\ 0 & \\ -\kappa_z & (1 - \frac{4r^2}{w_o^2} - 2\frac{z^2}{z_o^2})z \end{bmatrix} \tag{1.17}$$

$$F_{scatt}(r, z) \approx \frac{\alpha''}{\alpha'}\kappa_z \begin{bmatrix} \mathrm{k}rz \\ 0 \\ \gamma_o + \gamma_z z^2 + \gamma_r r^2 \end{bmatrix} \tag{1.18}$$

where we have defined γ_o, γ_z and γ_r as in [43]:

$$\gamma_o = z_o(z_o k - 1) \tag{1.19}$$
$$\gamma_z = (2 - z_o k)/z_o \tag{1.20}$$
$$\gamma_r = k/2 - 2(z_o - k z_o^2)/w_o^2 \tag{1.21}$$

and

$$\kappa_r = \frac{\alpha' E_o^2}{w_o^2} \tag{1.22}$$
$$\kappa_z = \frac{\alpha' E_o^2}{2 z_o^2} \tag{1.23}$$

are the so called trap stiffness, that characterize the linear restoring constant of the optical potential near the focus.

Discussion

In this derivation we have obtained a simple expression for the forces experienced by an object smaller than the wavelength in a paraxial optical field. These are separated in two contributions: $F_{scat}(r, z)$ pushing the object along the direction of propagation of light, and $F_{grad}(r, z)$ pulling the object towards the maximum of intensity. Consequently achieving a

stable potential requires $|F_{grad}(r,z)| > |F_{scat}(r,z)|$. When this is satisfied the equilibrium position lies along the optical axis and slightly away from the focus due the contribution of the scattering force. For small displacements the object experiences a linear restoring force along each axis with a restoration constant(κ_i) proportional to the optical power and the particle volume. As a result trapping small nanoparticles requires high optical intensities (for example to trap a silica nanosphere of $r \approx 70$nm in air requires about $5 \cdot 10^{10} W/m^2$ that correspond to 140mW of a 1550nm laser in a focal spot of 1μm waist).

Fields Beyond Paraxial Approximation

To achieve $F_{grad}(r) > F_{scat}(r)$ with a single beam optical trap, we need to focus the optical field to a diffraction limited spot, thus the paraxial approximation used to compute the optical forces does not hold. We need a better description of the beam at the focus, which is strongly dependent on the focusing optics and input beam boundary conditions. To describe a strongly focused optical beam we follow the theory of Richards & Wolf[95,128] that consider an aplanatic lens as focusing optics. This focusing optics generates a focal sphere F centred at the origin of coordinates and radius equal to the focal length (f) of the system. In order to get a sharp focus, the lens satisfies the Abbe sine condition:

$$h = f \sin\theta \tag{1.24}$$

which means that each ray that emerges from the focusing optics at height h meets at the focal sphere at the same height (Fig.1.1a). Additionally, each surface of the focusing sphere needs to conserve the intensity (i.e. energy needs to be conserved, Fig.(1.1.b), as a consequence

$$|E_2| = |E_1| \sqrt{\frac{n_1}{n_2} cos\theta} \tag{1.25}$$

where the $E_{1/2}$ and $n_{1/2}$ are the amplitude of the electric field and refractive index of the optics and focal sphere.

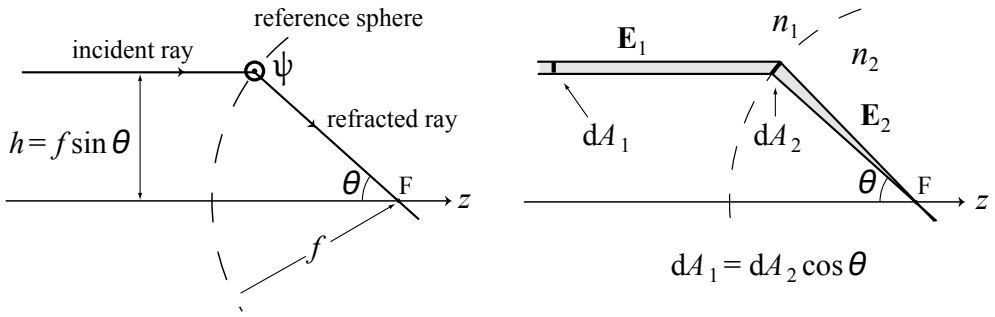

Figure 1.1: Diagrams showing the Abbe sine condition (a) and energy conservation through the focal sphere surfaces (b).

.

Under these assumptions, the focal field can be expressed in an angular representation[90] as

$$E(\rho,\phi,z) = \frac{ikfe^{-ikf}}{2\pi}\int_0^{\theta_{max}}\int_0^{2\pi} E_\infty(\theta,\phi)e^{ikz\cos\theta}e^{ik\rho\sin\theta\cos(\phi-\psi)}\sin\theta d\phi d\theta \quad (1.26)$$

Where θ_{max} represents the maximum collection angle of the lens (NA=$n_2\sin\theta_{max}$) and $E_\infty(\theta,\phi)$ represents the incoming field in spherical coordinates. In the experiments the incoming field has a waist diameter larger than the entrance pupil of the focusing optics (i.e. we will overfill the focusing lens), thus we can approximate E_∞ as a plane wave polarised along the x direction:

$$E_\infty(\theta,\phi) = E_0\frac{1}{2}\begin{bmatrix}(1+\cos\theta)-(1-\cos\theta)\cos 2\phi)\\ -(1-\cos\theta)\sin 2\phi\\ -2cos\phi\sin\theta\end{bmatrix}\sqrt{\frac{n_1}{n_2}\cos\theta}$$

Figure (1.2) shows an intensity map of E^2 along the zy and xy planes for a strongly focused Gaussian beam polarised along the x direction. We see that the focus spot can be well approximated with a Gaussian profile having a larger width along the polarization axis. Therefore the degeneracy in the radial optical forces that was found in the paraxial limit breaks. As a result each axis now experiences a different restoring force, bringing 3 decoupled harmonic oscillators (one for each axis) into a single trap. Still, the x, y axis frequency degeneracy could be

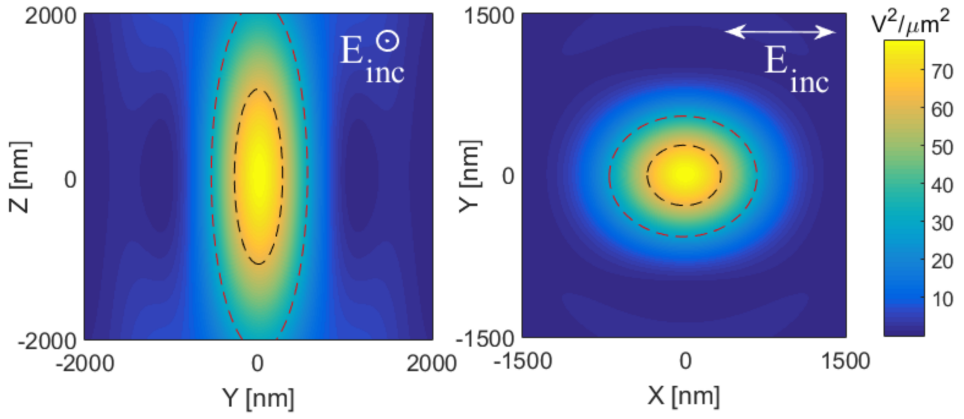

Figure 1.2: E^2 maps of a tightly focused Gaussian beam in the zy (left) and yz (right) planes. The input beam is linearly polarized along x, has a wavelength λ=1500nm and is focused using a 0.8NA lens. The black and red dashed lines represent an intensity decay $2/e$ and $1/e$ respectively for a Gaussian approximated field. Note the elongation of the beam waist along the polarization axis x.

.

recovered by using an input field with rotational symmetry such a circularly polarized beam. Additionally we find that in the focus, the field presents polarization vectors point in all directions (Eq.(1.26)) due to the large angle of several of the incident rays.

Discussion

We have found the expression that describes the field profile of an optical beam focused by a high NA optical system. Despite the accuracy of this model, trying to describe the focus of an beam from first principles is not the best approach. First it can be difficult to know the phase profile of the beam impinging on the focusing optics and then it is very complicated to describe accurately the geometry of the focusing optics (specially if working with commercial objectives). For this reason, the best approach to describe the field at the focus consists on experimentally finding the optical restoring constants (κ_x, κ_y and κ_z) along each axis and fitting them to a modified version of Eqn.(1.22) that takes account the waist asymmetry along

each axis:

$$\kappa_x = \frac{\alpha' E_o^2}{w_x^2} \tag{1.27}$$

$$\kappa_y = \frac{\alpha' E_o^2}{w_y^2} \tag{1.28}$$

$$\kappa_z = \frac{\alpha' E_o^2}{2 z_o^2} \tag{1.29}$$

Then, we can reconstruct the intensity profile of our field at the focus as an elliptically asymmetrical Gaussian beam:

$$\langle I(x,y,z)\rangle = \frac{2P}{\pi w_x w_y (1+(z/z_o)^2)} e^{-\frac{2x^2}{w_x^2(1+(z/z_o)^2)} - \frac{2y^2}{w_y^2(1+(z/z_o)^2)}} \tag{1.30}$$

Mie Scattering Theory

As we have seen, trapping nanoparticles requires high optical intensities, which often generate heat and convection. This is problematic for applications such as single molecule manipulation, the study of stochastic thermodynamics[83], trapping of photosensitive colour centres[41] and even trapping of living cells[119,84]. Therefore, in many cases it will be convenient to work with bigger particles in order to be able to use lower optical powers. However, as particles reach sizes $r \approx \lambda/2$ the dipole approximation used to describe our system breaks. In this cases we will need a more general theory to describe the optical forces acting on particles of arbitrary size.

The most general approach to describe the forces between an optical field and an object

is based on the momentum conservation law, that satisfies the following equation[90]:

$$\frac{(dP_{mec} + P_{field})_\alpha}{dt} = \int_{vol} \sum_\beta \frac{\partial}{\partial \beta} T_{\alpha\beta} = \int_A \sum_\beta T_{\alpha\beta} \cdot \vec{n}_\beta dA \tag{1.31}$$

where

$$T_{\alpha\beta} = \epsilon_o [E_\alpha E_\beta + c_\alpha^2 B_\beta - \frac{1}{2}(E \cdot E + c^2 B \cdot B)\delta_{\alpha\beta}] \tag{1.32}$$

is the Maxwell stress tensor, that accounts for the interaction between the electromagnetic forces and mechanical momentum. Time averaging Eqn. (1.31) over one period of the electromagnetic wave, the change in the incident field momentum vanishes, thus we finally obtain:

$$\langle F_{mech} \rangle = \int_A \langle \sum_\beta T_{\alpha\beta} \cdot \vec{n}_\beta \rangle dA \tag{1.33}$$

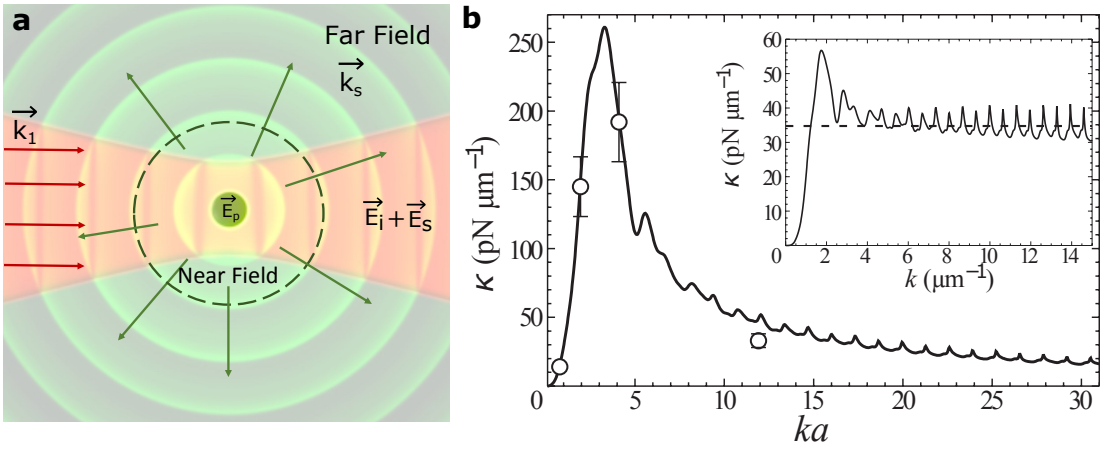

Figure 1.3: Mie scattering of an optically trapped particle . (a) The $\vec{E}_i$ incoming field is scattered by the particle into the $\vec{E}_s$ scattered field. The field inside the particle becomes $\vec{E}_p$. The far field consists on the superposition of the incoming and scattered fields $\vec{E}_i + \vec{E}_s$.(b)Transverse trap stiffness (κ) as function of $k \cdot a (= \frac{2\pi a}{\lambda})$ for a fixed wavenumber $k = 7.8\mu$m in a diffraction limited optical trap using 60mW of power. The solid line corresponds to theoretical results using the Mies scattering partial-wave expansion and circles to experimental values. Inset corresponds to transverse trap stiffness as a functioon of k for a fixed radius $a = 2\mu$m. At large values of $k \cdot a$ the stifness values oscillate due to optical resonances appearing inside the sphere. Figure adapted from[79].

This last expression together with Eq.(1.32) show that optical forces can be computed by knowing the fields at any surface surrounding the material (as long as the material is not de-

formed). This fields need to be self consistent (i.e. we need to compute the field resulting from the superposition the incident and scattered fields $E = E_i + E_s$ and $B = B_i + B_s$). The computation can be done following the procedure of Mazolli et al.[79], which considered it as a Mie scattering field problem. Briefly, one first should expand the incident wave in a set of vector spherical harmonics which are associated to the electric and magnetic multipole fields. Then, using the incident fields and the boundary conditions at the surface of the sphere one computes the coefficients for the scattered field in the same spherical harmonic basis. The first coefficient is the one computed under the dipole approximation, and as particle size increases one needs to compute more coefficients to obtain the correct field. Finally, one can compute the field superposition, to obtain the Maxwell stress tensor and the optical forces[57].

Discussion

In this section we have presented a general theory that describes the optical forces experienced by particles of arbitrary size in an optical field. Despite Mie scattering theory is significantly more complex than the analytical expression of the dipole approximation we obtain an important similarity: for small displacements from the centre of the trap, the particle experiences a linear restoring force along each axis. However, the dependence of κ_i with the particle size shows important differences.

Fig.(1.3b) shows the transverse trap stiffness for different wavelengths and particle radius as computed by as Mazolli et al[79]. As predicted from the dipole approximation, the stiffness κ_i at fixed power grows with the particle size up to $r_p \approx \lambda/2$. Conversely, when the particle size is comparable to the wavelength ($r_p \sim \lambda/2$), κ decreases with the particle size due to the influence of higher order Mie scattering terms. This leads to the fact that for an efficient optical trap one should avoid working with particle sizes larger than λ. Interestingly for very large particle sizes ($r \gg \lambda$), the stiffness shows a periodic resonance profile every multiple of $\lambda/4$ due to the appearance of whispering gallery modes inside the sphere.

Dynamics in the Optical trap

The motion of a particle confined in the harmonic regime of the optical potential can be described for each axis with an independent Langevin equation of the form (conveniently, we will write all the equations for the x axis, which then can be straightforwardly generalised to y and z):

$$m\frac{d^2x(t)}{dt^2} + \gamma_m\frac{dx(t)}{dt} + \kappa_x x(t) = \xi(t) \tag{1.34}$$

where γ_m is the viscous drag from the surrounding environment and $\xi(t)$ represents the random kicks from the thermal environment, which are modelled as a Gaussian White noise whose variance satisfies the fluctuation-dissipation theorem:

$$\langle \xi(t) \rangle = 0 \tag{1.35}$$

$$\langle \xi(t)\xi(t') \rangle = 2\gamma_m k_b T \delta(t - t') \tag{1.36}$$

with T the temperature of the thermal bath and k_b the Boltzmann constant.

It is also useful to define the following quantities of the oscillator:

$$\Gamma = \frac{\gamma_m}{m} \quad \text{Dissipation rate} \tag{1.37}$$

$$\Omega_m = \sqrt{\frac{\kappa}{m}} \quad \text{Mechanical frequency} \tag{1.38}$$

In the course of our experiments the mass is a direct property of the trapped particle whereas γ_m depends on environment properties, and should be computed in a specific manner depending on the regime we are working in.

We will always work in two well differentiated regimes: the so called overdamped regime

and underdamped (inertial) regime. We consider the system to be overdamped when $\Gamma \gg \Omega_m$ (i.e. the dissipation rate is higher than the mechanical frequency) and underdamped when $\Gamma \ll \Omega_m$.

For an overdamped system,γ should be calculated according to Faxen's Law[11], which describes the damping at low Reynolds number and takes into account the hydrodynamic effect of nearby surfaces. For a sphere this is

$$\gamma_m \approx \frac{6\pi\eta r_p}{1 - \frac{9}{16}(\frac{r_p}{h}) + \frac{1}{8}(\frac{r_p}{h})^3 - \frac{45}{256}(\frac{r_p}{h})^4 - \frac{1}{16}(\frac{r_p}{h})^5 + O((\frac{r_p}{h})^6)} \tag{1.39}$$

Where η is the viscosity of the fluid and h the distance from it's centre to the surface.

On the other hand, in the underdamped regime, γ is computed using Kinetic gas theory[12], where the damping is expressed as a function of the surrounding gas pressure:

$$\gamma_m = 6\pi\eta r_p \frac{0.619}{0.619 + Kn}(1 + c_k) \tag{1.40}$$

where $Kn = \lambda_{fp}/a$ is the Knudsen number, $\lambda_{fp} = (\eta/P)(\sqrt{\pi k_b T 2m})$ the mean free path of the gas molecules and $c_k = 0.31Kn/(0.785 + 1.152Kn + Kn^2)$ is a correction factor that becomes relevant at pressures.

Overdamped Regime

In the overdamped regime, the viscous dissipation in the system is so large that the particle never oscillates allowing us to us to drop the intertia term and rewrite the equation of motion as:

$$\gamma_m \frac{dx(t)}{dt} + \kappa x(t) = \xi(t) \tag{1.41}$$

which corresponds to a diffusion equation in the harmonic potential. The solution of this stochastic differential equation is[39]:

$$x(t) = x(0)e^{-\kappa t/\gamma_m} + \sqrt{\frac{k_b T}{\gamma_m}} \int_0^t e^{t-t'} \xi(t) dW(t) \tag{1.42}$$

where $dW(t)$ is the so called Wiener process[39].
For a deterministic or Gaussian distributed initial condition, $x(t)$ follows a Gaussian distribution, described by its mean and variance. The mean position of the particle respect to the centre of the trap in the general case of an applied external force F_{ext} is:

$$0 = \langle F_{ext} + \xi(t) + \kappa x + \gamma \dot{x} \rangle = \langle F_{ext} + \kappa x \rangle \longrightarrow \langle x(t) \rangle = -\langle \frac{F_i(t)}{\kappa} \rangle \tag{1.43}$$

The variance on the other hand can be obtained via the equipartition theorem as:

$$\langle x^2(t) \rangle = \frac{k_b T}{\kappa} \tag{1.44}$$

Finally to characterize the overdamped regime it is also useful to compute the Power Spectral Density (PSD) of x defined as $X(f) = \int_{-\infty}^{\infty} x(t) e^{i2\pi f t} dt$, that yields:

$$|X(f)|^2 = \frac{k_b T/\gamma_m}{2\pi^2 (f_c^2 + f^2)} \tag{1.45}$$

where $f_c = \kappa/(2\pi\gamma_m)$ is the so called cutoff frequency. Note that in this case, the mass does not play any role in the dynamics of the position.

Discussion

All optical trapping experiments in liquid take place the overdamped regime, as well as trapping experiments in air at atmosphere pressure. Working in the overdamped regime significantly simplifies the analytical description of the system, specially while studying thermodynamic processes in optical traps[110,32,76]. From the experimental point of view, working in the overdamped regime allows to study systems where the trapped object quickly equilibrates with the environment at a rate given by f_c, which can reach up to some kHz. Thus, by virtue of Eq. (1.43), we can measure low frequency forces with up to kHz in real time by measuring the average displacement of the trapped object from the centre of the trap. This is the principle behind the photonic force microscope[3] and also the reason why the biophysics community has been using optically trapped particles as force probes for single molecule experiments[16,75].

Underdamped regime

In the underdamped regime, trapped particles are able to oscillate due to the low dissipation of the environment. This is achieved by trapping particles in air and pumping the system to vacuum. In this case it is convenient to solve the equation of motion (Eq. 1.34) in the frequency space considering a monochromatic driving force $F(t) = F_o \sin(\Omega t)$ instead of $\xi(t)$. Using an ansatz of the form $x(t) = A \sin(\Omega t + \phi)$, we obtain a steady state solution:

$$A = \frac{F_o/m}{\sqrt{(\Omega_m^2 - \Omega^2)^2 + \Omega^2\Gamma^2}} \tag{1.46}$$

$$\phi = \arctan(\frac{-\Omega\Gamma}{\Omega_m^2 - \Omega^2}) \tag{1.47}$$

Similarly, the PSD of a thermally driven underdamped harmonic oscillator in angular frequencies is:

$$|X(\omega)|^2 = \frac{F_{th}}{m((\Omega_m^2 - \Omega^2)^2 + \Omega^2\Gamma^2)} \tag{1.48}$$

With the definition $Sxx(\omega) = \int_{-\infty}^{\infty} x(t)e^{i\omega t}dt$, and

$$F_{th} = \frac{\Gamma k_b T}{\pi} \tag{1.49}$$

Note that when compared to the overdamped expression we find $|X(2\pi f)|^2 = 2\pi|X(\omega)|^2$ by taking the limit $\Omega_m \ll \Gamma$. *

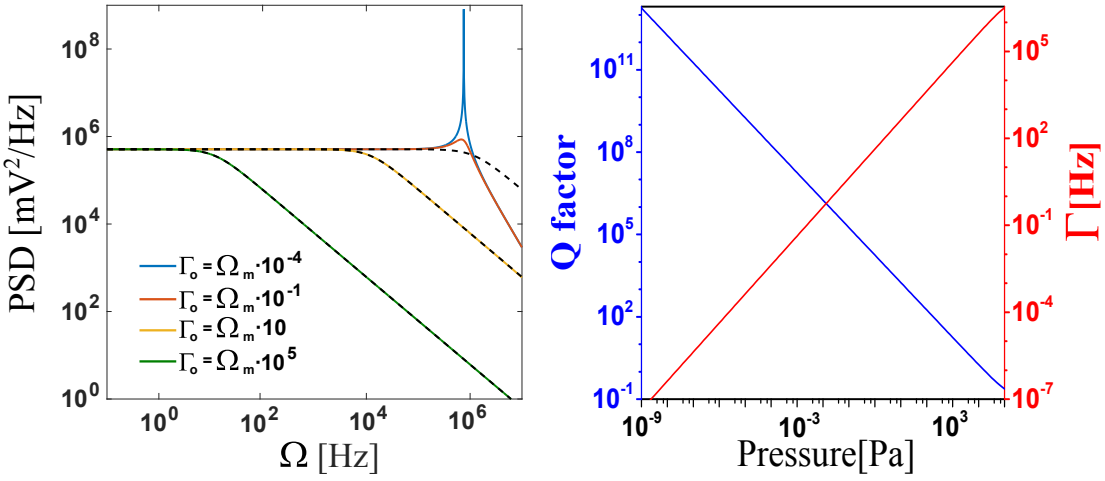

Figure 1.4: (a) PSD of an optically trapped nanoparticle with a mechanical frequency $\Omega_m = 130$ kHz for different levels of damping ($\Gamma = 816{\cdot}10^8, 816{\cdot}10^4, 816{\cdot}10^2$ and 86 Hz). We can differentiate between the overdamped regime (green and yellow curves) and the underdamped regime (red and blue curves). The solid curves have been computed the full expression of the PSD (Eq.1.48) whereas the dashed curves have been computed using the overdamped approximation (Eq.1.45). (b)Estimation of the Q factor and linewidth (Γ_o) for a levitated nanoparticle using kinetic gas theory. The trapped particle is assumed to have a radius of 72nm and oscillate along the x axis at $\Omega_m = 2\pi \cdot 130kHz$. We see that at 10^{-7} Pa the system achieves Q$> 10^{10}$.

.

A useful quantity to describe an underdamped harmonic oscillator is its quality factor, which defines how many oscillations it undergoes before loosing its coherence:

* Although it might seem confusing to use the frequency f in the overdamped regime and angular frequency Ω in the underdamped this follows a practical reason. On the one hand, the optical tweezers community has always worked in the overdamped regime where particle oscillations do not take place and processes studied in the time domain, which when inverted gives frequencies f. On the other hand, the optomechanical community typically uses angular frequencies, so first vacuum optical trapping experiments and theoretical proposals of optical levitation also took the angular frequency notation. Since these are two well differentiated optical trapping communities it makes sense to write to each of them in their own formalism.

$$Q := \frac{\Omega_m}{\Gamma} \tag{1.50}$$

One particular advantage of optically levitated systems is that being free from clamping losses, only the pressure in the system plays a role in γ_m. Therefore arbitrarily high quality factors could be achieved by lowering the pressure as shown in Fig. (1.4b). This is true from the classical point of view, but as we will see later, the photon quantum noise in the trapping beam eventually plays a role as a decoherence mechanism-.

Optical Detection

The next step in the description of optical traps is the method to transduce the particle motion into a measurable signal. There are several approaches in order to monitor the position and dynamics of optically trapped objects, the most common being direct camera detection with centroid fitting algorithms and interferometric detection schemes[88]. In the course of our experiments we have always used interferometric detection schemes as they provide higher sensitivity and acquisition rates ($\sim$ MHz) as compared camera detection ($\sim$ kHz). The goal of this section is to describe how a detection signal is generated and related to the dynamics of the trapped object. We will follow the same paraxial description outlined in [46] adding non-paraxials terms and extending it to the displacements along the optical axis as well.

Lateral Displacements

We start by considering the far field of a tightly focused Gaussian beam diverging with an angle θ:

$$\vec{E}(r,\theta) = \sqrt{P_o}\frac{-ikw_o}{r\sqrt{\pi\epsilon_o c}}e^{ikr-k^2w_o^2\theta^2/4}\vec{x} \tag{1.51}$$

Where the imaginary part in the numerator comes from the so called de Gouy phase[107]

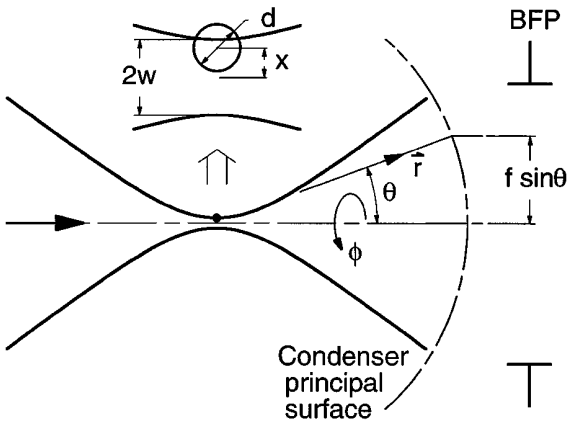

Figure 1.5: Geometry of the BFP detection scheme with the trap centre at the coordinate origin. A dipole-like scatterer in the focus of a Gaussian beam is displaced laterally by x. The far field of the scattered and unscattered fields is observed in the backfocal plane at a radius $f \sin\theta$. Figure adapted from[46] .

.

($\Delta\psi(z) = \arctan(\frac{z}{z_R})$) which adds a phase shift $-\pi/2$ to the trapping beam in the far field. As a result the far fields of a dipole in the focus and the trapping beam result in an interferometric signal with the trapping beam as reference or local oscillator.

For a small lateral displacement x of the dipole (see Fig. 1.5) the scattered far field at observation angle θ and ϕ writes as:

$$E_s(r) = \frac{k^2\alpha'}{4\pi\epsilon_o r} E(x) e^{ik(r - x\sin\theta\cos\phi)} \cos\theta \tag{1.52}$$

Similarly we can rewrite the unscattered field as a function of the beam intensity:

$$E(r) = \frac{-ikw_o I_{tot}^{1/2}}{r\sqrt{\pi\epsilon_s c_s}} e^{-ikr-(kw_o\theta/2)^2} \tag{1.53}$$

Then the resulting intensity of the interference from the scattered and unscattered fields yields:

$$I = \frac{\epsilon_o c}{2}[E_s^2 + E^2 + 2Re(E_s E^*)] \tag{1.54}$$

If we assume that the intensity noise of the trapping beam can be neglected and a weak scattering ($E_s \ll E$), only the last term leads to a change in the intensity pattern:

$$\delta I = \epsilon_o c Re(E_s E^*) \tag{1.55}$$

Combining Eqs. (1.52, 1.53 and 1.55) we obtain the $\delta I(\theta, \phi)$ for lateral displacement x:

$$\delta I = I_{tot} \frac{2k^3\alpha}{r^2 4\pi^2 \epsilon_o} e^{\frac{-x^2}{w_o^2}} \cdot \sin(kx \sin\theta\cos\phi) e^{-(kw_o\theta/2)^2} \cos\theta \tag{1.56}$$

Using a suitable collection lens, we can project this pattern on a split photodiode oriented to detect an intensity difference along the x axis. To obtain the detector response we integrate Eq. (1.56) over θ and over two halves for ϕ: $I_+ = \int_{\phi=0}^{\phi=\pi}$ and $I_- = \int_{\phi=\pi}^{\phi=2\pi}$ (one for each input) and subtract them.

In the case of a low NA collection optics, the paraxial approximation yields:

$$\frac{I_+ - I_-}{I_{tot}} \approx \frac{16}{\sqrt{\pi}} \frac{k\alpha'}{w_o^2} G(\frac{x}{w_o}) \tag{1.57}$$

where $G(u) = e^{-2u^2} \int_0^u e^{-y^2} dy$ and presents a slope $\approx w_o^{-1}$ at $x = 0$.

Displacements along the optical axis

The displacements along the optical axis z can be easily computed by considering the interference pattern between a local oscillator and second wavefront shifted by $\Delta\phi = \pi/2 + kz$. For a small displacement z along the optical axis($z < z_o$) the intensity change out of Eq.(1.56) becomes:

$$\delta I(\theta) = I_{tot}\frac{2k^3\alpha}{4\pi^2\epsilon_o r^2}\sin(kz+\arctan(z/z_r))\cos\theta e^{-(kw_o\theta)^2/4} \approx I_{tot}\frac{2k^4\alpha z}{4\pi^2\epsilon_o r^2}\cos\theta e^{-(kw_o\theta)^2/4} \tag{1.58}$$

Hence, the intensity response is also linear for displacements along the optical axis. In this case however, δI does not depend on ϕ. Thus, in order to reject the intensity term corresponding to the local oscillator, the other port of the splitted detector needs to be illuminated with a second beam with same power as the detection beam.

Discussion

Figure (1.6a) shows the expected detector response to the transverse displacement of a nanoparticle of 72nm radius in a 1550 nm diffraction limited optical trap using a 0.8NA focusing and collection optics. We see that for small displacements from the centre, the response is clearly linear , similarly as we saw for the optical forces. These two features are actually related since the imbalance in the observed photon flux corresponds to the optical force applied to the particle by virtue of the momentum conservation (i.e. the transverse optical forces show the same profile).
Using a paraxial approximation leads to an overestimation of the intensity response compared to the numerical integration of Eq.(1.56) for a high NA. Nevertheless the simplicity of the analytic expression (Eq.1.57) will be useful for further calculations, thus we suggest to use a scaling factor $M \approx 0.675$ matching the slope of the paraxial expression to the numerical result at $x = 0$, which also achieves a good overlapping of both functions for displacements around $\pm$nm.

Figure (1.6b) shows the expected detector response for an axial displacement of a nanoparticle of 73nm radius in a 1550 nm diffraction limited optical trap using a 0.8NA focusing and collection optics. We see that a dipole in the trap centre generates a signal that sits in the middle of the fringe of our interferometric detection, where the intensity response is linear. If the particle is moved by several wavelengths, the interference fringes attenuate due to the lower

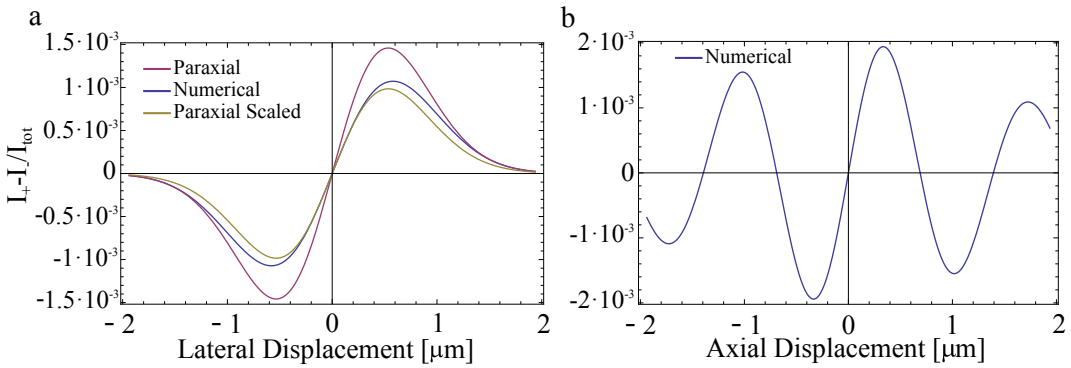

Figure 1.6: (a) Relative detector response ($\frac{I_+ - I_-}{I_{tot}}$) vs. lateral displacement of the particle for a paraxial analytic expression of the described model (purple), numerical calculation for the non-paraxial case (blue) and paraxial scaled by a factor $M \approx 0.675$ to match the slope of the non-paraxial calculation at $x = 0$. (b) Relative detector response vs. particle displacement along the optical axis. The responses are calculated for a 72 nm radius particle in a 1550 nm diffraction limited trap using a 0.8NA focusing and collection optics.

.

field intensity at the position of the dipole.

Remarkably, the BFP detection approach allows, with a single laser beam, to obtain a detection signal for each of the 3 decoupled oscillatory motions taking place in the single beam optical trap. Furthermore this position detection presents two main benefits that make it very convenient for sensitive detection. First, we are using a diffraction limited spot ($w_o \approx \lambda$) whose wavefront becomes spherical already at $z \approx 1$ mm, mode matching the spherical wavefront of the dipole emission from the trapped object and ensuring high fringe visibility. Secondly, since the scattered and unscattered photons follow the same optical path, this scheme results extremely robust in terms of interferometric stability.

Finally, the fact $\delta I(\theta)$ is related to a change in photon momenta shows that optically trapping an objects also performs a continuous position measurement of it. This should not be surprising as a particle in the trap centre continuously scatters photons revealing its position to an external observer.

Optical Trap Callibration

Knowing the dynamics of our trapped particle and how its displacements correlate to a detection signal allows us to calibrate our system. Namely, finding out the trap stiffness κ and a factor S_x [m/V] that linearly converts the voltage output of a photodetector into a linear displacement. Different methods can be used to calibrate the system depending on the trapping regime (overdamped/underdamped) we work. Yet, all calibration techniques rely on trapping a known particle and acquiring a long measurement of the particle thermally driven motion. Afterwards, from the measured dynamics, the properties of the trapping potential are inferred. In this section we will briefly describe the most common calibration methods for optical traps. Readers looking for a more detailed treatment are referenced to[57].

Maxwell-Boltzmann distribution Method

The equipartition method is used in the overdamped regime and relies on fitting the measured position distribution of the trapped particle $\rho(x)$ to the expected Maxwell-Boltzmann distribution for a harmonic potential:

$$\rho(x) = \rho_o e^{-\frac{\kappa_x (x - x_{eq})^2}{2\sigma_x^2}} \tag{1.59}$$

First though, we need to find S_x. From the acquired time trace, we compute the mean square displacement (MSD) of the signal for short times ($\tau \ll \gamma/\kappa_x$):

$$MSD(\tau) = \overline{[V(t+\tau) - V(t)]^2} = 2\frac{k_b T}{\kappa}\left(1 - e^{-\frac{\tau \kappa_x}{\gamma_V}}\right) \approx 2k_b T \gamma_V \tau \tag{1.60}$$

where γ_V is the damping factor scaled by S_x^2 (this formula relies on the particle diffusive behaviour at short timescales). From γ_V and knowing γ_m from the object and environment properties, we compute $S_x = \sqrt{\gamma_m/\gamma_V}$. Using S_x we transform the voltage time trace into a position time trace and compute $\rho(x)$ from where we extract the variance in the position

σ_x. Finally, using the equipartition theorem leads to

$$\langle x\frac{\partial H}{\partial x}\rangle = \frac{1}{2}\kappa_x\sigma_x^2 = \frac{1}{2}k_bT \tag{1.61}$$

giving the trap stiffness $\kappa_x = \frac{k_bT}{\sigma_x^2}$.

Autocorrelation Method

This method is based on computing the discrete autocorrelation function (ACF) of the experimental time trace. For a time trace with the positions $x_j = x(t_j)$ with $j = 1...N$ at sampling times $t_j = j\Delta t$ we compute the ACF as:

$$C_{x,exp}(\tau) = \frac{1}{N-k}\sum_{j=1}^{N-k} x_{j+k}x_j \tag{1.62}$$

which then can be fitted to the analytical expression:

$$C_x(\tau) = \frac{1}{T}\int_0^T x(t)x(t-\tau)dt = \frac{k_bT}{\kappa}e^{-\frac{|\tau|}{\gamma_m/\kappa_x}} \tag{1.63}$$

Thus fitting the the time constant of the exponential decay in the experimental data we obtain γ_m/κ_x. It is a rather simple method since only requires a linear fit. This method is useful if one needs to deconvolve complex time dynamics going on the trap.

Power Spectral Method

This method can be used in both the overdamped regime and the underdamped regime (this later requires knowing also the mass of the trapped object). It consists on computing and then fitting the experimental PSD of the detection signal X_V, which will be in units of V^2/Hz

For the overdamped regime, we fit $X_V(f)$ to Eq.(1.45) with f_c as fitting parameter (Fig.1.7d). Then the stiffness of the system is given by $\kappa = 2\pi f_c\gamma_m$. Computing the MSD

gives again the calibration factor that transforms $|X_V(f)|$ into the physical units m^2/Hz so the mean energy in the position degree of freedom of the oscillator satisfies the equipartition theorem (Eq.1.59).
This is the most used by the optical trapping community as it also allows to detect and filter different sources of noise that might distort the signal and there are several published routines[50] that simplify the fitting. Experimentally it is important to make sure that the acquisition frequency is well above the Nyquist frequency to avoid artefacts on the experimental PSD.

In the underdamped regime we fit the $X_V(\omega)$ to Eq.(1.48) with F_{th} and Γ as fitting parameters. We obtain $\kappa_x = m\Omega^2$ directly from the maximum of the PSD and the known mass. The conversion factor is obtained integrating the PSD $X_V(\omega)$ to obtain $\langle V^2 \rangle$ and then scaling it to m^2 so the mean energy satisfies the equipartition theorem (Eq.1.59):

$$\langle x^2 \rangle = S_x^2 \langle V^2 \rangle = S_x^2 \cdot 2 \int_0^\infty X_V(\omega)^2 d\omega = \frac{k_b T}{m\Omega_m^2} \tag{1.64}$$

Figure (1.7a) shows an experimental time trace for a $1\mu m$ particle in an optical trap in the overdamped regime. Then we apply each of the calibration methods described above (1.7 b,c,d) to obtain $\kappa_x \approx 137 pN/\mu$m.

Drag Force Method

This method relies on applying a constant force to the optically trapped particle by displacing the surrounding medium. This can be achieved for example by creating a laminar flow in a microfluidic chamber, resulting in a constant force acting on the particle or moving the sample stage. Measuring the displacement from the center of the trap Δx for a constant force gives directly the stiffness $\kappa_x = F/\Delta x$.

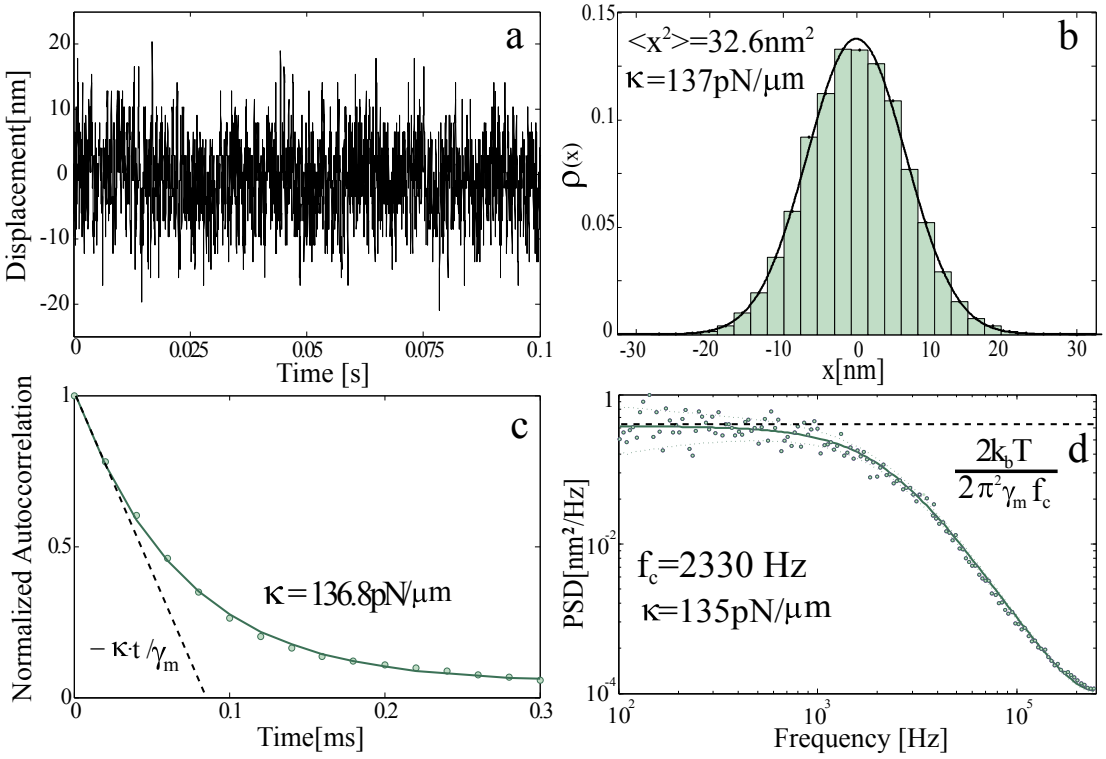

Figure 1.7: (a) Experimental time trace along x for a 1 μm silica particle optically trapped in water. We illustrate three different methods to calibrate the trap stiffness: (b) shows the Equipartition methods with the normalised histogram of position (green bins) and the fitted $\rho(x)$.(c) shows the experimental autocorrelation function (green dots) and the fit to an exponential decay (solid green line). At short correlation times, the response can be linearised (black dashed line) with a slope $-\kappa_x/\gamma_m$. (d) PSD method with the experimental PSD (green dots) and the Lorentzian fit (solid green line). At low frequency the PSD saturates to $2k_bT/(2\pi^2\gamma_m f_c)$.

Trap calibration beyond the linear regime

In the experiments developed during this thesis we always try to work in the linear regime. However, at large displacements from the beam focus ($\Delta x > w_o$) the restoring force looses its linearity. In these cases, the above methods (except the drag force) are not suitable to calibrate optical traps. To calibrate an optical trap beyond the linear regime it is necessary to follow a two step calibration process. First we start with a high stiffness reference trap that is calibrated using one of the described methods. Then we scan the trap we want to calibrate in the non-linear regime across the high stiffness trap by steering a mirror conjugated with the BFP of

the trapping lens. Note that the second trap needs to be attenuated so it has a relatively low stiffness -this will not be a problem, since the potential scales with the optical power used in the trap (Eq.1.29). Now one can reconstruct the optical potential of the weak trap using the particle in the stronger trap as a force probe.

Optical traps

So far we have presented the general theory describing the underlying physics of optical trapping: from optical forces to optical detection. With these physical principles there exist several ways one can implement a stable optical trap, each of them with specific characteristics that fit different experimental needs and limitations. For completeness we will show a quick overview on these configurations. In the following chapters we will give a more detailed view of the traps used in each experiment .

Single Beam Optical Traps

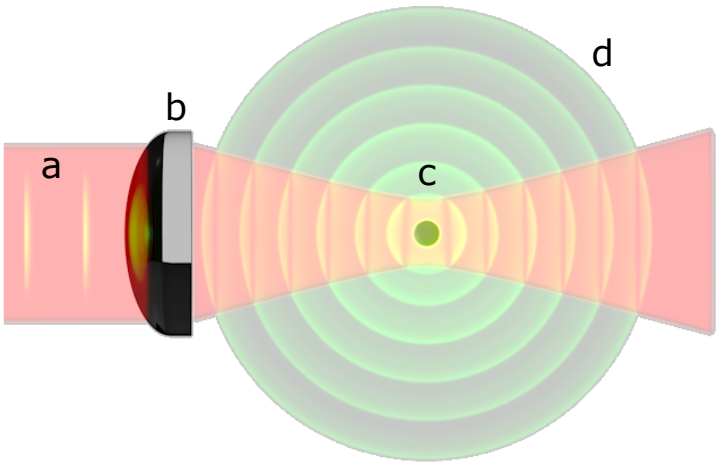

Figure 1.8: Basic elements required for a single beam optical trap: A collimated laser beam (red beam**a**) is focused to a diffraction limited spot using a single element focusing optics (**b**). The particle is trapped at the focus of the beam (**c**) and the forward scattered (green waves **d**) and unscatered fields propagate freely.

.

A single beam optical trap relies on a laser beam tightly focused to a diffraction limited spot in order to achieve $F_{grad}(\rho) > F_{scat}(\rho)$. This is the most widely used type of optical trap and requires a single focusing element. Due to the high NA requirements for the focusing optics (NA>0.7), optical traps are created close to the lens surfaces (100 μm to 2 mm away), thus limiting the geometry of the experiment. The basic elements of this configuration are shown in Fig.(1.8)
In this configuration the transverse stiffness (κ_x, κ_y) is typically 2-3 times larger than along the optical axis (κ_z). The main advantage of this geometry is the direct access to the forward scattered field of the particle, allowing for highly sensitive detection schemes. This geometry has been used in our Mobile Optical traps in vacuum[81] as well as in our thermodynamics experiments in liquid environment[83] and is also suitable for trapping with more exotic beams carrying orbital angular momentum such as Laguerre-Gaussian beams[3].

Counterpropagating Optical traps

Counter-propagating optical traps consist on focusing two identical and counter-propagating optical beams. In this configuration each beam has an opposed $\vec{k}$ vector resulting in the compensation of the scattering forces in the centre. The particle is confined along the transverse direction due to gradient forces, whereas along the optical axis both gradient and the opposing scattering force contribute to stability.

This approach has also been widely followed by several optical tweezers groups in the field of biophysics[29,2] and more recently by some groups working in optical levitation of microspheres[42,86,68] The main advantage of this approach is that due to the cancellation of scattering forces the NA requirements of the focusing optics become less stringent. This allows to work with lower optical intensities as well as trap the objects farther from the focusing optics. These traps are also more robust against spherical aberrations but they requires some extra optical elements in order to separate and control the beams polarization in the centre of the optical trap.

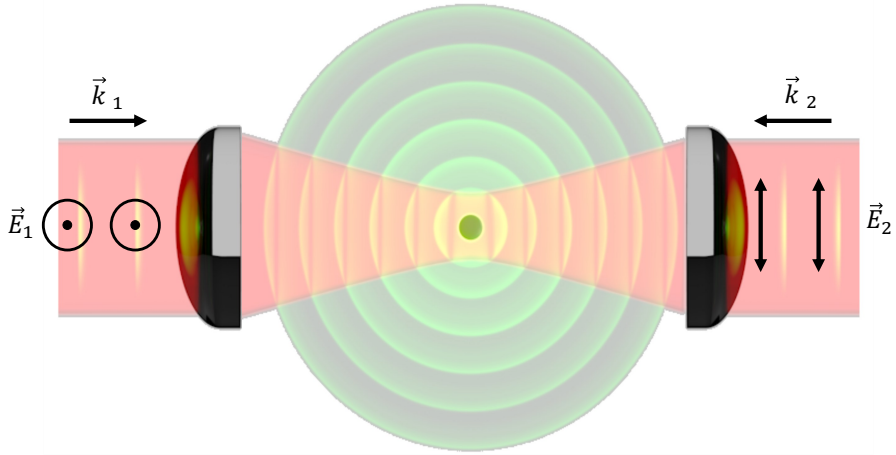

Figure 1.9: Basic elements required for a counter-propagating optical trap: Two counter-propagating laser beams (k_1 and k_2) with orthogonal polarizations ($\vec{E}_1$ and $\vec{E}_2$) are focused into the same spot to create a stable potential.

.

Cavity Standing wave

This approach makes use of the spatial field gradient created by the intensity profile of a standing wave in an optical cavity as suggested by Chang et al.[26] and Romero et al.[101]. It does not require any focusing optics and little optical powers due to the field enhancement factor provided by the cavity. Due to the low NA of the optical mode in the cavities, transverse forces are well described using the paraxial approximation discussed above. Regarding the axial forces, we need to consider the gradient force on a standing wave with a profile $E(z) = E_o \cos(k \cdot z)$. This gives,

$$F_z = \alpha' \cdot \frac{2k^2 I_o}{c\epsilon_o} z \tag{1.65}$$

Consequently we can achieve very deep potentials along the optical axis due to the compensation of the scattering forces and the force scaling with $\propto \lambda^{-2}$ instead of z_o^{-2} as in previous cases. Technically this configuration requires more equipment in order to lock the laser to the cavity during the experiment, which becomes increasingly challenging as the cavity Finesse increases. This configuration was first implement to trap nanoparticles by Kiesel et al.[62] in the

context of vacuum optical traps and later also by our group[82].

Plasmonic Optical traps

This approach uses the rapidly decaying evanescent fields from plasmonic nanostructures to create very large field gradients over distances $L \ll \lambda$. This family of traps were first implemented by Volpe et al.[124] in our group and have established themselves as subfield in the plasmonics community.

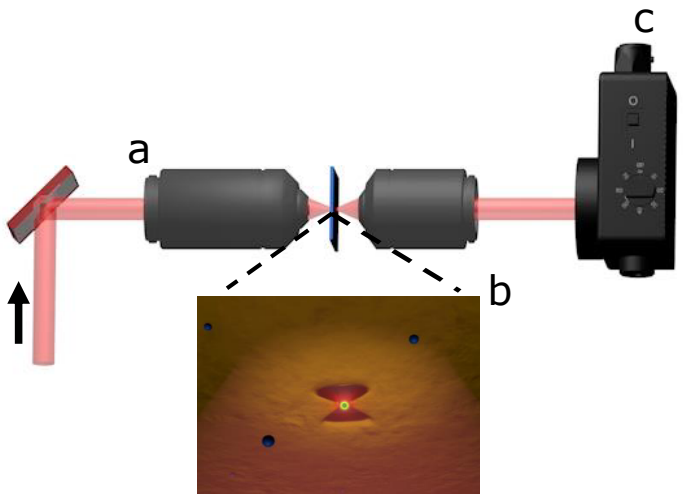

Figure 1.10: Basic elements required for a plasmonic trap: An optical beam (**a**) is used to excite a metallic structure in a substrate (**b**) surrounded by a liquid dispersion containing the sample to be trapped. The light transmitted thruogu the nanostructure is collected and sent to a photodiode (**c**) to monitor the dynamics of the trapped sample.

A general configuration consists on patterning a dielectric surface with metallic structures using nanofabrication techniques. Then, the patterned surfaces are covered by a liquid dispersion containing the sample and sealed for the experiments. The traps are created by exciting plasmons in the patterned structure in a different ways[80,59]. The main benefits of this ap-

proach are the small size of the optical traps and the large field gradients, which allows them to be used in integrated devices and trap smaller objects with lower optical powers. At the same time, due to the poor control of the material geometry and properties in the subwavelength scale, it becomes very challenging to obtain repeatable structures. Hence, quantitative repeatability of results among experimental groups is still challenging. An added difficulty is the non-existence of a standard trapping structure and detection schemes.

It does not matter how slowly you go as long as you do not stop.

Confucius

2

Stochastic Thermodynamics with optical tweezers

Stochastic Thermodynamics establishes a link between the stochastic dynamics of a system and Thermodynamics. This framework is particularly well suited to describe the thermodynamic functionals of trapped microparticles from the experimental observables that appear in the Langevin equation of motion our system. In this chapter, we will show how to compute the thermodynamic functionals such as heat and work in an overdamped optical trap using the stochastic thermodynamics framework. Then, we will use our trap as platform to study non-equilibrium processes and we present a new technique that extends the capabilities of optical traps to study non-isothermal thermodynamics in the mesoscale.

Stochastic Thermodynamics

Thermodynamics deals with the study of heat, temperature, energy and work of systems. Its birth was motivated by the work of the French physicist Sadi Carnot who aimed to understand and improve the efficiency of heat engines[22]. One of its building blocks are the laws of thermodynamics[117]:

- Zeroth Law: If two systems are both in thermal equilibrium with a third one, both have the same temperature.
- First law: In a closed system energy can be transferred in the form of work (W) and heat (Q). The total energy is conserved, but the internal energy of the closed system changes as $\Delta U = Q + W$.
- Second Law: Any non-equilibrium system will evolve towards a state which maximises its entropy $\Delta S \leq 0$.
- Third Law: The entropy of a system approaches a constant value as the temperature approaches absolute zero.

These laws allow us to predict how a system containing containing $N \approx 10^{23}$ particles evolve as a parameter is changed, greatly reducing the degrees of freedom needed to describe it. The evolution can be nicely expressed in the form of an equation of state such as the well known Combined Gas Law[117]:

$$P \cdot V = N \cdot k_b T \tag{2.1}$$

where P and V correspond to the pressure and volume of the system.

This reduction of degrees of freedom is justified by the so called Central Limit theorem[70], which states that the relative magnitude of fluctuations in the system will be proportional to $1/\sqrt{N}$ when coupled to a thermal bath. Hence systems containing many particles can be described in terms of their ensemble average. This allowed physicists and engineers to gain

understanding on how macroscopic systems such as heat engines exchange and transform energy.

In the last decades, miniaturization and nanotechnology have enshrined the size of the physical systems down to the μm and nm scales, creating and discovering a plethora of nanomachines[77], specially in the field of biophysics[122] and molecular motors[51]. At these scale the magnitude of thermal fluctuations is comparable with the energy stored in the system thus the classical description where thermal fluctuations are averaged out, fails. In fact even classical laws of thermodynamics seem to fail during individual events on fluctuating systems[127]. As a result, we need a new framework to describe explicitly how the few degrees of freedom of a microscopic system interact with a macroscopic thermal bath consisting of a large number of inaccessible degrees of freedom.

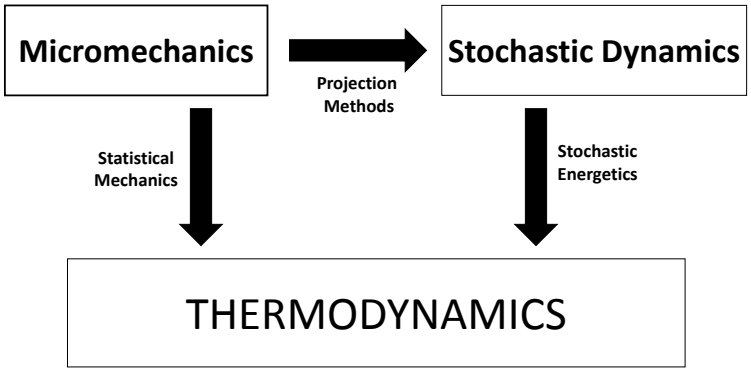

Figure 2.1: Conceptual map of the stochastic thermodynamics field. Systems can be described from different perspectives as their thermodynamic behaviour, stochastic dynamics or micromechanics. Different frameworks such as Statistical mechanics, Projection methods and stochastic energetics allow to switch between the different descriptions.

During the 90's this theoretical framework was developed with the theoretical contributions of Gallavotti[38], Jarzynski[55], Sekimoto[111], Evans[108] and Crooks[30] under the name of stochastic dynamics. Using this approach the microscopic system is described with a deterministic equation of motion where the interactions from the thermal bath are added in the form of fluctuating terms. The noise terms will be characterized by a statistical distribution (for example, Gaussian white noise for thermal fluctuations, Poisson shot noise for photon

number fluctuations, etc...). Stochastic dynamics describes well the dynamics of our microscopic sytems, but it does not account on how energy is exchanged with the thermal environment along single realizations or trajectories of the microscopic system. This missing link was established in the early 2000's by the work of Sekimoto under the name of Stochastic energetics[112], allowing to compute energy transfers (heat and work) along individual trajectories of a stochastic system. During the same period several experimental groups contributed to demonstrate the validity of the non-equilibrium fluctuation theorems in colloidal[127] and biological[29] systems derived by Jarzynski and Crooks.
In 2005 Udo Seifert suggested that entropy could also be attributed to fluctuating trajectories and gave the name of Stochastic Thermodynamics to this framework[109]. This established the necessary tools that have recently allowed to experimentally validate some fundamental aspects in the field such as the implementation of a Maxwell Demon by Toyabe et al.[120] and an experimental proof of the Landauer principle by Berut et al.[14] with its generalization in the symmetry breaking experiments of Roldan et al.[100]

Heat and Work in the Mesoscale

Here we derive the concepts of heat and work in the mesoscale in order to understand and describe the energy exchange in our microsystem. In this chapter we will restrict ourselves to the overdamped regime. For an in-depth derivation including the inertial regime we refer to Sekimoto's work[112].
Our starting point is the overdamped Langevin equation of a spherical particle in an optical potential U::

$$0 = \frac{\partial U(x,a)}{\partial x} - \gamma_m \frac{dx}{dt} + \xi(t) = -\kappa(a)x - \gamma_m \frac{dx}{dt} + \xi(t) \tag{2.2}$$

It contains the minimal triad of a system represented by x, a thermal environment (the bath characterized by a temperature T and friction coefficient γ_m) and an external system (a degree of freedom that controls the system through the parameter a). Energy is exchanged between these three in the form of heat (Q) and work (W) according to the laws of thermody-

namics. We start by considering the energy exchange of a particle with its environment upon a change dx in the particle trajectory in a constant potential:

$$dU(x) \equiv \frac{\partial U(x)}{\partial x} \circ dx = -(-\gamma \frac{dx}{dt} + \xi(t)) \circ dx \tag{2.3}$$

where $\circ$ is a Stratonovich-type product. Combining this result with the first law of thermodynamics allows us to define heat as:

$$dQ \equiv -(-\gamma \frac{dx}{dt} + \xi(t)) \circ dx \tag{2.4}$$

In other words, heat is the energy exchanged between the system and the bath eliminated degrees of freedom.

Next we consider a potential that varies as a function of a controllable external degree of freedom $a(t)$. The energy exchange is:

$$dU(x, a) = \frac{\partial U}{\partial x} \circ dx + \frac{\partial U}{\partial a} \circ da \tag{2.5}$$

that together with Eqn.(2.3) and the 1^{st} law yields:

$$dW \equiv \frac{\partial U(x, a)}{\partial a} \circ da \tag{2.6}$$

Hence work is the energy change in the system related to changing a controllable degree of freedom. These definitions of differential heat and work allow us to compute the cumulative heat and work along a trajectory as:

$$Q = \int_{x_o}^{x_t} \frac{\partial U(x, a)}{\partial x} \circ dx \tag{2.7}$$

$$W = \int_{a_o}^{a_t} \frac{\partial U(x, a)}{\partial a} \circ da \tag{2.8}$$

Fluctuations

When the work applied on a system out of equilibrium is on the order of the thermal fluctuations k_bT, it is possible for certain trajectories to violate the second law of thermodynamics. The probability of such an event was derived by Evans and Searles[35]:

$$\frac{\rho(\Delta s)}{\rho(-\Delta s)} = e^{\frac{\Delta s}{k_b T}} \tag{2.9}$$

Where $\rho(\Delta s)$ is the probability to observe and entropy change Δs. In other words, the probability to observe an entropy decrease decays exponentially. Note that, since entropy is an extensive quantity, the 2^{nd} law is recovered for large systems. This expression is valid for systems arbitrarily far from equilibrium and was first experimentally tested by Wang et al. by using optically trapped particles[127].

Equation (2.9) is one of the non-equilibrium fluctuation theorems (FT) that describe the statistical properties of thermodynamics functionals in the presence of thermal fluctuations. Two other relations important for us are the Crooks Fluctuation Theorem and Jarzynski's equality:

Crooks' Fluctuation Theorem

Consider a system in a state A that evolves to state B by changing a control parameter a in time. This process (forward) will be characterized by the work probability distribution $\rho_F(W)$. Similarly we can bring back the system from state B to A by reversing in time the control parameter a and obtain a (backwards) work distribution $\rho_B(W)$. Then the Crooks fluctuation theorem (CFT) establishes the following relation for these work distributions[30]:

$$\frac{\rho_F(W)}{\rho_B(-W)} = e^{-\frac{(W-\Delta F)}{k_b T}} \tag{2.10}$$

Where ΔF is the free energy difference between the states A and B.

Jarzynski's Equality

The Jarzynski's equality establishes that the average work done along a trajectory from states A$\rightarrow$ B and the free energy difference between them fulfils:

$$\langle e^{-\frac{W_{A\rightarrow B}}{k_b T}} \rangle = e^{-\frac{\Delta F_{A\rightarrow B}}{k_b T}} \tag{2.11}$$

Despite their validity out of equilibrium these expressions provide equilibrium information of the system. Hence these theorems become a powerful tools to that extract equilibrium information of systems performing out of equilibrium. These will allow to cross-check our experimental non-equilibrium and equilibrium measurements.

Description of the experiment

As we can see from in the literature[120,14,100,83], optical trapping experiments have been one of the main driving forces in the field of stochastic thermodynamics. They offer a robust and versatile platform for micromanipulation of a system consisting of few degrees of freedom and enough accuracy to resolve energy fluctuations on the order of $k_b T$. However, the study of non-isothermal processes in optical traps has remained fairly limited due to the challenges of controlling the temperature in the microscale. These arise from the difficulty to isolate microscopic systems and to the presence of convection effects in fluids, thus temperature control in optical traps could only achieve a range of few tenths of Kelvin around room temperature[74]. To overcome this short range of accessible temperatures we suggest to use an additional random force as a heat bath for a colloidal particle. Since the magnitude of the fluctuations is related to the temperature, we will be able to control the effective temperature seen by our particle by controlling the amplitude of the random forces. To verify this hypothesis we will perform an extensive study of two different thermodynamic processes in order to check the consistency of our thermal bath in and out of equilibrium. These will be a case where where W depends on the temperature and a case where it does not.

We start by adding an extra noise term $\xi_E(t)$ to Eq.(2.2)

$$\gamma\dot{x}(t) + \kappa_x(x(t) - x_0) = \xi(t) + \xi_E(t) \tag{2.12}$$

Where $\xi(t)$ and $\xi_E(t)$ are uncorrelated and $\xi_E(t)$ has also a Gaussian white noise (thermal) spectra:

$$\langle \xi(t)\xi_E(t) \rangle = 0 \tag{2.13}$$
$$\langle \xi_E(t)\xi_E(t') \rangle = \sigma^2\delta(t - t') \tag{2.14}$$
$$\langle \xi_E(t) \rangle = 0 \tag{2.15}$$

In the absence of external forces $\xi_E(t)$ and κ_x and x_0 fixed at a constant value, the particle position fluctuation are Gaussian-distributed. The amplitude of these fluctuations depends on the temperature of the surroundings T as predicted by equipartition theorem $\kappa_x\langle(x - x_0)^2\rangle = k_bT$. If we now include the external random force $\xi_E(t)$, the equipartition theorem allows us to define a centre of mass temperature of the particle T_{kin} from the amplitude of its motion,

$$T_{\text{kin}} = \frac{\kappa_x\langle(x - x_0)^2\rangle}{k_b} = T + \frac{\sigma^2}{2k_b\gamma_m} \tag{2.16}$$

We also want to find a way to measure this T_{kin} out of equilibrium. In this case, the CFT shows that work fluctuations are not symmetric upon time-reversal of the protocol. Thus we define the following asymmetry function [40],

$$\Sigma(W) = \frac{W - \Delta F}{k_bT}. \tag{2.17}$$

Which can be used to define an effective non-equilibrium temperature that we name Crooks Temperature (T_C) calculated from the slope of $\Sigma(W)$ as a function of W.

$$T_c = \frac{W - \Delta F}{k_b\Sigma(W)} \tag{2.18}$$

The value of the effective Crooks temperature depends strongly on the properties of the external noise. In general T_c and its equilibrium counterpart T_{kin} do not coincide. However, if the external force is an external Gaussian white noise we expect $T_c = T_{\text{kin}}$[78] . From the experimental point of view we cannot generate a white noise due to the limited bandwidth of our systems. Hence the optimal bandwidth for $\xi_E(t)$ that guarantees it's behaviour as a thermal bath will also be studied.

Experimental Setup

Our optical trapping setup consists of an electrophoretic chamber to exert random forces on the particles trapped in an optical tweezer measuring the position fluctuations. The main idea behind using elecrophoretic forces is that such a mechanism is decoupled from the optical trapping mechanism.

Electrophoretic chamber

Dielectric particles acquire surface charge when they are suspended in a polar liquid like water[34]. This means that we can exert them forces by applying electric fields. The electrophoretic flow cell provides a stable trapping environment as well as the capability to exert high electric fields on its centre. The main requirement of the electrophoretic chamber is to produce high and uniform electric fields in the trapping region. Repeatability of the channel in different flow cells is not as important since forces can calibrated and tuned accordingly. This allows us to use a simple and reliable fabrication technique[84].

Figure (2.2) shows a schematic design of the flow cell consisting of two wide reservoirs with an electrode. The reservoirs are connected by a short (< 5mm) and narrow (< 2mm) channel. This design fulfils two requirements: First the central channel provides higher resistivity than the two reservoirs, achieving high E fields in the central trapping regions. Second, since the radius of our particle ($\sim \mu$m) is much smaller than the channel features (mm), it experiences a uniform E field along small displacements (≈ 250 nm).

The flow cell is cut in a piece of parafilm (using a sharp razor or a focused CO_2 laser). A

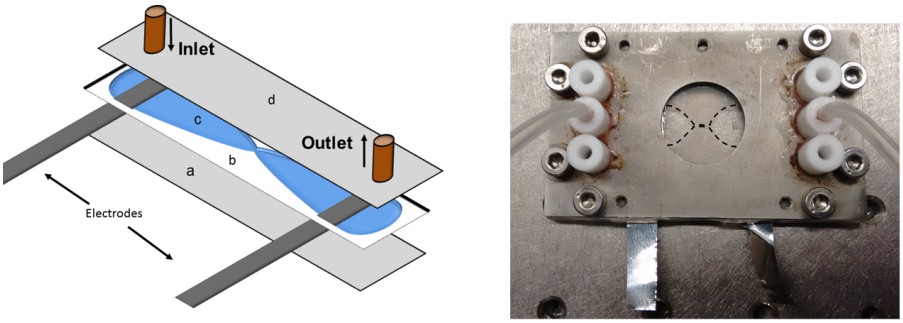

Figure 2.2: Diagram of the flow cell. The glass slides (a,d) sandwich a piece of parafilm (b) where the reservoirs connected with a narrow channel have been cut (c). The electrodes are connected to the high voltage amplifier in contact with the solution containing the suspended microparticles. On the right we see an actual flow cell mounted in a metallic holder used in the trapping experiments. The dashed lines mark the boundary of the channel.

100μm thick glass slide with two holes serves as inlet and outlet of particles (holes can be made by means of a focused CO_2 laser, HF acid or sandblasting). At the edges of a second glass slide we glue two electrodes made by cutting a 0.5cm x 5cm piece of a 50μm thick stainless steel foil. Then, the chamber is sealed by sandwiching the parafilm mask between the two glass slides while heating them on a hot plate. Finally, the tubing is attached to the top coverslip holes using small plastic connectors glued with epoxy. For safer manipulation and clamping of the flow cell we use the aluminium holder shown in Fig.(2.2).

The electrodes of the electrophoretic flow cell are connected to a high voltage amplifier with a maximum output of 2000V* driven by an arbitrary waveform generator providing the Gaussian white noise signal.

*TREK 623B 10kHz bandwidth

Random forces generation

To generate a Gaussian white noise we use the Box-Muller algorithm[3]. We generate a sequence of 10^6 random numbers $\{x_i\}$ with a normalised Gaussian distribution ($\langle x_i \rangle = 0$ and $\langle x_i x_j \rangle = \delta_{ij}$) and we load this sequence into the memory of the arbitrary waveform generator connected to the amplifier. Since the bandwidth of the amplifier is limited to 10 kHz, we set the clock rate for the random voltage to 20ksamples/sec. This repeats the sequence every 50s, which is enough to avoid artefacts and correlations. Note that with this configurations one can also exert forces with an arbitrary distribution such as sinusoidal, ramps, etc. and these are totally decoupled from the trapping mechanism.

Optical Tweezer

The electrophoretic flow cell is mounted on the self-built inverted microscope setup shown in Fig. (2.3). To create the optical tweezer we use a fibre coupled high power laser 5W CW [†]. After the fibre the beam is tightly collimated using a 40X achromatic objective (Edmund) and sent through an acousto-optic-deflector (AOD) [‡]. Using a $\lambda/4$ waveplate prior the AOD we maximise the diffraction efficiency. After the AOD a telescope expands the beam and conjugates the crystal diffraction plane with the backfocal plane of the High NA microscope objective (O1) [§]. This creates an optical trap in the channel of our electrophoretic flow cell that can be displaced along one axis by changing the driving frequency of the AOD. Before the objective we also place a $\lambda/4$ and $\lambda/2$ waveplates to set a linear polarization for our trap and a polarizing beam splitter (PBS) that splits the beam to a photodiode monitoring the power in the trap.

The position detection system consists of a green fibre laser collimated using a 10X achromatic objective (Edmund optics) mounted on a z axis translation mount to adjust the divergence of the beam at the entrance of the trapping objective. The forward scattered light of the

[†]ManLight, λ =1064nm
[‡]Isomet LS55-NIR
[§]Nikon CFI PL FL 100X, NA 1.3

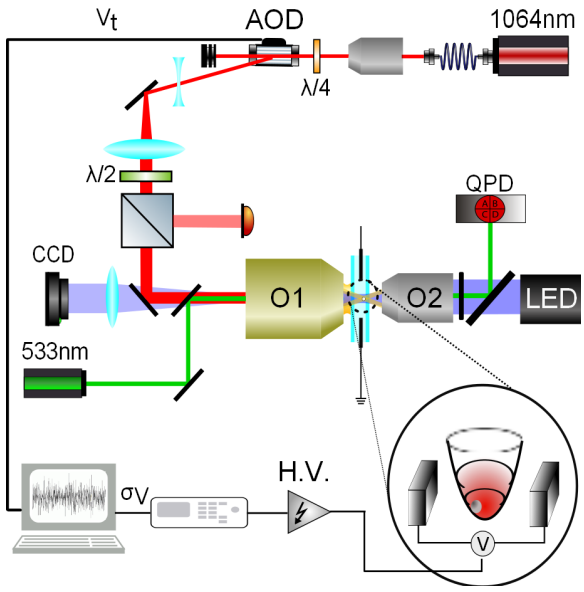

Figure 2.3: Schematics of the Optical tweezers setup combined with an electrophoretic flow cell. A 1064 nm laser beam is diffracted using an AOD and focused with a 100X objective (O1) to form an optical tweezer. A second laser beam with at 532 nm is focused with the same objective (O1) and the forward scattered light collected with a 10X objective and sent to a QPD for position detection. To exert random forces the electrophoretic chamber electrodes are connected to a high voltage amplifier (HV) that amplifies the signal of an arbitrary waveform generator.

detection beam is collected by a 10x objective (O2) and projected to a quadrant photodiode ¶. To block the trapping beam and ambient lights we put a $\lambda = 532nm$ laser line filter in front of the photodetector. The x, y and z voltages from the photodiode are sent to a Labview FPGA card (NI PXI-7842R, maximum acquisition frequency 200 kHz) for analog-to-digital conversion.

The sample is illuminated by a white led lamp using the same 10x collection objective from the detection. The image is collected using the same trapping objective and sent to a CCD camera connected to an external monitor. Our sample consists of polystyrene microspheres of radius 500 ± 25 nm (PPs-1.0, G.KiskerProducts for Biotechnology).

¶QPD, NewFocus 2911, 200 kHz bandwidth

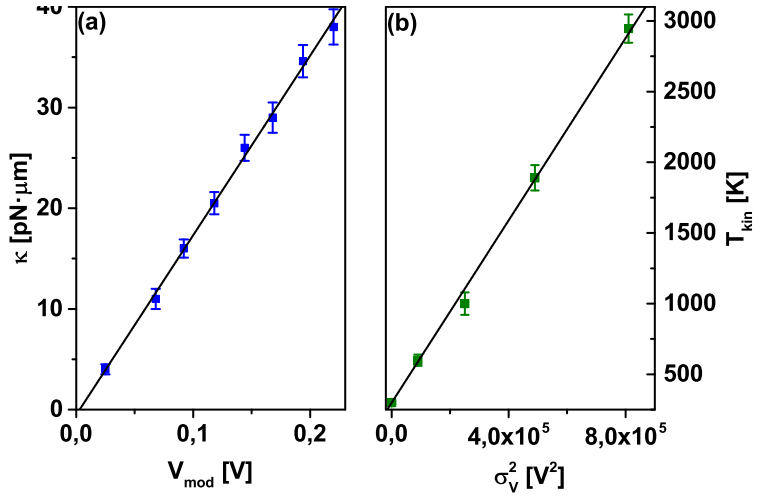

Figure 2.4: Calibration of the thermodynamic tweezers setup: (a) shows the stiffness of the optical trap as a function of the modulation voltage V_t applied at the AOD, which agrees to the linear fit $\kappa = (-0.58 + 178.45V_t)$pN/$\mu$m.(b) shows the temperature of the thermal bath experienced by the particle T_{kin} as a function of the variance of the random voltage applied on the electrophoretic chamber σ_V^2. The black solid line corresponds to the linear fit T_{kin} =$300K + \frac{3274K}{V^2}\sigma_V^2$.

Calibration of the Setup

The calibration of the setup follows two steps. First a standard calibration of the optical tweezer and then a calibration for the temperatures of the virtual thermal bath. To the adjust alignment between the QPD x axis and the forces generated in the electrophoretic chamber we apply a sinusoidal signal at 18 Hz to a trapped particle while monitoring the PSD of the QPD signal for x and y (S_{xx} and S_{yy}). Then we adjust the detector or the electrophoretic chamber angle until the 18 Hz peak is only visible in the S_{xx}.

The calibration of the optical tweezer is made using the PSD method. Since the intensity of the optical trap is controlled by the modulation depth (V_{mod}) driving the AOD we repeat this calibration at different values of V_{mod}. Fig 2.4 (a) shows the κ calibration curve as a function of V_{mod} showing good agreement with a linear fit.

The second calibration step allows us to obtain T_{kin} of the microparticle. Since the po-

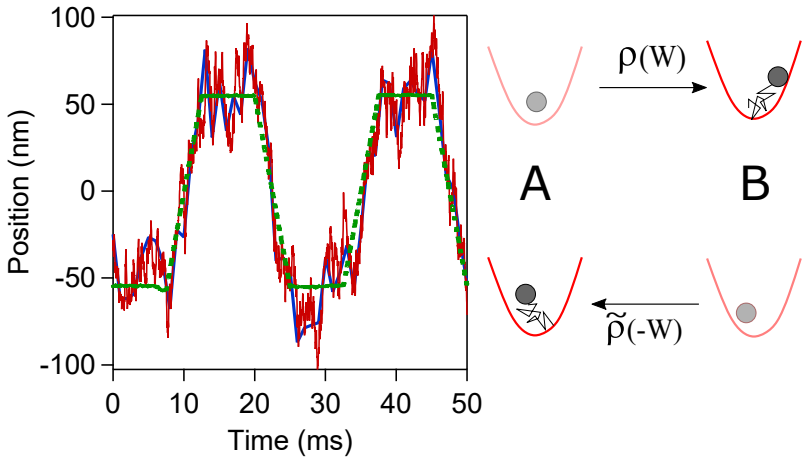

Figure 2.5: Position of the trap (green dashed curve) as a function of time and time traces of the position of the particle sampled at 1 kHz (blue curve) and 10 kHz (red curve) in the dragging experiment. The forward (A→ B) and backward (B→A) processes are illustrated on the right.

sitions histogram of a particle in a harmonic potential follows a normal distribution, we can extract T_{kin} from the variance of the position distribution of the particle σ_x^2 as:

$$T_{kin}(\sigma_V^2) = \frac{\kappa\,(V_{mod})\,\sigma_x^2\,(\sigma_V^2)}{2k_b} \tag{2.19}$$

Where σ_V^2 is the variance of the voltage at the output of the waveform generator. Figure (2.4b) shows a calibration curve for $T_{kin}(\sigma_V^2)$ reaching up to 3000K which is a full order of magnitude above room temperature. As expected for a thermal force, T_{kin} grows linearly with the variance of the force fluctuations σ^2 [78]. The slope of the calibration curve contains all the geometric factors of the system that determine the intensity of electric field in the electrophoretic chamber as well as the particle response to the electrical forces. In the case of Fig.(2.4) it fits to $T_{kin} = 300K + \frac{3274K}{V^2}\sigma_V^2$.

Experimental Results: Dragged Trap

Our first case of study consists of a particle that is driven out of equilibrium by dragging the optical trap ($\kappa = 18.0 \pm 0.2\,\mathrm{pN}/\mu\mathrm{m}$) at constant speed $v = 22\,\mathrm{nm/ms}$. The protocol

is shown in Fig.(2.5) together with a time series of the position of the particle sampled at different acquisition frequencies. First the trap is held fixed with its centre at $x_0 = -55$ nm during $\tau_1 = 7.5$ ms. Then the trap centre is displaced in the $x-$axis at a constant velocity from $x_0 = -55$ nm to $x_0 = 55$ nm in a time interval of $\tau_2 = 5$ ms. The bead is then allowed to relax to equilibrium by keeping the trap centre fixed at $x_0 = 55$ nm for $\tau_1 = 7.5$ ms before the trap is moved back from $x_0 = 55$ nm to $x_0 = -55$ nm in $\tau_2 = 5$ ms. The duration of each cycle is $\tau = 25$ ms and every cycle is repeated 12000 times, that is a total experimental time of 300 s. Every 300 s$-$cycle is repeated for different values of the amplitude of the random force $\xi(t)$, starting with the case where no external force is applied.

The relaxation time for the particle position is $\tau_r = \gamma_m/\kappa_x = 0.5$ ms where $\gamma = 8.4$ pN ms/μm is the friction coefficient. The time spent by the trap in the fixed stage of the protocol then exceeds by one order of magnitude the calculated relaxation time, which should be enough to make sure the particle reaches equilibrium before the next step of the protocol. In the dragging steps, the viscous dissipation is of the order of $\langle W_{\text{diss}} \rangle \sim \gamma_m \langle \dot{x} \rangle L$[78], where $L = 110$ nm is the distance travelled by the trap, which yields $\langle W_{\text{diss}} \rangle \sim 20$ pN nm $\simeq 5\, kT$ indicating that the work dissipation cannot be neglected and the system is therefore out of equilibrium. In this case, the control parameter is the position of the trap centre, $\lambda = x_0$, and therefore the work is calculated as

$$W = \int \frac{\partial U}{\partial x_0} \circ dx_0(t) = \int -\kappa(x(t) - x_0(t)) \circ dx_0(t), \tag{2.20}$$

for every realization of the forward and backward processes.

Figure 2.6 shows the work distributions at different noise intensities for both forward and backward dragging processes. When increasing the noise amplitude, the average work remains constant but the variance increases. Since in this process, the free energy does not change, $\Delta F = 0$, the average work coincides with the average dissipation rate $\langle W \rangle = \langle W_{\text{diss}} \rangle$. Therefore, the addition of the external random force does not introduce an additional source of dissipation. The work distributions at different noise amplitudes fit to theoretical Gaussian distributions obtained from reference.[78] using T_C as the only fitting parameter in the asymmetry function, as indicated by Eq. (2.18). Note also that both work distributions cross at $W = 0$, since $\Delta F = 0$.

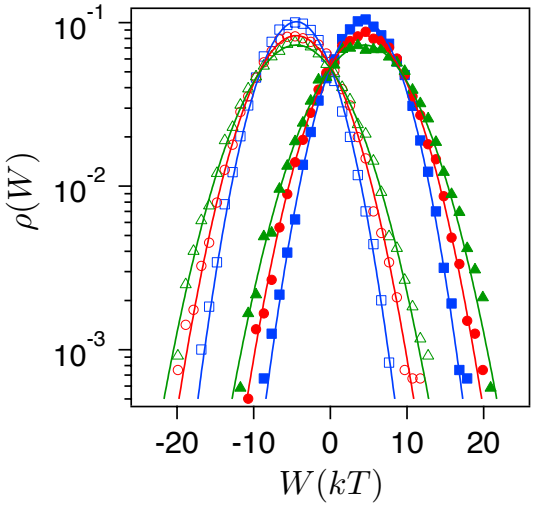

Figure 2.6: Work distributions in the forward ($\rho(W)$, filled symbols) and backward ($\tilde{\rho}(-W)$, open symbols) dragging experiments depicted in Fig. 2.5. Different symbols and colours correspond to different noise intensities, yielding the following values of the Crooks temperature: $T_c = 525\,\mathrm{K}$ (blue squares) $T_c = 775\,\mathrm{K}$ (red circles) and $T_c = 1010\,\mathrm{K}$ (green triangles). Solid lines are the theoretical values of the work distributions obtained for the same values of kinetic temperatures. Work was calculated from trajectories sampled at $f = 10\,\mathrm{kHz}$.

Discussion

As we discussed, if we want this technique to be applicable to the design of nonequilibrium thermodynamic processes, we require that the equilibrium and nonequilibrium kinetic temperatures, that is T_{CM} and T_c, coincide within experimental errors. However, some discrepancies were found in reference[78] when the sampling frequency was changed, and their origin could not be fully understood.

In order to clarify this issue, we now compare the values of T_{kin} and T_c obtained for different values of the noise amplitude and different acquisition frequencies, ranging from 1 kHz to 10 kHz. Figure (2.7a) shows that equilibrium and nonequilibrium effective temperatures do coincide within experimental errors when the sampling rate exceeds $f = 2$kHz. When changing the position acquisition frequency, the value of T_{CM} does not change, whereas T_c changes significantly up to a saturating value, reached when $f \simeq 2$ kHz. This deviation between equilibrium and nonequilibrium kinetic temperatures for certain values of the data acquisition rate could be a drawback for our setup to be applicable to design nonequilibrium thermodynamic processes at the mesoscale.

We can get a deeper understanding of the mismatch between T_{kin} and T_c by simulating the overdamped Langevin equation (1.34) and taking into account the cut-off of the random force at $f_{\text{co}} = 3$ kHz recently observed in reference.[99]. Simulations follow an Euler numerical scheme[92] with a simulation time step of $\Delta t = 10^{-3} ms$. The values of all the external parameters are set to those of the experiment. The spectrum of the external force is flat up to a cut-off frequency of $f_{\text{co}} = 3$ kHz and its amplitude is arbitrarily set to a value σ such that $\sigma^2/2k_b\gamma_m = 500$ K. Such random force was attained by generating a Gaussian white noise signal and applying a filter with a cut-off frequency $f_{\text{co}} = 3$ kHz and followed by an inverse Fourier transform.

With the simulations we investigate if the difference between T_c and T_{CM} at low sampling frequencies can be assessed by our model. Figure (2.7b) shows the values of the quotient

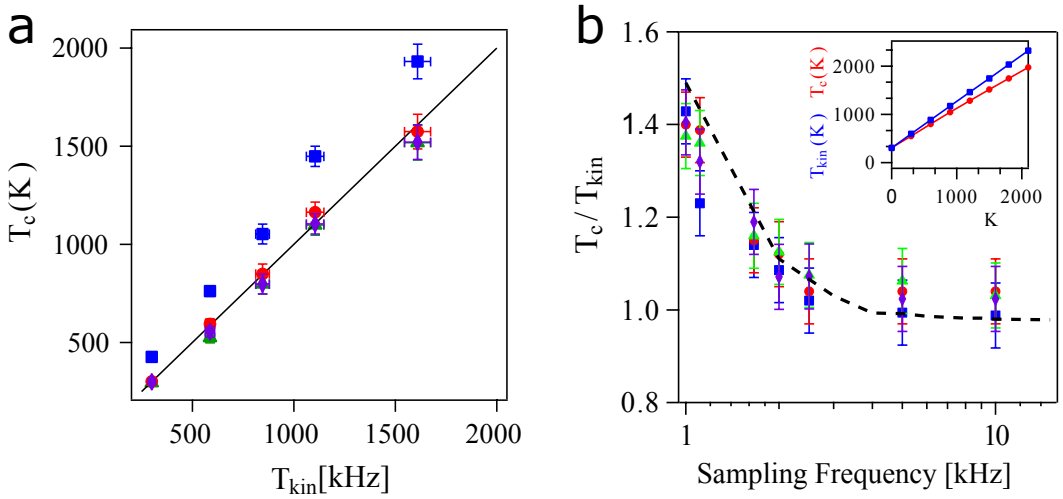

Figure 2.7: **a** Comparative of the temperature found for an equilibrium (T_{CM}) and non equilibrium process (T_C). Different symbols correspond to results obtained for different sampling rates: 1 kHz (blue squares), 2 kHz (red circles), 5 kHz (green triangles) and 10 kHz (magenta diamonds). Solid black line corresponds to Tc = Tkin. **b** Values of the quotient $T_c/T_{\rm kin}$ in the dragging experiment as functions of the sampling frequency for different values of the external field, corresponding to the kinetic temperatures: $T_{\rm kin} = 525\,{\rm K}$ (blue squares), $T_{\rm kin} = 775\,{\rm K}$ (red circles), $T_{\rm kin} = 1010\,{\rm K}$ (green triangles) and $T_{\rm kin} = 1520\,{\rm K}$ (magenta diamonds). We also show the value of $T_c/T_{\rm kin}$ as a function of the sampling frequency obtained from numerical simulations of the overdamped Langevin equation for an external noise with flat spectrum up to $f_{\rm co} = 3\,{\rm kHz}$ and intensity $\sigma^2/2k\gamma = 500\,{\rm K}$ (black dashed curve). Inset: $T_{\rm kin}$ (blue squares) and T_c (red circles) as a function of noise intensity, $\sigma^2/2k\gamma$, for the experimental values of the experiment described in Ref.[78]. Solid lines are included to guide the eye.

T_c/T_{CM} as a function of the sampling frequency plotted for different values of the external field corresponding of those described in the caption of Fig. (2.6). The solid black line in Fig. 2.7 shows that the value of T_c/T_{kin} as a function of the sampling frequency, as obtained from the numerical simulations, is in well agreement with the experimental measurements. The results in Fig. 2.7 indicate that sampling at frequencies above the noise cut-off frequency does not yield any difference in the nonequilibrium measurements. When sampling close to the corner frequency of the trap, $f_c = \frac{\kappa}{2\pi\gamma} = 340$ Hz in this case, equilibrium and nonequilibrium kinetic temperatures do not coincide, and T_c is above its equilibrium counterpart, $T_c > T_{\mathrm{kin}}$.

Interestingly, the opposite result ($T_c < T_{\mathrm{kin}}$) was reported in Ref.[78] for a similar dragging trap experiment. From the experimental point of view, we may note that in the present work, the noise cut-off frequency given by the amplifier is one order of magnitude larger than the one in Ref.[78], and therefore the drawbacks of a coloured spectrum of the noise are reduced. In the inset in Fig. (2.7), we show that our model predicts this different behaviour when using the experimental data in the experiment in Ref.[78] ($f_{\mathrm{co}} = 1$ kHz, $\kappa = 6$ pN/μm, $\tau_1 = \tau_2 = 6.3$ ms and $L = 122$ nm for instance). Therefore, the relation between T_c and T_{kin} is complex and very sensitive to the values of the experimental parameters.

From this discussion, we can conclude that a sampling frequency $f = 2$ kHz is optimal for the experiment we describe next, since it is below any relaxation of the external force (~ 3 kHz), above the corner frequency (~ 300 Hz) and does not unnecessarily store redundant data.

Experimental Results: Isothermal Expansion

As a second application of our technique, we analyse a different thermodynamic process consisting in a "breathing" harmonic potential, where the trap centre is held fixed but its stiffness is changed with time from an initial κ_{ini} to a final κ_{fin} value. Since the stiffness of the trap can be thought of as the inverse characteristic volume of the system, $\kappa \sim 1/V^{15}$, such process is equivalent to an isothermal compression or expansion. At odds with the dragging process, in this case the free energy changes along the process, yielding $\Delta F = kT_{\mathrm{kin}} \ln \sqrt{\kappa_o/\kappa_f}^{112}$. This

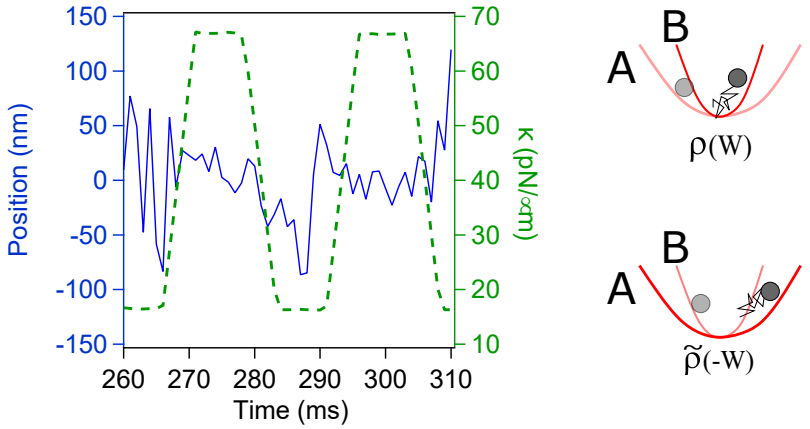

Figure 2.8: Position of the particle (blue line, left axis) and trap stiffness (green line, right axis) as functions of time in the isothermal compression-expansion cycle. Sampling rate, $f = 2\,\mathrm{kHz}$. The process is illustrated on the right panel.

process becomes significant for two reasons, first it has a free energy $\Delta F \neq 0$ that depends on the temperature. Secondly because is a thermodynamic process which can be used to extract energy from a thermal bath thus having relevance in several heat engine cycles.

The experimental protocol is shown in Fig. 2.8, the trap is initially held fixed with stiffness $\kappa_1 = (16.5 \pm 0.2)\mathrm{pN}/\mu\mathrm{m}$ for $\tau_1 = 3.5$ ms. Then, the system is isothermally compressed by increasing the stiffness up to $\kappa_2 = (66.8 \pm 0.2)pN/\mu\mathrm{m}$ in $\tau_2 = 2.5$ ms. Further, the particle is allowed to relax to equilibrium for $\tau_1 = 3.5$ ms with the trap stiffness held fixed at κ_2 before the system is isothermally expanded from κ_2 to κ_1 in $\tau_2 = 2.5$ ms. Every cycle lasts $\tau = 2(\tau_1 + \tau_2) = 12$ ms and is repeated 24000 times for different values of the amplitude of the external random force.

For every isothermal compression (forward process) and expansion (backward process), the trap position is fixed, and κ our control parameter, thus we measure work as:

$$W = \int \frac{\partial U}{\partial \kappa} \circ d\kappa(t) = \int \frac{1}{2} x^2(t) \circ d\kappa(t), \tag{2.21}$$

Figure (2.9) shows the distributions of the work (minus the work) in the forward (backward) process of increasing (decreasing) the stiffness of the trap (see Fig. 2.8) for different

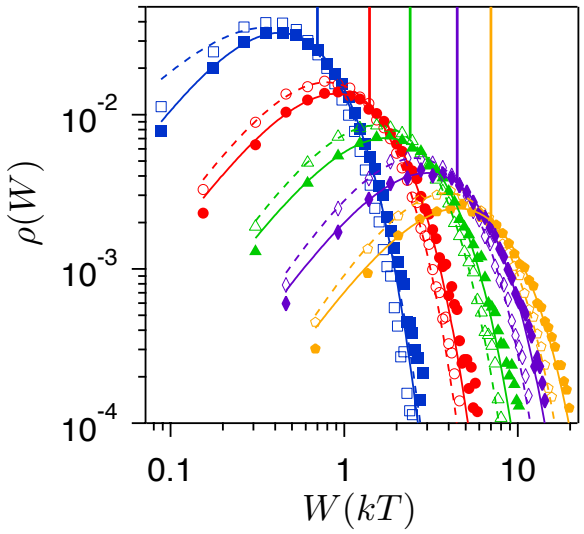

Figure 2.9: Work distributions in the isothermal compression [$\rho(W)$, filled symbols] and isothermal expansion [$\tilde{\rho}(-W)$, open symbols] for different values of the noise intensities corresponding to the following nonequilibrium effective temperatures: Without external field, $T_c = 300\,\mathrm{K}$ (blue squares), $T_c = 610\,\mathrm{K}$ (red circles), $T_c = 885\,\mathrm{K}$ (green triangles), $T_c = 1920\,\mathrm{K}$ (magenta diamonds) and $T_c = 2950\,\mathrm{K}$ (orange pentagons). Solid and dashed curves are fits to Eq. (2.22). Vertical lines of the corresponding color show the expected value for the free energy change at the given temperatures. Data acquisition rate to calculate the work: $f = 2\,\mathrm{kHz}$.

values of the external noise amplitude are shown in Fig. 2.9. We notice that the work fluctuations are non-Gaussian for both isothermal compression and expansion, as predicted theoretically in[113]. We find that the work distributions can be fitted with a very good agreement to generalized Gamma distributions,

$$\rho(W) = C_F\, W^{z_F}\, e^{-W/\alpha_F}, \tag{2.22}$$

$$\tilde{\rho}(-W) = C_B\, (-W)^{z_B}\, e^{W/\alpha_B}, \tag{2.23}$$

where the fitting parameters C_F, C_B, α_F and α_B depend on the amplitude of the external noise, but not z_F and z_B. The above result can be justified provided that the work along isothermal compression and expansion is equal to the sum of squared Gaussian variables [see Eq. (2.21)] which is Gamma-distributed[123]. Interestingly, the distributions (2.22) and (2.23) are analogous to that of the work in the adiabatic compression or expansion of a dilute gas[31].

Discussion

The asymmetry between forward (compression) and backward (expansion) work distributions is an indicator of the irreversibility or the nonequilibrium nature of the process. In Fig.(2.9) we show that the forward and backward work histograms cross at the value of the effective free energy change $\Delta F = kT_{\rm CM} \ln \sqrt{\kappa_{\rm fin}/\kappa_{\rm ini}}$ in all cases, with $T_{\rm kin}$ equal to the calibrated equilibrium kinetic temperature. The difference between $\rho(W)$ and $\tilde{\rho}(-W)$ is quantified with the work asymmetry function, Eq.((2.17)), whose values for different noise intensities are shown in Fig. 2.10. The work asymmetry function depends linearly on the work, with its slope equal to $1/k_b T_{\rm kin}$, or equivalently $T_c = T_{\rm kin}$. The inset in Fig. (2.10) shows that this equality holds throughout the range of temperatures we explored up to 3000K. This result implies that our setup is suitable to implement nonequilibrium isothermal compression or expansions in the mesoscale, with the externally controlled temperature verifying all the requirements of an actual one.

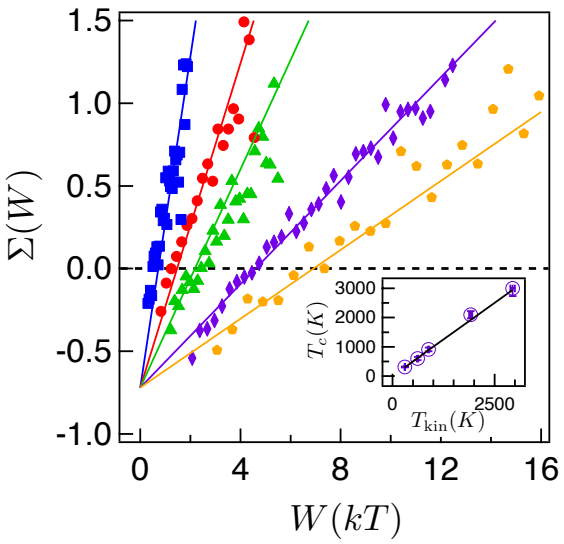

Figure 2.10: Experimental values (markers) and theoretical values (solid lines) of the work asymmetry function obtained from the work distributions in Fig. 2.9. Theoretical curves are computed using the values obtained for $T_{\rm kin}$. Inset: T_c as a function of $T_{\rm kin}$ (open magenta circles, error bars are smaller than the symbol size). The solid line has slope 1.

Conclusions and Outlook

Throughout this chapter we have presented the stochastic thermodynamics formalism which allows us to compute the energy exchange of a microsystem in contact with a thermal bath. Following this formalism, we have demonstrated the possibility to use random forces with a Gaussian white noise spectra in order implement an additional thermal bath whose temperature can be tuned up to several thousands of K. By means of different experiments, we have demonstrated that such a thermal bath provides a consistent temperature for both equilibrium and non-equilibrium processes. In one of these experiments we also found the work distribution for isothermal compressions/expansions, which is a relevant thermodynamic process involved in heat engine cycles. Using our approach it is possible to implement arbitrary stiffness vs. temperature (pressure vs. temperature) curves using an optical trap as an analogy of a piston with a single gas molecule, thus allowing to study the efficiency of heat engines in the microscale. Using this same thermal bath approach two experimental heat engines have been recently implemented: a Carnot cycle with a colloidal particle[76] and an Otto cycle with an single ion in a Paul trap[103] both showing unique features not comparable with their macroscopic counterparts. Some recent proposals also suggested to extend the study of thermodynamics with optical traps to the underdamped regime by following a cavity optomechanics approach[32].

As an outlook we expect that, using the techniques presented in this chapter, it will be possible to implement and test some open questions such as optimal protocols in both overdamped and underdamped regime and in the long term optimize the efficiency of microscopic heat engines in order to bring them from toy models to actual functional devices.

Love is like... coupled harmonic oscillators.

Pau Mestres

3

Cavity Optomechanics with a Levitated Nanoparticle

The field of optomechanics studies systems where an Electromagnetic field interacts with a mechanical oscillator: photons interacting with phonons. By making use of a cavity this interaction can be enhanced and eventually brought to a regime where the quantum properties of both mechanics and optics manifest themselves even at room temperature. This chapter discusses how to achieve optomechanical coupling between a cavity and an optically levitated nanoparticle aiming to cool its centre of mass and prepare a mechanical ground state at room temperature.

Introduction

A typical optomechanical system is formed by a optical cavity with a movable end mirror. The optomechanical coupling arises from the interaction between the end mirror and a light field. The reflected field is phase shifted according to the mirror displacement revealing its position while the field radiation pressure also transfers momentum to the mirror disturbing its motion. The combination of these two phenomena imposes a limit for the sensitivity of these measurements, the so called Standard quantum limit (SQL). The first to realise about it were Braginsky[21] and Caves[23] in the late 70's. They shown that quantum-mechanical radiation-pressure fluctuations of the light field imposed a limit of how accurately the position of a free test mass could be measured, which caused great concern in the context of gravitational wave interferometry. Although it did not limit the performance of interferometers back then, the SQL had striking implications in the future design and implementation of nowadays gravitational wave detectors.

During the 90's the cavity optomechanical interaction was studied as a mechanism to manipulate the quantum properties of the optical field. These include light squeezing[36,73], quantum non-demolition measurement protocols[53,36]and even preparation of non-classical light-matter states in the case of strong interactions[19,72]. Similarly the radiation pressure was proposed as a mechanism to manipulate the mechanical motion of the end mirror and cool or amplify it's center of mass[126].

The first radiation pressure cooling experiment with a macroscopic oscillator was performed by Cohandon et all.[28] in 1999 measuring the displacement of the mirror and applying feedback with an additional laser beam. They managed to bring the vibrational modes of a macroscopic mirror down to few K the at room temperature, limited by the signal readout and coupling to the thermal environment.

The advent of micro and nanofabrication techniques in the 2000's soon allowed to tailor the properties of the mechanical oscillators and tune it's integration with optical cavities in a wide diversity of geometries such as micromirrors at the end of a cantilever[49,85], toroidal[63] and

disc microresonators[10] containing whispering gallery modes, 1D photonic and phononic crystals with co-localized defects[105], membranes capacitively coupled to microwave circuits[94,114], etc.
These micro-optomechanical systems allowed to enter a new regime where the delayed response of the cavity field could be used as a cooling mechanism without need of applying feedback. Additionally, the small size of these devices allowed them to be used in dilution refrigerators greatly decreasing their initial phonon occupation. These two features eventually led to the ground state cooling of some of these optomechanical systems in cryogenic temperature in 2011 by Chan et al.[24] and Teufel et al.[115].

In order to obtain a long lived mechanical quantum state, the mechanical oscillator needs to be decoupled from decoherence sources (typically clamping losses for solid state devices). A figure of merit for this decoupling is given by the $Q \times f$ product. To reach higher Q factors, two proposals[102] suggested in 2010 the use optically trapped nanoparticles in high vacuum as a mechanical oscillator, which could then be coupled to a macroscopic Fabry-Perot cavity. Actually, the predicted decoupling from the environment was so large that these systems could be used to reach ground state even at room temperature.

Since then several groups started working with levitated nanoparticles using different geometries of optical trapping such as counter-propagating traps[66,86,93], optical cavities[62,82], single beam optical tweezers[82,44,54], parabolic mirrors[125] and even Paul traps[87]. These groups have demonstrated feedback cooling, cavity cooling and optical manipulation of nanoparticles in vacuum in many among other optomechanical features. Yet ground state remains unachieved due to the technical demands of such experiment.

Here we present our work towards the milestone of ground state cooling at room temperature. We will start with a semiclassical description of the elements in the experiment: the optical cavity and a levitated nanoparticle. Then, we will consider different techniques to cool the centre of mass of our particle and the different detection methods that provide enough sensitivity to resolve the ground state, provided the SQL. Finally we will present our setup where we have implemented several cooling techniques and give a current benchmark

of its capabilities that meet the needs to reach ground state.

Quantum harmonic oscillator

As in the case of classical physics, the harmonic oscillator is one of the few analytical solvable systems in quantum mechanics. It has a huge impact in most of the branches of modern physics - molecular spectroscopy, solid state physics, nuclear structure, quantum field theory, quantum optics and so forth- and will be also describe our optically trapped particles and light fields.

The basic Hamiltonian of a mechanical harmonic oscillator is

$$H = \frac{\mathrm{p}^2}{2m} + \frac{m\Omega^2 \mathrm{x}^2}{2} \tag{3.1}$$

where m represents the mass and Ω the frequency of the oscillator and we have converted the classical observables of momentum p and position x into Hermitian operators via canonical quantization $[\mathrm{x}, \mathrm{p}]=i\hbar$. We want also to define the annihilation a, creation $a^\dagger$ and number N operators as[106]:

$$a = \sqrt{\frac{m\Omega}{2\hbar}}\left(\mathrm{x} + \frac{i\mathrm{p}}{m\Omega}\right) \tag{3.2}$$

$$a^\dagger = \sqrt{\frac{m\Omega}{2\hbar}}\left(\mathrm{x} - \frac{i\mathrm{p}}{m\Omega}\right) \tag{3.3}$$

$$N = a^\dagger a \tag{3.4}$$

that satisfy the following commutation relations:

$$[N, a] = [a^\dagger a, a] = -a \tag{3.5}$$
$$\left[N, a^\dagger\right] = [a^\dagger a, a^\dagger] = a^\dagger \tag{3.6}$$

Using Eqs.(3.4-3.2) we can rewrite the Hamiltonian as:

$$H = \hbar\Omega\left(N + \frac{1}{2}\right) \tag{3.7}$$

which to satisfies the Schrödinger wave equation[106]:

$$H\psi_n(x) = \left(n + \frac{1}{2}\right)\hbar\Omega\psi_n(x) \tag{3.8}$$

where we denoted the energy eigenfunctions by their eigenvalue n. This eigenfunction representation is also known as Fock states.

The lowest energy level is ground state and its wavefunction in the x representations reads

$$\psi_0(x) = \left(\frac{m\Omega}{\pi\hbar}\right)^{1/4} e^{-\frac{m\Omega}{2\hbar}x^2} \tag{3.9}$$

with energy $\hbar\Omega/2$ and the so-called zero-point fluctuations x_{zpf} which corresponds to the minimum displacement that satisfies the Heisenberg uncertainty principle[106]:

$$x_{zpf} = \sqrt{(\langle x_o^2\rangle - \langle x_o\rangle_0^2)} = \sqrt{\frac{\hbar}{2m\Omega}} \tag{3.10}$$

Using the commutation relations in Eq.(3.6) we can find the n^{th} eigenfunction $\psi_n(x)$ by recursively applying $a^\dagger$:

$$\psi_n(x) = \sqrt{\frac{1}{n!}}(a^\dagger)^n\psi_0(x) \tag{3.11}$$

To each eigenfunction $\psi_n(x)$ corresponds an energy level $\left(n+\frac{1}{2}\right)\hbar\Omega$. This evenly spaced energy levels correspond to the discrete quanta of excitation of the system, photons for a light field and phonons for a mechanical oscillator. Yet, these higher energy states do not agree very well with our macroscopic experience of an harmonic oscillator consisting of a localized wave packet oscillating in in space .

Coherent States

The quantum representation of a state that mostly resembles a classical oscillator is the so-called coherent state which was described by Glauber[47]. This state describe well for example the output field of a laser, and writes in the Fock state basis as[106]:

$$|\alpha\rangle = e^{-|\alpha|^2/2}\sum_{n=0}^{\infty}\frac{\alpha^n}{\sqrt{n!}}|n\rangle \tag{3.12}$$

Where α is the complex amplitude of the field in units of the mean number of quanta:

$$\langle N\rangle = \langle\alpha|N|\alpha\rangle = \langle\alpha|a^\dagger a|\alpha\rangle = \alpha^*\alpha = |\alpha|^2 \tag{3.13}$$

When we measure the energy of a coherent state (e.g. a laser beam), the probability to find n quanta (e.g. photons)is:

$$P(n) = |\langle n|\alpha\rangle|^2 = e^{-|\alpha|^2}\frac{|\alpha|^{2n}}{n!} = \frac{\bar{n}^n}{n!}e^{-\bar{n}} \tag{3.14}$$

corresponding to a Poissonian distribution.
A physical picture of coherent states consists on a ground state that has been displaced to higher energies by means of the displacement operator $D(\alpha) = exp(\alpha^\dagger a - \alpha^* a)$ while maintaining the minimum uncertainties according to Heisenberg's uncertainty principle. This higher energy state then oscillates periodically in the (p, q)space and can be related classical picture of a particle oscillating with an amplitude equal to the displacement. An other important feature of coherent states is that an attenuation transforms them into another coherent

state with smaller relative amplitude[9], which also agrees with the classical picture of motion attenuation of an harmonic oscillator. and is what we do when cooling the centre of mass of an optically trapped particles.

Quadrature Operators

Since field amplitudes are represented by a complex amplitude α, we use a two dimensional representation. For a mechanical oscillator, one can use position and momentum as coordinates; for the optical field we have the amplitude and phase. Unfortunately, phase operators do not have a simple quantum mechanical representation, thus it will be more convenient to work with the quadrature amplitude operators (i.e. real and imaginary part of a):

$$\mathrm{p} = a + a^\dagger \quad \text{and } \mathrm{q} = i(a^\dagger - a) \tag{3.15}$$

Whose uncertainty satisfies $\langle \delta p^2 \rangle \langle \delta q^2 \rangle \geq 1$ (=1 for a coherent state). We can extend their use in the semiclassical picture by taking the average $\langle a \rangle \to \alpha$. Hence, we can use the quadrature operators to characterize our system in both quantum and classical picture in a plot p vs. q. For a coherent state this is an ellipse centred at $(\langle \mathrm{p} \rangle, \langle \mathrm{q} \rangle)$ with radius$\langle \mathrm{p}^2 \rangle$ and whose area represents the uncertainty principle [*].

Optical Cavities

Optical cavities are elements extensively used in optics experiments starting by their presence in every laser. The simplest picture of a cavity consists of two opposed highly reflective mirrors with radius of curvature r_1 and r_2. In order for a cavity of length L to be stable, it needs to satisfy the following stability criterion[107]:

[*]This semiclassical picture is suitable to represent the so called Gaussian States (Ground State, coherent states and even squeezed states), which are the ones we will work throughout this thesis. To represent other quantum states such as Fock States one should use Quasi-Probability distributions such as the Wigner Function representation. We refer to[9] for more details

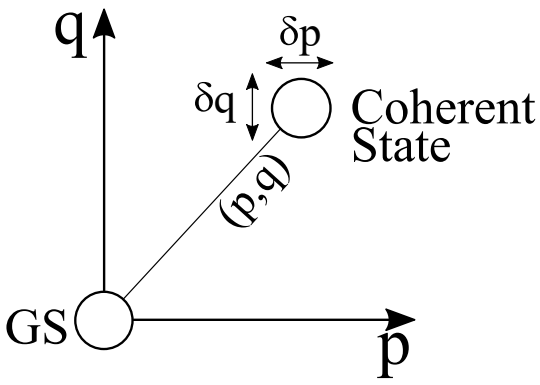

Figure 3.1: 2D semiclassical representation of a Ground State (GS) and a Coherent state. Both of them are represented by the same area uncertainty ellipse, but the coherent state has been displaced to higher values of p and q. The coherent state rotates in the phase space diagram as our macroscopic perspective of a mechanical oscillator.

$$0 \leq \left(1 - \frac{L}{r_1}\right)\left(1 - \frac{L}{r_2}\right) \leq 1 \tag{3.16}$$

This criterion allows for several stable geometries as discussed in[107]. We choose a confocal geometry since they offer higher tolerances against misalignment.

The optical properties of a cavity are most easily derived using a classical picture of multiple interfering waves[9]. Consider an incident field at frequency ω_L and amplitude α_{in}. For a coupling mirror with transmission T_1, the amplitude transmitted into the cavity is $\alpha_o = \sqrt{T_1}\alpha_{in}$. Now, the field reflected in the cavity is attenuated every roundtrip by

$$g_m = \sqrt{R_1 R_2 A D} \tag{3.17}$$

where R_1 and R_2 are the mirror reflectivities, A the absorption and D the diffraction losses. Additionally the field accumulates a phase $\delta\phi = \omega_L 2L/c$ mod. $[2\pi]$. As a result the internal cavity field arises from the interference of the coupled field with its successive reflections:

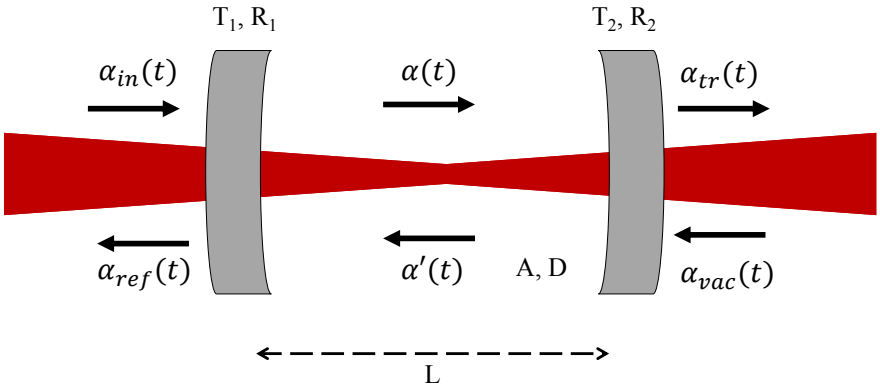

Figure 3.2: Representation of a confocal optical cavity of length L. The cavity input mirror has a transmission T_1 and reflection R_1, and the output mirror has a transmission T_2 and R_2. The cavity also features absorption A and diffraction D losses. The amplitude of the different fields considered for the cavity are α_{in} for the field we send to it, α_{ref} for the reflected field, α and α' as the intracavity fields at different points of the roundtrip, and α_{tr} as the cavity transmitted field and α_{vac} as the vacuum field fluctuations entering through the output mirror.

$$\alpha = \sum_{k=0}^{\infty} \alpha_o \left(g_m e^{\delta\phi}\right)^n = \frac{\alpha_o}{1 - g_m e^{\delta\phi}}. \tag{3.18}$$

This leads to an intracavity power

$$P_{cav} = \frac{|\alpha_o|^2}{|1 - g_m e^{\delta\phi}|^2} = \frac{|\alpha_o|^2}{(1 - g_m)^2 + 4 g_m \sin^2(\delta\phi/2)} = P_o \frac{1}{1 + (2F/\pi)^2 \sin^2(\delta\phi/2)} \tag{3.19}$$

Where $P_o = (\alpha/(1-g_m))^2$ is the maximum power at resonance and F is the so called cavity finesse:

$$F = \frac{\pi\sqrt{g_m}}{1 - g_m} \tag{3.20}$$

The finesse is a measure of the cavity quality and typically is determined by the reflectivity of the mirrors. Note however, that this not entirely true in the presence of an intracavity medium and further losses included in the term g_m.

Equation (3.19) shows a periodic maximum cavity response with the field accumulated dephase $\delta\phi$. These maxima correspond to the different cavity resonance frequencies ω_c and are spaced by the so-called free spectral range:

$$\Delta\omega_{FSR} = \pi\frac{c}{L} \tag{3.21}$$

Equations (3.19, 3.23) also show that high Finesse cavities can build up very high intracavity power when at resonance ($\delta\phi = 0$).
When the driving field α_{in} of a resonant cavity is switched off α will decays at an exponential rate:

$$\alpha_{cav}(t) = \alpha_{cav}(t=0)e^{-\kappa t/2} \tag{3.22}$$

with $\kappa = (c/2L)(1 - g_m)$. In other words, κ are the losses during one cycle divided by the roundtrip time.

Fiting this decay constant allows experimentally measure the cavity Finesse at high reflectivities as

$$F = \Delta\omega_{FSR}/\kappa \tag{3.23}$$

For the specific case of high Finesse cavities ($g_m \ll 1$), losses can be considered small and will come from the input T_1 absorption (A), diffraction (D) and leakage of the field through the end mirror (T_2). Assuming these terms are small we can linearise and group them into a loss term γ_o as

$$2\gamma_o = T_1 + A + D + T_2 = T_1 + P \tag{3.24}$$

$$g_m = e^{-\gamma_o} \approx 1 - \gamma_o \tag{3.25}$$

$$\tag{3.26}$$

where P combines the unwanted losses and the transmission of the output mirror. This allows us rewrite the decay rate as

$$\kappa = \frac{2\gamma_o\Delta\omega_{FSR}}{\pi} \tag{3.27}$$

Cavity Equations of Motion

Input-Output formalism

In this section we want to derive the equations of motion of a High Finesse cavity fields that will be necessary to describe the optomechanical interaction with our levitated nanoparticle. We will use a semiclassical description where fields are linearised at their mean value and then consider the quantum uncertainties as classical fluctuations. This assumptions are justified since we will always consider optical fields with large number of photons ($n \gg 10^8$). For a full quantum description of the cavity we refer to[9].

Figure (3.2) depicts a confocal Fabry Perot Cavity with the different fields considered. Using energy conservation at the mirrors we find the following field relations at the inputs/outputs of the the cavity:

$$\alpha_{ref}(t) = \sqrt{T_1}\alpha(t) - \sqrt{1-T_1}\alpha_{in}(t) \tag{3.28}$$

$$\alpha_{tr}(t) = \sqrt{P}\alpha(t) - \sqrt{1-P}\alpha_{vac}(t) \tag{3.29}$$

Next we consider the evolution of the intracavity field $\alpha(t)$ when the cavity experiences a change $\delta x(t)$ in its optical length $L(t)$. If this change is small compared with λ/F, the cavity roundtrip time remains $\tau \approx 2L/c$ and the field gains phase $\Phi = 2k\delta x$. This modifies the circulating amplitude as :

$$\alpha(t+\tau) = \alpha(t)e^{i\Phi}\sqrt{1-T_1}\sqrt{1-P} + \alpha_{in}e^{i\Phi}\sqrt{T_1}\sqrt{1-P} + \alpha_{vac}e^{i\Phi}\sqrt{P} \tag{3.30}$$

Taylor expanding on both sides and keeping only the leading terms we obtain

$$\alpha(t) + \tau\dot{\alpha}(t) = \alpha(t)\left(1 + i\Phi - \frac{T_1}{2} - \frac{P}{2}\right) + \alpha_{in}\sqrt{T_1} + \alpha_{vac}\sqrt{P} \tag{3.31}$$

Finally we can rewrite this last expression and the boundary conditions (Eqs.3.28, 3.29) in

the so-called input-output form[27]:

$$\tau\dot{\alpha} = \alpha(i\delta\Phi - \gamma_o) + \alpha_{in}\sqrt{T_1} + \alpha_{vac}\sqrt{P} \tag{3.32}$$

$$\alpha_{ref} = \sqrt{T_1}\alpha - \alpha_{in} \tag{3.33}$$

$$\alpha_{tr} = \sqrt{P}\alpha - \alpha_{vac} \tag{3.34}$$

To solve the cavity equations of motion, we linearise them and take a semiclassical picture, where the field and its phase shift are described by a constant steady state value $\bar{\alpha}$ and $\bar{\Phi}$ plus a time fluctuating term $\delta\alpha$ and $\delta\Phi = 2k\delta x$:

$$\alpha(t) = \bar{\alpha} + \delta\alpha(t) \tag{3.35}$$

$$\Phi = \bar{\Phi} + 2k\delta x(t) \tag{3.36}$$

To find the steady states we set $\dot{\alpha} = 0$ and then substitute the expression for $\bar{\alpha}$ in Eqs.(3.33, 3.34):

$$\bar{\alpha} = \frac{\sqrt{T_1}}{\gamma_o - i\bar{\Phi}}\bar{\alpha}_{in} \tag{3.37}$$

$$\bar{\alpha}_{ref} = \frac{T_1/2 - P/2 + i\bar{\Phi}}{\gamma_o - i\bar{\Phi}}\bar{\alpha}_{in} \tag{3.38}$$

$$\bar{\alpha}_{tr} = \frac{\sqrt{TP}}{\gamma_o - i\bar{\Phi}}\bar{\alpha}_{in} \tag{3.39}$$

Note that we have considered the mean vacuum field entering the unused cavity mirror $\langle\alpha_{vac}\rangle = 0$ as it only introduces fluctuations.

Figure (3.3) shows the Lorentzian power and phase response of the different cavity fields as a function of the cavity detuning $\Delta = \delta\Phi/\tau$ for a realistic cavity. We see that due to the

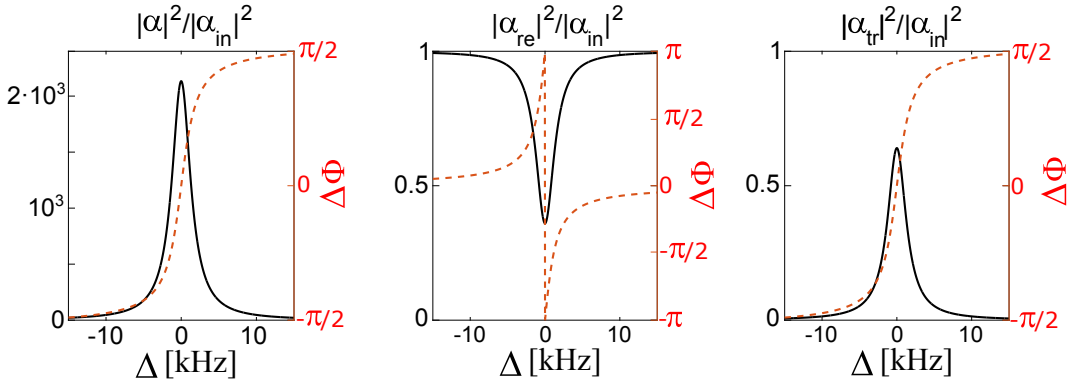

Figure 3.3: Power (solid line) and phase (red dashed line) cavity response for the intracavity α, reflected α_{re} and the transmitted α_{tr} fields. Fields are calculated for a realistic for a confocal cavity of length $L = 2.5cm$, assuming perfect mode matching, coupling mirror transmission $T_1 = 0.4ppm$ and additional losses of$P = 1ppm$.

additional losses, the normalised reflected and transmited powers do not reach 0 and 1 respectively in resonance. This photon losses result in a loss of the information that can be retrieved from the system.

Regarding the phase response we see that the reflected light shows a very sharp phase response (sharper than the linewidth), which will be useful for the cavity locking techniques, wheareas the intracavity and transmitted fields show a smoother frequency response. Additionally, all fields are in phase at resonance:

$$\bar{\alpha} = \frac{\sqrt{T_1}}{\gamma_o}\bar{\alpha}_{in}, \quad \bar{\alpha}_{ref} = \frac{T_1 - P}{\gamma_o}, \quad \bar{\alpha}_{tr} = \frac{\sqrt{T_1 P}}{\gamma_o}\alpha_{in} \tag{3.40}$$

Propagation of fluctuations through the cavity

We proceed in our description of the cavity by treating the propagation of fluctuations. This will allow us to describe the cavity when used as a measurement device for the particle position fluctuations.

We start by considering resonant cavity and rewrite the equations of motion (Eqs. 3.32, 3.33 and 3.34) for the field fluctuations (Eqs. 3.35 and 3.36) and Fourier transform them to obtain the equations of motion in the frequency space :

$$
\begin{aligned}
(\gamma_o - i\tau\Omega)\delta\alpha[\Omega] &= \sqrt{T_1}\delta\alpha_{in}[\Omega] + \sqrt{P}\delta\alpha_{vac}[\Omega] + i\bar{\alpha}\delta\Phi[\Omega] && (3.41)\\
\delta\alpha_{ref}[\Omega] &= \sqrt{T_1}\delta\alpha[\Omega] - \delta\alpha_{in}[\Omega] && (3.42)\\
\delta\alpha_{tr}[\Omega] &= \sqrt{P}\delta\alpha[\Omega] - \delta\alpha_{vac}[\Omega] && (3.43)
\end{aligned}
$$

Due to the aforementioned inconvinience to write a phase operator, we rewrite these equations to the quadratures (Eq. 3.15):

$$
\delta\alpha[\Omega] = \frac{\delta p[\Omega] + i\delta q[\Omega]}{2}, \quad \delta\alpha^*[\Omega] = \frac{\delta p[\Omega] - i\delta q[\Omega]}{2} \tag{3.44}
$$

Combining Eqs. (3.43,3.44) we rewrite the intracavity, reflected and transmitted fluctuations as a function of the incident field and cavity phase fluctuations $\delta p_{in}, \delta q_{in}, \delta\Phi$:

$$
\begin{aligned}
\delta p[\Omega] &= \frac{\sqrt{T_1}\delta p_{in}[\Omega] + \sqrt{P}\delta p_{vac}[\Omega]}{\gamma_o - i\tau\Omega} && (3.45)\\
\delta q[\Omega] &= \frac{\sqrt{T_1}\delta q_{in} + \sqrt{P}\delta q_{vac}[\Omega] + 2\bar{\alpha}\delta\Phi[\Omega]}{\gamma_o - i\tau\Omega} && (3.46)\\
\delta p_{ref}[\Omega] &= \frac{(\gamma_o - P + i\tau\Omega)\delta p_{in}[\Omega] + \sqrt{T_1 P}\delta p_{vac}[\Omega]}{\gamma_o - i\tau\Omega} && (3.47)\\
\delta q_{ref}[\Omega] &= \frac{(\gamma_o - P + i\tau\Omega)\delta q_{in}[\Omega] + \sqrt{T_1 P}\delta q_{vac}[\Omega] + 2\sqrt{T_1}\bar{\alpha}\delta\Phi[\Omega]}{\gamma_o - i\tau\Omega} && (3.48)\\
\delta p_{tr}[\Omega] &= \frac{(\gamma_o - T_1 + i\tau\Omega)\delta p_{vac}[\Omega] + \sqrt{T_1 P}\delta p_{in}[\Omega]}{\gamma_o - i\tau\Omega} && (3.49)\\
\delta q_{tr}[\Omega] &= \frac{(\gamma_o - T_1 + i\tau\Omega)\delta q_{vac}[\Omega] + \sqrt{T_1 P}\delta q_{in}[\Omega] + 2\sqrt{P}\bar{\alpha}\delta\Phi[\Omega]}{\gamma_o - i\tau\Omega} && (3.50)
\end{aligned}
$$

These set of equations shows two interesting features for a resonant cavity. First we see that at resonance the intensity fluctuations δp are decoupled from the phase fluctuations of the excitation fieldδq and cavity $\delta\Phi$. Thus to extract information about δq and $\delta\Phi$ it is nec-

essary to set an interferometric readout. This is can be understood by noting that we work in the maximum of the cavity amplitude response (see Fig.3.3) where the derivative of the intensity with the detuning is 0 and the derivative in the phase response is maximal. If we work with a non-zero detuning steady state ($\tau\Omega \neq 0$), noise fluctuations in a single quadrature of the excitation field will be projected into both quadratures of of the transmitted field. Hence one can project intracavity phase fluctuations into transmitted intensity fluctuations by measuring with a detuned cavity.

Furthermore, we note that high frequency components in the fluctuations δq_{in} and δp_{in} impinging the coupling mirrors are reflected by the cavity and low-pass filtered to δp_{tr} via a transfer function:

$$\langle \delta p_{tr}[\Omega]^2 \rangle \propto \frac{\langle \delta p_{in}[\Omega]^2 \rangle}{(\gamma_o)^2 + (\tau\Omega)^2} \tag{3.51}$$

The same happens for the intracavity phase fluctuations caused by $\delta\Phi[\Omega]$, where the cavity acts as an integrator that averages the phase fluctuations during the photon storage time. These features allow for example the use of narrow linewidth optical cavities as passive noise filters for laser systems that are not quantum noise limited. Similarly it also becomes a limitation to access modulations of the intracavity field at frequencies larger than the cavity bandwidth $\Omega_c = \gamma_o/\tau$, limiting our sensitivity for intracavity measurements.

Limits in interferometric measurements

With the equations describing the cavity field and a BFP interferometry measurement (see. Chapter 1) we can compare theoretically the sensitivity of the two different readout techniques and elucidate which is more suitable to resolve the zero-point-fluctuations x_{zpf} of an optically levitated nanoparticle. In this section we will derive the sensitivity limit of each approach taking into account the SQL, and discuss the advantages of each different approaches. We will start by considering the BFP case and then the case of a particle coupled to a cavity.

We first consider sensitivity limit imposed by the photon shot noise statistics also known as imprecision noise. Taking the linearised intensity response of the BFP signal from Eq. (1.57) in units of photon rate n (i.e. the power imbalance between the two halves in the BFP caused by a particle displacement δx in an optical trap formed by a stream of n photons/s) yields:

$$\delta n = M\frac{16}{\sqrt{\pi}}\frac{k\alpha}{4\pi\epsilon_o w_o^3}n\delta x \tag{3.52}$$

Where the factor $M = 0.675$ adjusts the slope of the analytic paraxial approximation to the high NA numerical calculation (see Fig.1.6).
Comparing δn to the reference field intensity fluctuations ($\delta n_{shot} = \sqrt{n}$), we find that the shot-noise limit of the BFP corresponds to a fluctuating spectra

$$S_{xx}^{sh} = \frac{1}{nM^2}\left(\frac{4\pi^{3/2}\epsilon_o w_o^3}{16k\alpha}\right)^2 \approx \frac{3.82\cdot 10^{-6}}{n}\mathrm{m^2Hz^{-1}} \tag{3.53}$$

where numerical results correspond to our trap geometric parameters NA$= 0.8$, $\lambda = 1550$ nm and $w_o = \lambda/(2\mathrm{NA})$.

Next, using Eqs.(1.22, 1.38 and 3.10) we want to rewrite the mechanical frequency Ω_m and the corresponding x_{zpf} as a function of n:

$$\Omega_m = \sqrt{\frac{4\alpha\hbar\omega n}{\pi\epsilon_o c w_o^4 m}}, \quad x_{zpf}^2 = \frac{1}{4}\sqrt{\frac{\pi\epsilon_o c w_o^4\hbar}{n\alpha\omega m}} \tag{3.54}$$

Finally, we consider the backaction noise. Namely the random driving force acting on our particle due to the randomly arriving photons and their scattering. The force acting on a particle along an axis i is $F_i = P_{scatt}^i/c$. For a shot noise limited optical trap the power

spectral density of the scattered power is[54]:

$$S_{PP_i}(\Omega) = \int_{-\infty}^{\infty} \langle P_{scatt}(\Omega) P^*_{scatt}(\Omega') \rangle_i d\Omega' = \frac{\hbar\omega_l}{2\pi} P_{scatt}(\Omega)_i \tag{3.55}$$

For a beam polarized along the x axis our particle becomes an x oriented dipole that scatters in a radiation pattern $f(\theta, \phi) = (3/8\pi)\sin^2\theta$. As a result the scattered power is split in 3 components, corresponding to $P^x_{scatt} = (2/5)P_{scatt}$, $P^y_{scatt} = (2/5)P_{scatt}$ and $P^z_{scatt} = (1/5)P_{scatt}$ and finally

$$S^x_{FF}[\Omega] = \frac{2(\hbar\omega_l)^2}{5\pi c^2}\sigma\frac{n}{\pi w_o^2} \tag{3.56}$$

where σ is the scattering cross-section:

$$\sigma = \frac{\alpha^2 k^4}{\varepsilon_o^2 6\pi} \tag{3.57}$$

Multiplying the random force by the amplitude response (Eq. 1.46) of the mechanical oscillator and integrating over the frequency space we obtain the mean square displacement of the position fluctuations introduced by backaction:

$$S^b_{xx} = \frac{2(\hbar\omega)^2}{5\pi c^2}\sigma\frac{n}{\pi w_o^2}\frac{\pi}{\Gamma(m\Omega_m)^2} = \frac{\alpha k^4 w_o^2 \hbar\omega}{60\pi c\Gamma m\epsilon_o} \tag{3.58}$$

This result shows some very unique features. First, backaction for levitated nanoparticles is strongly dependent on the wavelength but not on the particle size, since its volume contained in both m and α. This results from the fact that the depth of our optical potential depends on the particle volume as well as the kinetic energy of the harmonic oscillator.
This equation also shows that backaction can be lowered by increasing the mechanical dissipation on the levitated nanoparticle Γ, thus achieving larger values of Γ will make resolving x_{pf} easier. Conversely in the absence of dissipation the particle fluctuations diverge, leading to the particle escaping the potential.

Interestingly, we also observe that the backaction dependence on n differs from to most

of other optomechanical systems where backaction fluctuations tipically scale with n[8]. In our system S^b_{xx} is independent of the laser power. This counterintuitive response arises from the fact that trapping (scattering of photons) also performs a position measurement of the levitated nanoparticle. Thus, although increasing the laser power n leads to a linear increase of backaction it also increases optical confinement maintaining S^b_{xx} fixed (see also Fig.3.4).

This last point can also be derived considering the mean-square displacement of an optically trapped particle whose thermal bath fluctuations scale with n, as well as its stiffness κ:

$$S^{SQL}_{xx} = \approx \frac{2(\hbar\omega)^2}{5\pi c^2}\frac{1}{\pi w_o^2 2k_b\Gamma}\frac{n}{\kappa_x} \tag{3.59}$$

Finally, adding the measurement uncertainties and the backaction we find the minimum fluctuations resolvable by the SQL

$$\langle \delta x^2_{SQL}\rangle = \langle \delta x^2_{sh}\rangle + \langle \delta x^2_b\rangle = \frac{1}{nM^2}\left(\frac{\pi^{3/2}\epsilon_o w_o^3}{4k\alpha}\right)^2 + \frac{\alpha k^4 w_o^2\hbar\omega}{60\pi c\Gamma m\epsilon_o} \tag{3.60}$$

Figure (3.4) shows the different contributions to position uncertainties as a function of n for a 1550 nm diffraction limited optical trap with 0.8NA. We see that a shot noise limited free space detection can resolve a quantum ground state in the trap with $n \sim 10^{14} - 10^{18}$, corresponding to 0.1μW-100 mW.

Considering our optical traps use about 100 mW of power, measuring x_{zpf} seems within reach. Still, this requires to achieve high enough values for $\Gamma \sim 10^3$, avoid optical losses and have detectors that can handle such high optical powers while staying shot noise limited.

Cavity Readout

We now turn our attention to the use of the optical cavity as readout mechanism. If we intoduce a dielectric nanoparticle in the cavity mode, it increases the overall optical path seen

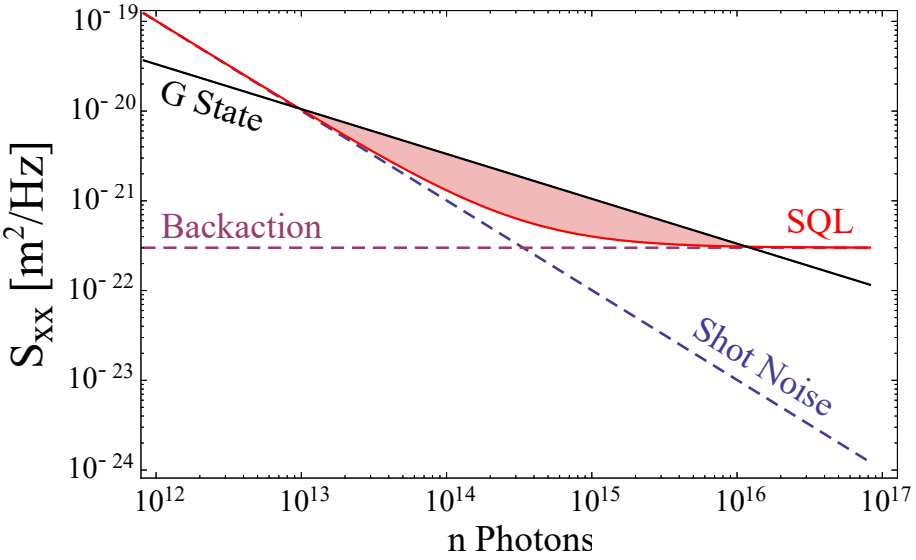

Figure 3.4: Interferometric detection limits using backfocal plane interferometry for a diffraction limit optical trap with NA=0.8, $\lambda = 1550nm$ and a spherical particle of 73nm radius. The blue dashed line shows the impression limit from shot noise whereas the purple curve represents the measurement backaction in the system considering a dissipation $\Gamma = 1000$. The sum of the two contributions is shown in red as the SQL. The black curve represents the zero point fluctuations x^2_{zpf}. The red shaded area between the black and red curve shows the region in which a thermal occupation below 1 phonon can be resolved using a BFP interferometric approach.

by the cavity field resulting in a shift of the cavity resonance frequency, which is known as dispersive coupling. For a dielectric particle in the dipole regime, this frequency shift is given by[25,101]:

$$\delta\omega_c(x) = \omega_c \frac{\alpha_p}{2V_m\epsilon_o} f(x) \tag{3.61}$$

where $V_m = \pi L(w_o/2)^2$ is the cavity mode volume, α_p the particle polarizability and $f(x) = \sin^2(kx)$ is the intensity profile normalised to 1. Expanding $\delta\omega_c$ around $kx = \pi/4$ we obtain a linear response:

$$\frac{\delta\Phi}{\tau} = \delta\omega_c(x) \approx \frac{\partial\omega_c}{\partial x}\delta x \approx \omega_c \frac{\alpha_p}{2V_m\epsilon_o} 2k\delta x = G\delta x \tag{3.62}$$

where G is the so-called optomechanical coupling strength and corresponds to the linear term of the frequency shift expansion. We use this expression to find how the particle phase fluctuations are imprinted in the transmitted cavity field (Eq.3.46):

$$\begin{aligned}\langle Sqq_{tr}\rangle &= \frac{(\gamma_o - T_1)^2 + \tau^2\Omega^2}{\gamma_o^2 + \tau^2\Omega^2} + \frac{T_1 P}{\gamma_o^2 + \tau^2\Omega^2} + \frac{4P\langle\bar{\alpha}^2\rangle}{\gamma_o^2 + \tau^2\Omega^2}(G\tau)^2\langle\delta x^2\rangle \\ &= 1 + \frac{TP}{(T+P)^2}\frac{n_{in}(16F)^2}{1+(\Omega/\Omega_c)^2}\frac{G^2\langle\delta x^2\rangle}{\Delta\omega_{FSR}^2} \end{aligned} \tag{3.63}$$

where we have considered both cavity input ports to be quantum limited ($\delta q_{in} = \delta q_{vac} = 1$).

Our sensitivity limit is reached when the particle induced phase fluctuations are equal to the quantum field fluctuation term (first term on the r.h.s of Eq. 3.63). Hence the smallest particle position fluctuations we can resolve are:

$$\langle\delta x^2\rangle_{sh} = \frac{(T+P)^2}{TP}\frac{1+(\Omega/\Omega_c)^2}{n_{in}(16F)^2G^2}\Delta\omega_{FSR}^2 \tag{3.64}$$

This equation shows that the sensitivity is reduced for high frequency fluctuations above Ω_c, similarly to what we saw for δp. The sensitivity also improves with the finesse F, the power driving the cavity n_{in} and the optomechanical coupling strength G; in other words all parameters increasing the light matter interaction. The terms T and P indicate how losses also reduce our sensitivity and how in the case of symmetric cavity phase fluctuations can be extracted through both cavity mirrors. Note that these phase fluctuations can only be read by beating the transmitted beam with a reference laser, therefore we will need to mix this signal with a properly mode matched reference beam.

Next we use Eq. (1.65) to rewrite the mechanical frequency Ω_m as a function of the number of photons n circulating in the cavity standing wave of the TEM_{00} mode:

$$\Omega_m = \sqrt{\frac{3k^2 n_{in}\hbar\omega F^2 T_1}{\rho c\pi^3 w_o^2}\frac{\epsilon-1}{\epsilon+2}} \tag{3.65}$$

And we estimate the backaction introduced by the trapping field as in the BFP case but

assuming that most of the photons are scattered along the cavity axis due to the higher density of states:

$$S_{xx}^{b} = \frac{n_{in}}{\Gamma(m\Omega_m)^2}\sigma\frac{(\hbar\omega_c F)^2 T_1}{\pi(c\pi w_o)^2} = \frac{\hbar\omega_c k^2\alpha}{6\pi\epsilon_o c\Gamma m} \tag{3.66}$$

Which also shows that backaction neither deppends on the particle size nor trapping power as in the BFP case. This is not surprising as we are still considering the scattering in an optical trap with minor geometrical differences.

Note however, that for this readout to work the particle needs to sit in the linear slope of the standing wave and not in the local maxima. As a result the particle wil not oscillate according to the potential used in Eq. (3.65) and we will need to provide an additional potential created by second cavity mode or an optical tweezer. For an additional cavity mode this analysis remains valid and we just need to add a factor $C \approx 3$ in the backaction to account for the extra power in the trapping beam; the case of an optical tweezer will be analysed afterwards.

Taking this into account and adding the shot noise contribution we find the SQL for an optical cavity trapping and detection scheme:

$$S_{xx}^{SQL} = \frac{(T+P)^2}{TP}\frac{1+(\Omega/\Omega_c)^2}{n_{in}(16F)^2G^2}\Delta\omega_{FSR}^2 + S\frac{\hbar\omega_c k^2\alpha}{6\pi\epsilon_o c\Gamma m} \tag{3.67}$$

Figure (3.5) shows the SQL limit for a particle trapped at the centre of a 2.5cm high finesse confocal optical cavity for $\lambda = 1064$ nm as a function of the photons impinging the cavity input mirror and assuming the same Γ as in the BFP and a shot noise limited reference beam. We see that we are able to detect fluctuations smaller than δx_{zpf} while using lower optical powers, meaning that our sensitivity increases due to the light-matter interaction enhancement provided by the cavity. We observe also larger zero-point fluctuations δx_{zpf}^2, due also to the smaller intensity in the trap focus.

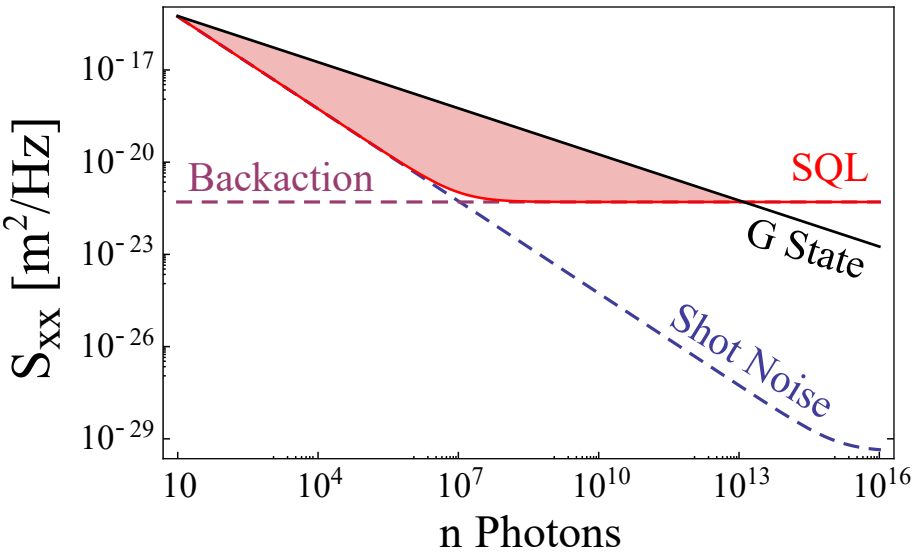

Figure 3.5: Interferometric detection limits using a lossless confocal optical cavity of 2.5 cm length and $F = 700.000$ for $\lambda = 1064nm$. The cavity has waist w_o is $65\mu m$ and a silica nanoparticle of 75nm radius is placed at the centre. The blue dashed curve represents the measurement imprecision caused by shot noise whereas the purple line shows the measurement backaction in the system for a value of $\Gamma = 1000$. The red curve shows their addition as the SQL. In black we show the zero-point fluctuations x^2_{zpf}. The red shaded area between the black and red curve shows the region in which a thermal occupation below 1 phonon can be resolved using a cavity readout approach.

Discussion

In this section we have presented a model for two different interferometric detection techniques. A priori both can resolve the zero point fluctuations of a trapped particle GS. However, from the practical point of view some of the requirements can hardly be satisfied. For example, the cavity detection approach neglects the presence of additional intracavity fluctuations such as thermal noise in the mirrors. These are totally non-negligible as the mirror optomechanical coupling strength ($G_m = \omega_{cav}/L \approx 10^{17}$) is 10 orders of magnitude larger than the one of the particle. Therefore we can foresee that thermal noise in the mirrors may dominate the spectra of transmitted fluctuations specially at frequencies < 1 MHz. This problem is non-existent for the BFP detection, where the beam carrying the signal only interacts with the particle and the reference beam. This statement is supported by the literature where experiments in references[37,62] implement optical-cavity readouts and show significantly worse SNR than experiments in references[54,67,45] where BFP detection is implemented.

Alternatively we can also improve our sensitivity by boosting the optomechanical coupling strength G either by miniaturising the optical cavity or using larger particles as S^b_{xx} does not depend on the particle size. On the one hand larger particles result into smaller x_{zpf} and more interactions with the residual air molecules making it harder to reach GS. Cavity miniaturization on the other hand is a good approach but leads to larger optical linewidths and would limit the cooling rate Γ.
Finally, both detection techniques have to deal with the presence of classical noise in a strong reference beam of the interferometer, which can be minimised using a noise eater and balancing well the detectors.

Another experimental constraint is the fact that current optical levitation setups require to break vacuum and load a particle at ambient pressure. This means that optical potential ($U_{opt} \propto \Omega_m^2$) needs to be deep enough to confine the particle against thermal fluctuations at atmospheric pressure. This can be a strong inconvenience when using a cavity since confinement transverse to the optical axis is weaker.

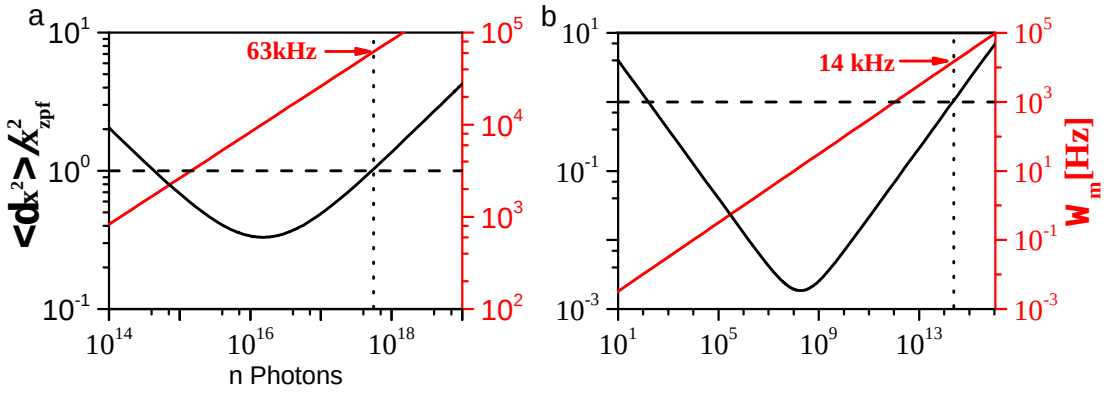

Figure 3.6: Ratio between standard quantum limit and ground state fluctuations vs. the photons in the optical trap (a) and photons impinging the cavity (b). The dashed line corresponds to a SNR=1. The dot line is a guide to the eye showing which is the maximum frequency we of our mechanical oscillator at the point where backaction overcomes x_{zpf}. Again we have assumed an external dissipation $\Gamma = 1000$.

Figure (3.6) shows the mechanical frequency and the ratio of the SQL and x_{zpf} as a function n in the optical tweezer and n_{in} for the cavity for the optical powers considered. We see that despite the cavity achieves a higher sensitivity than the BFP interferometry, a single beam optical trap achieves higher mechanical frequencies (i.e. deeper optical potential in the ground state detectability range) thus better confinement along all 3 axis.

Considering all these points, the best option to measure the ground state of a mechanical oscillator seems to be the use of a BFP detection scheme. Also since we will work in the backaction dominated regime we will try to use larger wavelengths (i.e. $\lambda = 1550$ nm) to minimise $Sxxb$ while still working with detectors (InGaAs) offering high quantum efficiencies (≈ 0.8).

Optical Damping

In our calculations we have assumed the existence of a mechanical dissipation channel with $\Gamma = 1$ kHz but we have not discussed its origin or how to achieve it. We will now discuss about two possible optical techniques to provide this mechanical dissipation to our mechan-

ical oscillator. The first scheme consists on a direct modulation of the optical potential based on the measured position of the levitated nanoparticle, the second relies on the passive cavity delayed response when the mechanical frequency of the oscillator is lower than the cavity bandwidth.

Active Feedback Cooling

The simplest approach consists on implementing an active feedback based on the particle's position that modulates the optical potential in order to extract energy from its centre of mass.
In the second chapter isothermal expansions/compressions of the optical potential have been used to extract/increase the energy from the centre of mass degree of freedom. For a periodic motion the feedback needs to run cyclically and we need to time correctly the trap expansions and compressions with the oscillatory motion to maximise the dissipation Γ, thus building a thermodynamic cycle[†]. Due to the unprecedented thermal isolation of the particle from the environment fast thermalization is strongly suppressed and we achieve a steady state where $T_{CM} \ll T_{bath}$.

The design of a simple dissipative cycle shown in Fig.(3.7). It consists on four instantaneous trap modulations during an oscillation period. The trap power is lowered at the extremes of the motion and increased back when the particle is at the trap center. The work on the system performed in this instantaneous processes is:

$$\delta W = \frac{\partial U}{\partial \kappa_x} \delta \kappa_x = x^2 \delta \kappa \tag{3.68}$$

This equation shows that when compressions are performed at $x = 0$ the work put on the system is minimized ($\delta W = 0$), whereas performing the expansions at the maximum value of x^2 maximizes the extracted work.

To estimate the optical cooling rate Γ_{opt} we consider that the energy of the particle at

[†] A macroscopic analog of this process would be the compressor in a fridge that compresses and expands a gas that extracts heat from the food compartment

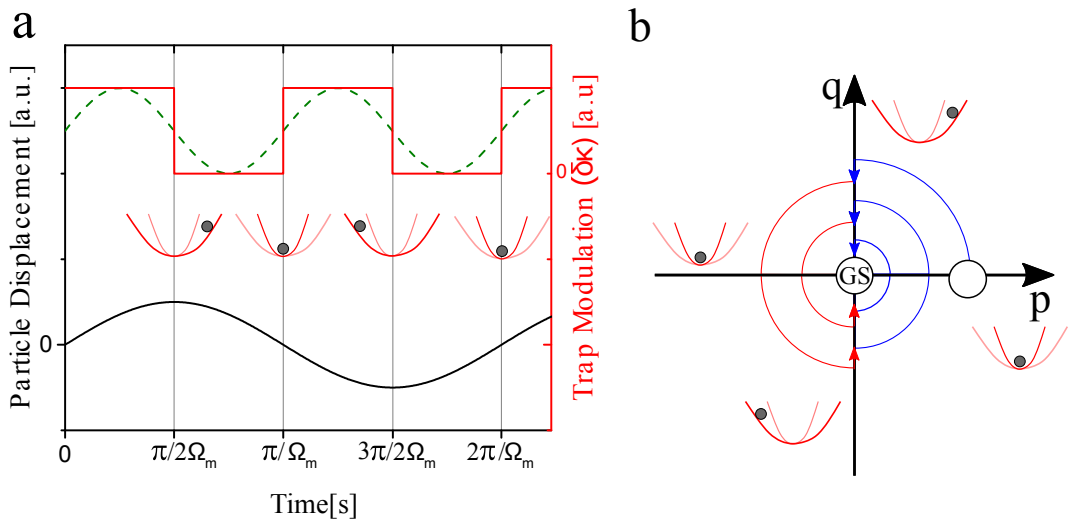

Figure 3.7: (a)Scheme of a thermodynamic cycle to cool the centre of mass motion by doing instantaneous isothermal expansions and compressions. The red square signal shows the stiffness modulation during one period of the particle motion (solid black line). The illustrarions show the qualitative change of the potential according to the particle position. We also show an harmonic approximation to the square signal (green dashed line). (b) Shows how the cooling affects the particle motion in the quadrature representation.

time $t = \pi/(2\Omega_m)$ is at equilibrium with the thermal bath $E = \kappa x_{max}^2 = 2k_bT$. Then the energy dissipated in a single expansion becomes:

$$\frac{dE}{dt} \approx \frac{\delta W}{\delta t} = x_{max}^2 \delta\kappa_x 2\Omega_m \tag{3.69}$$

For a small enough modulation $\delta\kappa_x \ll \kappa_x$ the period of the oscillations will remains unchanged. Averaging the energy dissipated in half period we find the total energy dissipation rate $\Gamma_o pt$ provided by the feedback:

$$\Gamma_{opt} = 4\Omega_m \frac{\delta\kappa_x}{\kappa_x} \tag{3.70}$$

To find the centre of mass temperature of the steady state we need to account for the heat exchanged with the bath. For an underdamped harmonic oscillator this leads to[112]:

$$\delta Q = \kappa x \delta x + \frac{p}{m}\delta p + \frac{1}{2m}\delta p^2 \tag{3.71}$$

where

$$dx = \frac{p}{m}dt, \qquad dp = (-\kappa x - \Gamma_m)dt + \sqrt{2m\Gamma_m k_b T}dW(t) \tag{3.72}$$

and $W(t)$ is a Wiener process ($\langle dW(t)\rangle = 0$ and $\langle dW(t)^2\rangle = dt$).

Substituting δq and δp in Eq.(3.71) we find the expression for the heat differential:

$$dQ = \Gamma(k_b T - \frac{p^2}{m})dt + \frac{p}{m}\sqrt{2m\Gamma_m k_b T}dW(t) \tag{3.73}$$

maintaining the assumption that the energy change over one cycle is small and averaging dQ over a period yields:

$$\langle p^2/m\rangle = E \tag{3.74}$$

$$dW(t) = 0 \tag{3.75}$$

$$\langle dQ\rangle = \Gamma_m(k_b T - E)dt \tag{3.76}$$

Finally adding the contribution from work (Eq. 3.70) and using the 2^{nd} law of thermodynamics leads to the average energy change in the system :

$$\langle dE\rangle = \left(\Gamma_m k_b T - \langle E\rangle\Gamma_m - 4\frac{\delta\kappa_x}{\kappa_x})\right)dt \tag{3.77}$$

which results in a steady state energy for the center of mass

$$E_{CM} = \frac{k_b T\Gamma_m}{\Gamma_m + \Gamma_{opt}} \tag{3.78}$$

This defines a new dissipation $\Gamma = \Gamma_m + \Gamma_{opt}$ and a centre of mass temperature T_{CM}:

$$T_{CM} = T\frac{\Gamma_m}{\Gamma_m + \Gamma_{opt}} \tag{3.79}$$

For a the mechanical frequency $\Omega_m = 63kHz$ for which ground state can be resolved (Fig.3.6) and a trap modulation of 0.5% we obtain $\Gamma \approx 1250$ at 10^{-8} mbar, which is larger than the value considered in the ground state calculations. Experimentally though, this feedback scheme has never been implemented in a single beam optical trapping experiment. Instead, the single beam optical trap cooling schemes use a sinusoidal modulation corresponding to the the first term of the Fourier expansion of the square signal (Fig. (3.7)[54,44]. The reason is that it is more accessible to work with pure harmonic components, although the continuous trap modulation introduces unwanted reheating during the cycle.

So far we have considered a single axis, but in an actual experiment cooling is perform along $x, y,$ and z axis, requiring 3 modulation cycles. Since the motion along the different axis is decoupled, modulation to cool a given axis will be out of phase respect to the remaining ones. This results into additional work put into the system which reduces the cooling efficiency when compared to the single axis calculations.

Cavity cooling

The second approach to dissipate mechanical energy using optical fields consists on using an cavity whose linewidth is smaller than the mechanical frequency. Contrary to the feedback case, this approach does not need prior knowledge of the particle position.
Here we will present a semiclassical derivation of the system's equations of motion based on refference[8]. For an extensive derivation in the quantum picture see the same reference[8].

We start by considering the configuration of an optically trapped nanoparticle at the linear slope of a cavity standing wave ($Kx = \pi/4$) with power P. The additional gradient force

along x introduced by the of the cavity writes:

$$F_x = \frac{1}{4} Re[\alpha] \nabla E_o^2 = \frac{\alpha 4\mathrm{P}}{2c\epsilon_o w_o^2 \pi} \nabla \sin^2(kx) \approx \hbar G n_{cav} \tag{3.80}$$

where the force term is linearised assuming that the particle fluctuates in the Lamb-Dicke regime ($k\sqrt{\langle x^2 \rangle} \ll 1$). This leads a to an extra force term $\hbar G n_{cav}$ entering the particle equation of motion. Adding the cavity equation of motion (Eq. 3.32) the trap-cavity system is described by the coupled equations:

$$\begin{aligned} m\ddot{x} &= -m\Gamma_m \dot{x} - m\Omega_m^2 x + \hbar G n_{cav} & (3.81) \\ \dot{\alpha} &= -\frac{\kappa}{2}\alpha + i(\Delta + Gx)\alpha + \sqrt{\kappa_1}\alpha_{in} & (3.82) \end{aligned}$$

Note that we have rewritten Eq.3.32 with the following substitutions $\alpha_c = \sqrt{\tau}\alpha$ as the amplitude of the cavity standing mode, $\Delta = \Phi/\tau$ as cavity detuning and $\kappa_1 = T_1/(2\tau)$ as the coupling rate of the input mirror.

As a first step to solve the coupled equation of motion we linearise them around the steady state of the cavity field:

$$\begin{aligned} m\ddot{x} &= -m\Omega_m^2 x - m\Gamma_m \dot{x} + \hbar G(\bar{\alpha}_c^* \delta\alpha_c + \bar{\alpha}_c \delta\alpha_c^*) & (3.83) \\ \delta\dot{a} &= (i\Delta - \frac{\kappa}{2})\delta\alpha_c + iGx\bar{\alpha}_c & (3.84) \end{aligned}$$

and then we Fourier transform them, to obtain the following equations in the frequency space writes as:

$$\begin{aligned} -m\Omega^2 x[\Omega] &= -m\Omega_m^2 x[\Omega] + im\Gamma_m \Omega x[\Omega] + hG(\bar{\alpha}_c^* \delta\alpha_c[\Omega] + \bar{\alpha}_c \delta\alpha_c^*[\Omega]) & (3.85) \\ -i\Omega\delta\alpha_c[\Omega] &= (i\Delta - \frac{\kappa}{2})\delta\alpha_c[\Omega] + iG\bar{\alpha}_c x[\Omega] & (3.86) \end{aligned}$$

Substituting the second expression into the first gives susceptibility of the mechanical oscillator:

$$\chi[\Omega] = \left(-m\Omega^2 + m\Omega_m^2 - i\Omega\Gamma_m + \hbar G^2|\bar{\alpha}_c|^2\left(\frac{1}{(\Delta+\Omega)+i\kappa/2} - \frac{1}{(\Delta-\Omega)-i\kappa/2}\right)\right)^{-1} \tag{3.87}$$

Finally rearranging into real and imaginary terms and substituting $\hbar G^2|\bar{\alpha}|^2 = 2m\Omega_m g^2$ yields

$$\chi^{-1} = m\left(\Omega_m^2 + 2\omega\delta\Omega_m(\Omega) - \Omega^2 - i\omega[\Gamma_m + \Gamma_{opt}(\Omega)]\right) \tag{3.88}$$

where

$$\delta\Omega_m[\Omega] = g^2\frac{\Omega_m}{\omega}\left(\frac{\Delta+\Omega}{(\Delta+\Omega)^2+\kappa^2/4} + \frac{(\Delta-\omega)^2}{(\Delta-\Omega)^2+\kappa^2/4}\right) \tag{3.89}$$

is an optomechanically induced mechanical frequency shift and

$$\Gamma_{opt} = g^2\frac{\Omega_m}{\omega}\left(\frac{\kappa}{(\Delta+\omega)^2+\kappa^2/4} - \frac{\kappa}{(\Delta-\omega)^2+\kappa^2/4}\right) \tag{3.90}$$

is the additional mechanical dissipation introduced by the cavity.

Equation (3.89) tells us that for a red-shift detuning ($\omega_l < \omega_c$) the mechanical frequency decreases while the opposite occurs in the blue detuned regime ($\omega_l > \omega_c$). Similarly Eq.(3.90) shows that the dissipation on the mechanical oscillator increases when working in the red-detuned regime while fluctuations are amplified in the blue detuned regime. Furthermore, Γ is maximised by reducing the cavity losses κ. This sets two different cooling regimes: the resolved-sideband regime when $\Omega_m > \kappa$ and the Doppler regime when $\kappa > \Omega_m$.

In the resolved sideband-regime, the lowest temperature is achieved for a detuning equal to the mechanical frequency ($\Delta = -\Omega_m$) yielding:

$$\Gamma_{opt} \approx 4\frac{g^2}{\kappa} \tag{3.91}$$

Similarly in the Doppler regime the lowest temperature is achieved for a detuning equal to

the cavity linewidth $\Delta = \kappa/2$ which yields :

$$\Gamma_{opt} \approx 8 \left(\frac{g}{\kappa}\right)^2 \Omega_m \tag{3.92}$$

Thus to achieve higher dissipations (lower temperatures) we need a cavity in the resolved sideband regime where Γ increases with κ^{-1}, instead of κ^{-2} as is the Doppler regime case.

Discussion

We have presented two different cooling schemes: an active feedback where the trap power is actively modulated to cool down the motion along three axes and a passive feedback where a detuned optical cavity cools down particle motion one axis. Current state of the art experiments have achieved cooling rates $\Gamma_{opt} = 2\pi \cdot 270$Hz for 100 nm particles using active feedback[54] and $\Gamma_{opt} = 2\pi \cdot 49$ kHz for 240 nm particle (that would be around $2\pi \cdot 720$Hz for 100 nm particles) using cavity cooling[62]. These have allowed to cool the centre of mass down to $T_{CM} \approx 450\mu$ K in an optical tweezer[54] and $T_{CM} \approx 64$ K in a high Finesse cavity[62]. The reason of this large difference in T_{CM} is that cavity experiments could only be performed at pressures up to few mbar where thermalization due to air molecules was still high. This limitation was caused by the particle loss due to the lack of cooling along the other axis. Conversely, active feedback experiments could reach $2 \cdot 10^{-8}$mbar where interactions with gas are negligible and most reheating comes from backaction and feedback itself due to uncertainties in the measurement. This means that if particles can be brought to the same vacuum conditions while using a cavity, they could be cooled to the ground state.
Therefore, our approach will be to combine the best of the two approaches: the sensitive detection and 3 axis cooling of an optical tweezer and the high cooling rate of a cavity in the resolved sideband regime. This will allow us to actively cool the centre of mass in all directions and then use the passive cavity cooling to beat the limitations of the active feedback along a single axis. Note that the use of a tweezer also provides a mean to confine the optically levitated nanoparticle in the linear slope of the cavity standing wave.

With this scheme the particle particle will interact with two optical fields so the backac-

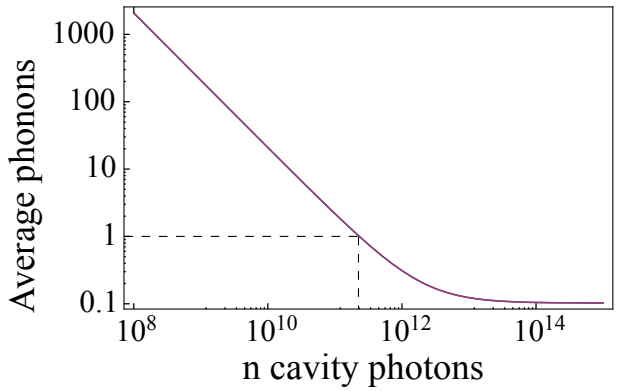

Figure 3.8: Average phonon occupation number for a 73 nm radius nanoparticle levitated in an optical tweezer using $\lambda_{tw} = 1550nm$ and cooled by a 1064 nm cavity with $F = 700.000$ and $L = 2.5$cm. The mechanical frequency is assumed to be $\Omega_x = 2\pi \cdot 100$ kHz

tion introduced by each of them needs to be accounted in the calculations, as well as the fact that Γ_{opt} now depends on the optical cavity field. Different wavelengths will also be used for each field to avoid artefacts in the interferometric measurements. On the one hand, the optical tweezer will be the main contribution to backaction ($\propto \lambda^{-4}$) so a longer wavelength $\lambda_{tw} = 1550$nm will be used to minimise it. On the other hand the cavity field will be weaker, thus a shorter wavelength $\lambda_{cav} \approx 1064$ nm will be chosen to increase the optomechanical interaction while still being a minor contributor to backaction.

To determine the intensity needed in each field we start by fixing an optical tweezer power P≈ 175mW that resolves x_{zpf} well above the shot noise limit (Fig.3.4) and gives a mechanical frequency $\Omega_m \approx 100$ kHz along is transverse axis. Then we find the intracavity power needed for Γ_{opt} to cool system to ground state against the optical tweezer and cavity fields backaction $S_{xx}^{b1550} + S_{xx}^{b1064}\rangle$ below x_{zpf}^2.

Figure (3.8) shows $(S_{xx}^{b1550} + S_{xx}^{b1064})/x_{zpf}^2$ as a function the intracavity photon number n in a $F \approx 700.000$ and 2.5cm long cavity. For $n > 4 \cdot 10^{10}$ we are able to reach a mechanical occupation number below 1, which corresponds to the ground state. Then estimating how much detuned power we need at the coupling mirror we find:

$$P \approx \frac{n\hbar\omega_c(\Omega_m^2 + (\kappa/2)^2)}{\kappa} \approx 48mW \tag{3.93}$$

In conclusion from the theoretical point of view it is feasible to couple an optical tweezer to an optical cavity and harness the advantages of both configurations: the high stability and sensitivity from the tweezer and the high optical cooling rates of a cavity. This should allow to reach and resolve the quantum ground-state of an optically levitated nanoparticle at room temperature.

Experimental Results

In this section we present the details of the experimental setup that built to levitate, measure and cool a nanoparticle to its motional ground state. Then we will benchmark its capabilities and show the first experiments demonstrating cavity cooling of a levitated nanoparticle in an external optical tweezer.

Setup Overview

Our theoretical calculations have established the following experimental requirements in order to achieve ground state cooling of a levitated nanoparticle at room temperature:

- We need to be able to bring a levitated nanoparticle to pressures around 10^{-8} mbar to avoid unwanted interactions with the environment.
- We need a high finesse cavity in the resolved sideband and the ability to couple it to an optically trapped particle in order perform resolved sideband cooling.
- The optical trap needs also to be able to resolve the zero point fluctuations of the ground state.

- We need to correct for all imperfections that take place in a real experiment and have not been taken into account in our calculations (laser noise above shot noise, electric noise, optical losses...).

Taking these into account we have built the high vacuum setup depicted in Fig.3.9

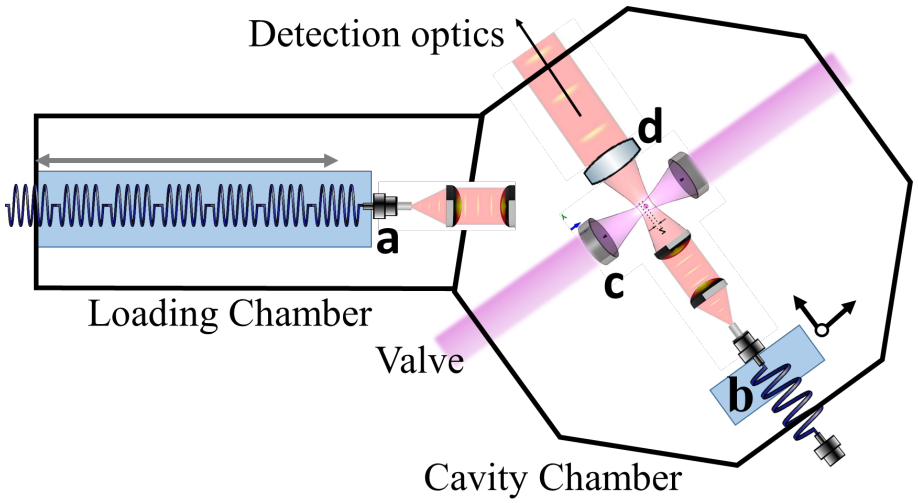

Figure 3.9: Main elements of the vacuum setup. The loading chamber and the cavity chamber are separated by an all metal vacuum valve.The loading chamber contains a translation stage (a) that translates the mobile optical trap to the cavity chamber. In the cavity chamber we have a 3D piezo stage with a second mobile optical trap that can position optically trapped particles in the cavity field. The forward scattered light is collected with a high NA lens (d) and send to the position detection system.

The setup is built around the idea of protecting the cavity mirrors from dirt every time particles are loaded to the optical trap. It consists of two separate vacuum chambers in a load-lock configuration. The first vacuum chamber (Fig.3.9 Loading Chamber) is used to load a particle in a mobile optical trap (MobOT) (Fig.3.9a) at ambient pressure using a nebuliser with a suspension of silica particles and ethanol. Then, we decrease the loading chamber pressure to 1 mbar and bring the particle to the second vacuum chamber (Fig.3.9 Cavity Chamber) where it is transferred to a second optical trap mounted on a 3D piezo stage inside the optical cavity holder (Fig.3.9b). This second trap is aligned with a highly sensitive BFP detection system (Fig.3.9d) with the goal to resolve the quantum ground state. Once the particle

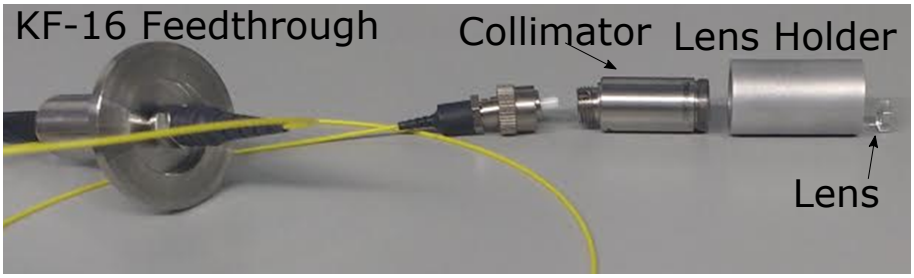

Figure 3.10: Main elements inside the MobOT. The fibre is sent to vacuum through a fibre feedthrough, followed by a collimator, a lens holder and the high NA lens.

transferred, the loading trap is retracted and we close the valve separating the two vacuum chambers. Then we couple the Cavity MobOT to the High Finesse Cavity standing wave (Fig.3.9c), and we start to evacuate the second vacuum chamber while the particle is feedback stabilized in the optical tweezer. In case the cavity unlocks, there is no risk of loosing the particle and it can be locked on and off with different fields when needed for a given optomechanical experiment. The load-lock scheme also makes it easier to reach UHV pressures in the cavity chamber.

In the following subsections we give an accurate description and performance benchmark of the different elements in our setup.

Mobile Optical Trap

To be able to manipulate levitated particles in vacuum over arbitrarily long distances we have designed a new kind of optical trap called mobile optical trap (MobOT). The trap consists of a single mode optical fiber and a collimator followed by a high NA aspheric lens. Figure (3.10) shows an unassembled MobOT system, which weight less than 100g, making it compatible nano-positioning systems such as stick-slip piezos.

Although we have designed the MobOT to displace the optical trap it can also be fixed. Compared to the conventional approach that uses a collimated beam and an objective, our approach allows to fully fiberize the trapping beam simplifying the alignment, reducing point-

ing noise, absorption and reflections of the objective focusing optics and the overall cost of the experiment. The smaller size of the MobOT elements also results in lower outgassing rates, making them compatible with HV experiments.

In our experiment we have implemented two different Mobots. In the current configuration, the first Mobot (loading) is mounted on a large cylindrical rod in the loading chamber. To bring the light into a fibre in the vacuum chamber we use a KF-16 single mode fibre feedthrough from Schäfter Kirchhoff. After the fibre we use a collimator that gives a 4.8mm beam diameter output followed by a 5.3 mm diameter NA lens (0.77NA) that focuses the beam to a diffraction limited spot. This trap has been used with wavelengths of 980 nm, 1064 nm and 1550 nm. The particle signal is monitored in backreflection using a photodiode (Fig. 3.11a).

The second MobOT rests in the cavity chamber. It uses the same optical fiber feedthrough and a collimation lens that gives a 2mm diameter output beam, which is then focused with a 1.28mm diameter 0.8 NA lens. The intensity at the trap focus is modulated with an AOM. This trap is mounted on a 3D stick-slip piezo positioning system[‡] next to the high finesse optical cavity. Figure (3.11) shows a scheme of the different elements of the cavity MobOT. In front of the trap we set a BFP detection system with a 0.77NA collection lens that sends the forward scattered light to three balanced detectors [§]. We use a D-shape mirror to choose the axis projected in the X and Y photodetectors and the full beam for Z, which is balanced using the same laser picked prior to fibre feedthrough coupling. Finally a $\lambda/4$ and $\lambda/2$ waveplates are used to align the trap polarization orthogonal to the cavity axis.

The laser source for the cavity trap is a low noise narrow linewidth 2W fiber laser with $\lambda = 1550$ nm [¶], allowing us to create an optical trap in the frequency ranges of $\Omega_z \in [10kHz, 50kHz]$, $\Omega_x, \Omega_y \in [30kHz, 180kHz]$, which covers the mechanical frequencies

[‡] SMARACT
[§] New Focus 2117
[¶] CF-Kilo, Keopsys

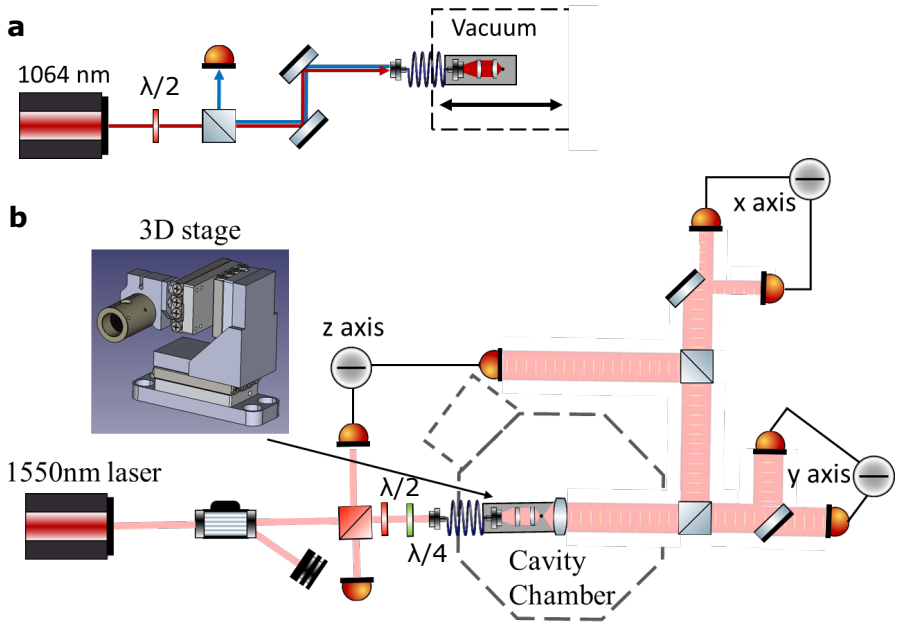

Figure 3.11: Detailed scheme of the MobOT. (a) The long range MobOT is mounted in an infinite screw to perform a load-lock transfer between the two vacuum chambers . Using a PBS the back-reflected signal is sent to a photodiode. (b) The cavity MobOT rests on a 3D positioning piezo-stage. The trap intensity is modulated using an AOM and its polarization is aligned to the cavity axis using a $\lambda/4$ and $\lambda/2$ wavepletes. A high NA lens collects the forward scattered field that is slitted into three balanced detectors measuring the particle displacement along each axis.

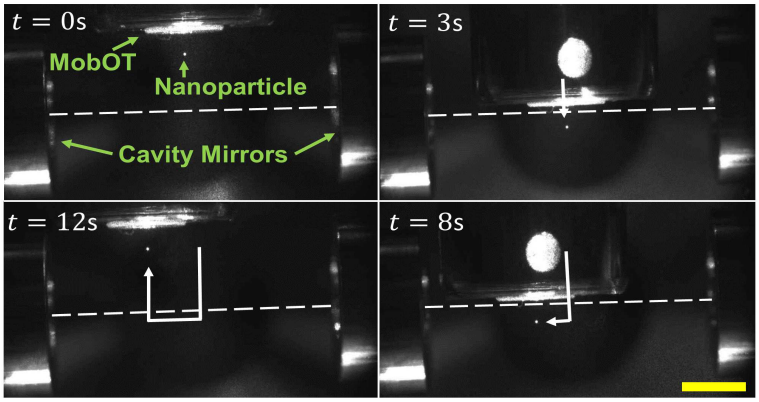

Figure 3.12: 3D displacements of a levitated nanoparticle through a high finesse optical cavity. The white dashed line shows the cavity axis and the solid white line follows the trajectory of the particle. The time at which each picture is taken is shown on the top left corner. The yellow scale bar corresponds to a length of 5 mm.

estimated in our calculations for ground-state.

Two important features of our MobOT are the high degree of control in the position and depth of the trap. These allow to stably manipulate particles over arbitrarily long distances at speeds above $1c$m/s as shown in Fig.(3.12), where a particle is manipulated across our optical cavity using the loading MobOT. As already mentioned, mobile traps also permit to optically transfer levitated particles between different optical potentials in vacuum as shown in Fig.(3.13a). In this configuration we can transfer a nanoparticle from the loading MobOT to the standing wave of our resonant cavity (Fig.3.13b) or to the cavity MobOT. Note that this requires matching the focus position of the two traps with an accuracy of λ.

Optical Detection

Even for arbitrarily long displacements, the MobOT generates a signal of the relative particle position along the optical axis. This signal is generated from the backscattered field (E_p) collected with the same aspheric lens used for focusing. The signal is sent to a photodiode where it interferes with the field reflected at the end facet of the fiber E_r that acts as a reference arm

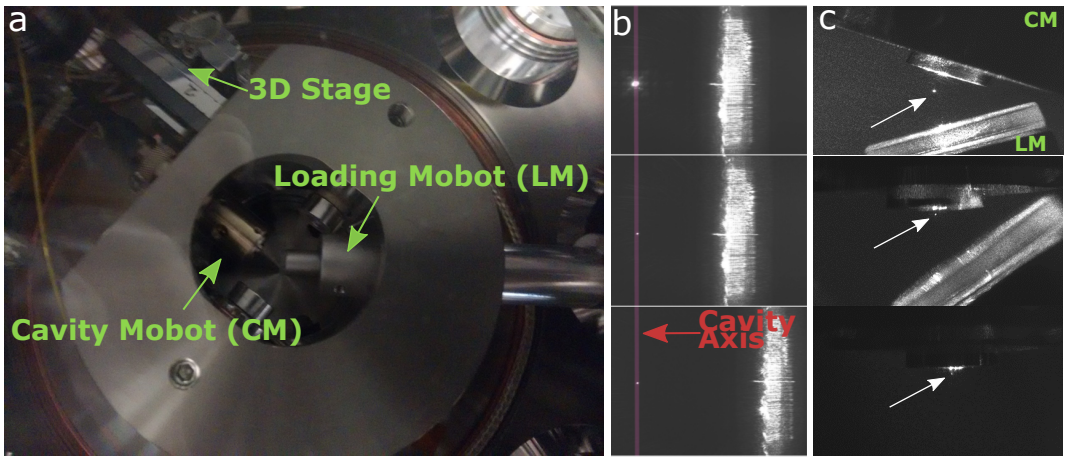

Figure 3.13: Optical transfer of a levitated nanoparticle between different optical fields. (a) Top view of the loading and cavity MobOTs inside the cavity holder. (b)Step by step optical transfer from the cavity MobOT to the standing wave of the cavity field: first the optically trapped particle is brought at the location of the standing wave (top), then the intracavity power is increased while the MobOT power is lowered until the particle jumps to the cavity standing wave (centre) and finally the MobOT is retracted (bottom). (c) Step by step optical transfer between to MobOTs: The particle is brought with the loading MobOT to the Focus of the Cavity MobOT, then power of the loading MobOT is decreased while the power on the Cavity MobOT increases until the particle is trapped in the later and finally the loading trap is retracted. We have used 1064 nm wavelength for the Loading MobOT and the cavity and 980 nm for the cavity MobOT.

in a homodyne detection scheme. The resulting intensity at the PD is given by[81]:

$$E_{PD}^2 = E_r^2 + E_p^2 + 2E_pE_r\cos(\phi_r + \phi_p(z)), \tag{3.94}$$

where ϕ_p and ϕ_r are the relative phases of the backscattered light from the particle and reference respectively.

The dipole radiation pattern of the particle imprints the position of the particle along the optical axis onto the phase of the backscattered light $\phi_p(z) \approx \phi_0 + \phi_z$. Here, $\phi_0 = \phi_r(0) - \phi_p$ is an arbitrary relative phase between the backscattered light from the particle and the reference beam and $\phi_z = 2k_0z$ is the phase change due to motion along the optical axis, where $k_0 = 2\pi/\lambda$ is the wavevector. Note that a small displacement of $z(t)$ along the optical axis leads to an optical path difference between the backscattered light and the reference $2z(t)$. For a periodic motion $z(t) = q_z\cos(\Omega_z t)$ the last term of Eq. (3.94) reads

$$2E_pE_r\left(J_0(2k_oq_z) + \mathrm{Re}\left\{2\sum_{n=1}^{\infty}e^{i\phi_0}i^nJ_n(2k_0q_z)\cos(n\Omega_z t)\right\}\right), \tag{3.95}$$

where we used the Jacobi-Anger expansion[1].

The right term of Eq. (3.95) is a sum of harmonics of the oscillation frequency of the particle where the relative strength of each harmonic is given by a Bessel function $J_n(2k_0q_z)$.

Figure (3.14) shows a characteristic time trace and FFT of the detector signal measured with a 73 nm radius nanoparticle trapped at 5mBar with a 0.8NA diffraction limited optical trap with $\lambda = 1064$ nm. The large SNR of the MobOT signal ($\approx$ 60 dBm) allows us to resolve the oscillatory underdamped motion of the particle and up to five harmonics of the oscillations along the optical axis $\Omega_z = 56$kHz. From the ratio of the 1^{st} and 3^{rd} harmonics $J_1(2k_0q_z)^2/J_3(2k_0q_z)^2$ we retrieve $q_z \approx 183$nm in excellent agreement with the 191 nm expected from the equipartition theorem $2T_0k_B = m\Omega_z^2q_z^2$, where $T_0 = 300$K and k_B is Boltzmann's constant, $m = 3.6\cdot10^{-18}$. Finally the FFT also features with a low SNR the second harmonic of the transverse axis oscillations $2\Omega_x$ and $2\Omega_y$, the later of which overlaps

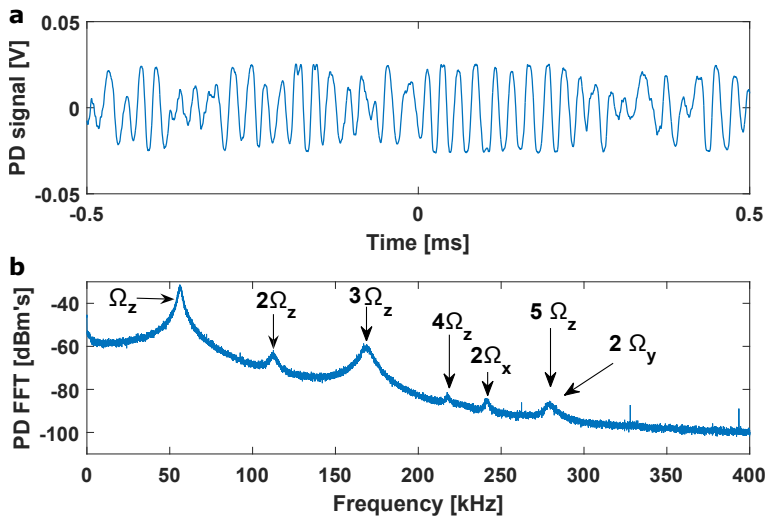

Figure 3.14: Trapping of a single 73nm radius silica nanoparticle in a mobile optical trap. (a) Time-trace of the backscattered intensity reaching the photodiode and (b) its average FFT using 64 windows of 0.1s at 4MHz acquisition frequency.

with the 5^{th} harmonic of Ω_z.

Conversely, for the cavity Mobile optical trap we use the BFP interferometry scheme that provides very high sensitivity along all axis. Figure (3.15) shows the PSD of each balanced photodiode for the same nanoparticle trapped in the cavity trap with more than 55dB SNR. Still, we see that the PSD corresponding to a ground state sits 16dB's below the background level which currently makes direct ground state measurement impossible. To overcome this limitation we have came up with two strategies. First maximising the BFP signal with high power balanced detectors that can handle up to 100 mW on each diode. Furthermore a laser intensity noise eater can lower background noise by approximately 30 dBm. Both allows for a gain in resolution of $>$ 16 dBm and will soon be implemented in the setup. Alternatively, we could also implement a ring-up measurement protocol similar to reference[54] in which the cavity cooling is switched off and from the reheating time trace we infer the initial phonon occupation number.

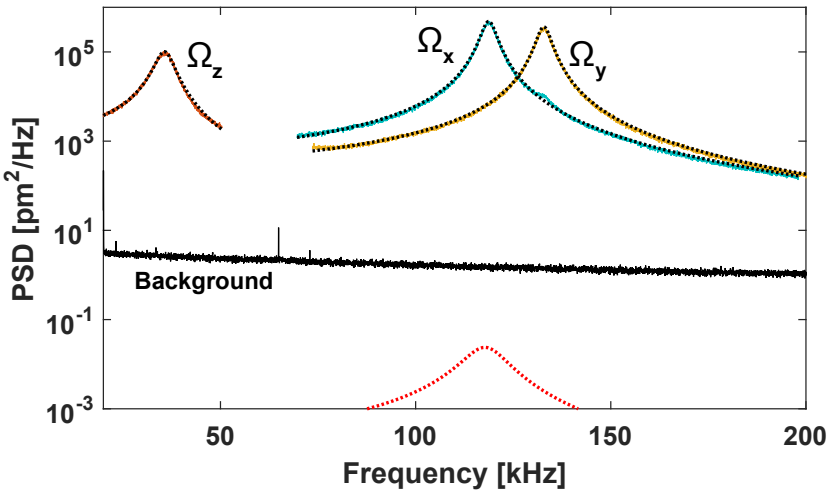

Figure 3.15: Power spectral densitiy of the particle motion in the mobile MobOT siting on the 3D piezo stage along the z axis (red solid line), x axis (cyan solid line) and y axis (yellow solid line). The black dashed line corresponds to lorentzian fits and the red dashed line to an Lorentzian signal that would correspond to the ground state along the x axis. The black solid line corresponds to the detector signal for the x axis for a trap without particle.

Noise Eater

Even low noise high power lasers feature intensity noise well above shot noise for frequencies <1 MHz. This reduces our sensitivity and also causes reheating of our particle centre of mass. To lower the classical noise in laser systems one can follow several methods such as using a large filtering cavity with narrow linewidth or a noise eater. The requirement of hundreds of mW for our optical traps makes the lock and stability of a filtering cavity challenging, thus we use as noise eater. A noise eater works by sending part of the laser power output to a photodiode. The photodiode fluctuations around the mean value are then fed as an error signal into a PID servo whose output is lowpass filtered and sent to an AOM modulating the laser power (see inset in Fig. 3.16). This noise eater reduces the impact of laser intensity noise by more than 30dB in the frequency range of interest as shown in Fig.(3.16).

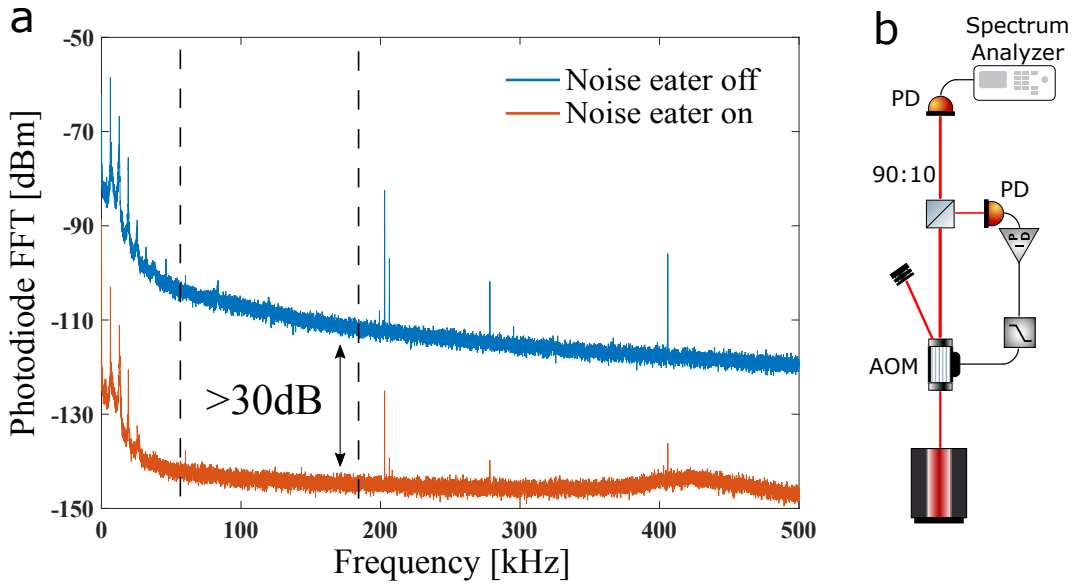

Figure 3.16: Noise eater performance. (a) FFT of the laser intensity fluctuations at the transmission photodiode without noise eater (blue) and with noise eater (red). The dashed lines mark the range of accessible mechanical frequencies Ω_x for our levitated nanoparticle. (b) shows the elements used to implement the noise eater in our setup.

Feedback Stabilization

Using the MobOT backscattered signal (Fig.3.14) it is also possible to generate a feedback signal to reduce the particle centre of mass motion. However, since oscillations along the transverse axis are poorly resolved by using a single mode optical fibre, these feedback mostly dissipates energy along the optical axis. Yet it improves the trap stability allowing to work for few hours at pressures below 0.01 mbar

The feedback scheme is implemented in a FPGA card that modulates the trap intensity of our loading MobOT. The feedback samples the particle position at 520 kHz (limited by the FPGA acquisition frequency). For each sample V_i we measure its deviation from the current mean $\langle V_z \rangle = M^{-1} \sum_{i-M}^{i-1} V_i$ and compare it to the standard deviation $\sigma_V = \sqrt{M^{-1} \sum_{i-M}^{i-1} (\langle V_z \rangle - V_i)^2}$ over the last $M = 13$ samples corresponding to an oscillation period. To cool the particle,

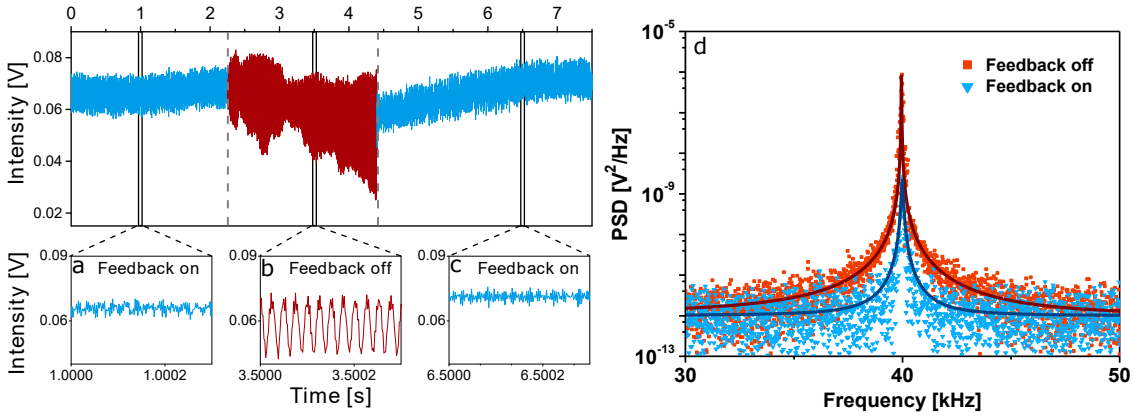

Figure 3.17: Effect of the feedback for the MobOT backscattered signal on the particle motion at P=$2 \cdot 10^{-5}$ mBar : (a) The particle motion amplitude is damped by the feedback. (b) It increases when the feedback is deactivated and (c) returns to a low amplitude oscillation when the feedback is switched on again. Closeup of the PSD in the region of the first harmonic at 40kHz of a particle at 2×10^{-5} mBar without (red squares) and with feedback (blue triangles). Darker lines are Lorentzian fits.

we modulate the laser intensity an AOM according to

$$P_{\text{Laser}} = P_{\text{o}} \times \begin{cases} (1+\epsilon) & \text{if } |\langle V_z \rangle - V_z| > \sigma_V \\ 1 & \text{if } |\langle V_z \rangle - V_z| \leq \sigma_V \end{cases}, \tag{3.96}$$

where P_0 is the laser intensity without feedback and $\epsilon = 7.5\%$ is the laser modulation depth. Since the trap stiffness $k_{\text{trap}} \propto P_{\text{Laser}}$, this scheme increase the stiffness whenever the amplitude changes too quick (similarly as the feedback shown in Fig. 3.7).

Figure 3.17 shows the effect of the feedback on the particle motion at $2 \cdot 10^{-5}$ mbar. When the feedback is switched off, the oscillations increase rapidly and decrease again when the feedback is switched back on. Computing and fitting the FFT we exctract the linewidth increase $\delta\Gamma_{opt}$, which gives us $T_{CM} = 30$ K along the optical axis. Although this temperature is much higher than those shown in previous 3D cooling schemes[54,44], it demonstrates the capability to perform center of mass cooling of a levitated particle.

Conversely in the cavity MobOT we use each axis BFP signal to generate a combination of an analog and a digital feedback schemes. For the z axis we use the analog scheme designed

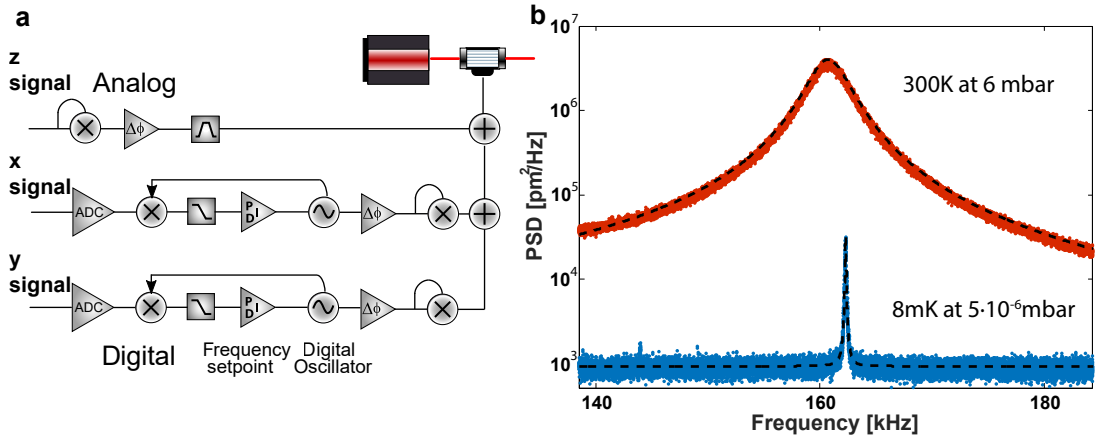

Figure 3.18: (a)Flow diagram to generate the feedback signal using an analog and a digital scheme. The z signal is multiplied itself, phase shifted and band passed. Similarly, the x and y signals are frequency locked to a digital oscillator by means of a phase lock loop (PLL). Then the digital oscillator is phase shifted and frequency doubled. Finally, all axes signals are added and sent to an AOM modulating the power in the optical trap. (b) PSD along the x axis for a particle cooled with the combined feedback at $5 \cdot 10^{-6}$ mbar. The callibration PSD at 6 mbar is shown for comparison.

by Gieseler et al.[44]. For the x and y axis we use a digital scheme designed by Jain et al.[54]. We add the two feedback signals using a signal splitter from [‖] and send the resulting signal to an AOM that modulates the trap depth. Figure(3.18a) shows the flow diagram of the combined feedback scheme.

From our experience, the digital feedback is more convenient than the analog due to the possibility to fine tune the frequencies to be doubled in each experiment (the analog one consists of a physical circuit that cannot be tuned). Also, it provides better phase control of the feedback along the trap frequency fluctuations. However, the digital feedback implementation requires FPGA Hardware and software [**], which make it expensive and limits us to 2 channels/device.

Figure (3.18b) shows the PSD of the particle oscillations under feedback along the y axis

[‖] minicircuits model ZFRSC-42+
[**] HF2LI Zurich Instruments

at $5 \cdot 10^{-6}$ mbar. Using a Lorentzian fit and comparing it with the thermal fluctuations at 6 mbar we infer $T_{CM} \approx 8$mk.

This demonstrates both our capability to cool the three degrees of freedom as well as to keep particles trapped at low pressures which is the second fundamental requirement.

High Finesse Cavity

Our optical cavity is a confocal symmetric Fabry-Perot resonator formed by 25mm radius of curvature mirrors. In order to stay in the resolved sideband regime we work with mirrors with $F \sim 700.000$. This parameters give a $\sim$ 25 kHz cavity linewidth (four times smaller than our mechanical frequency) and a FSR of 6GHz. The mirrors are fabricated by advanced thin films (ATFilms) using a superpolished fused silica substrate coated with a distributed Bragg grating that alternates Ta_2O and SiO_2 layers as high and low index materials. The coating is deposited by Ion Beam Sputtering, which achieves a surface roughness below 0.1 nm RMS and absorption below 1ppm at 1064nm[61]. The mirror's size is around 7.75mm diameter and 4mm thick. They are mounted in a tungsten cylinder mechanically clamped to a main holder. The main holder is shown in Fig.(3.19) and has been designed with large apertures (3cm) to allow optical and mechanical access of the mobile optical traps. To isolate it from vibrations the cavity is mounted on a stack of tungsten spacers separated by 5mm thick viton rubber rods.

Cavity Locking

To drive the cavity mode we want a laser whose linewidth is narrower than our cavity linewidth (25 kHz). We use a Mephisto laser (Coherent) which provide a 1kHz linewidth with some interesting wavelength tuning capabilities[††]. Additionally,we need to maintain a fixed frequency difference between the cavity resonance and the cooling laser beam. In other words,

[††] $\pm$30GHz with 1Hz bandwidth by tuning the temperature of the laser crystal and $\pm$65 MHz with up to 100 kHz bandwidth by using a piezo that compresses the laser crystal

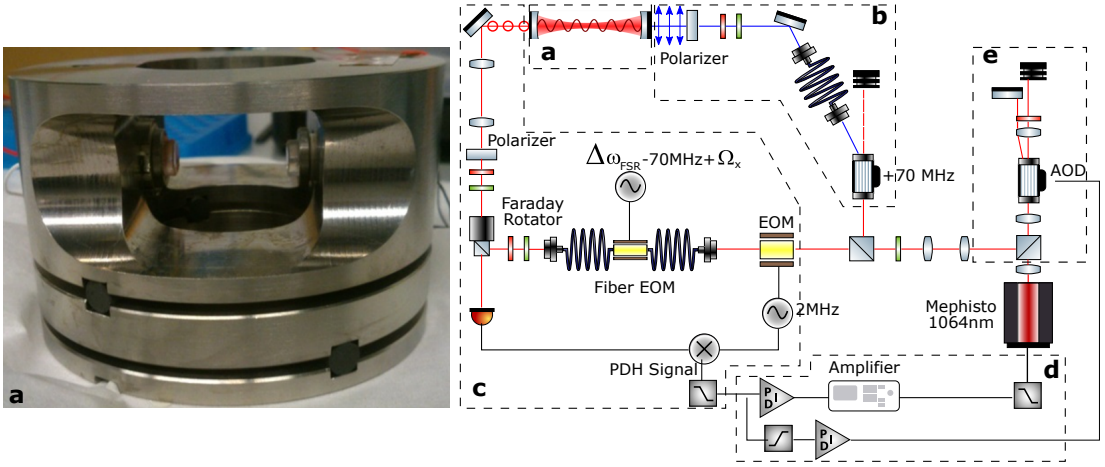

Figure 3.19: Optical Cavity and optics of for the locking scheme. The grouped elements correspond to the optical cavity holder with mirrors mounted (a), cooling beam optics (b), locking beam optics to generate the PDH error signal (c), servos to convert the error signal into a feedback signal to correct the laser frequency (d) and retroreflector (e).

to lock the laser frequency to compensate the cavity and laser drifts. In our experiment we use rather large cavity mirrors, so our cavity length tuning bandwidth using piezoelectric ceramics is limited thus we choose to tune the laser frequency.

To lock the laser to the cavity resonance we use the Pound-Drever-Hall (PDH) locking technique[33]. The PDH lock was devised in the early 1980's based on Pound's work in microwave systems in the 1940's. This technique uses a phase EOM to modulate the laser field at a frequency much higher than the cavity linewidth (2.5 MHz$= \Omega_{PM} > \kappa_{cav}$). Thus the field impinging the cavity mirror E^{in} becomes a phase modulated field E^{in}_{PM}:

$$E^{in} = Ae^{i\omega_l t} \longrightarrow E^{in}_{PM}A = Ae^{i\omega_l t + i\beta \sin\Omega_{PM} t} \tag{3.97}$$

$$\approx A\left(J_o(\beta)e^{i\omega t} + J_1(\beta)e^{i(\omega+\Omega_{PM})} - J_1(\beta)e^{i(\omega-\Omega_{PM})}\right) \tag{3.98}$$

where we have kept only the leading terms (first order sidebands) in the Jacobi-Anger expression.

We see that the beam impinging onto the input cavity mirror consists of a carrier frequency with power $P_c = |A^2 J_o(\beta)^2|/(\epsilon c)$ and two sidebands each at $\pm\Omega_{PM}$ with power $P_\pm =$

$J_1^2(\beta)A^2/\epsilon_o c$.
As a result, the field reflected by the cavity becomes:

$$E_{ref} \approx Ae^{i\omega t}[R(\omega)J_o(\beta) + R(\omega+\Omega)J_1(\beta)ei\Omega_{PM} - R(\omega-\Omega)J_1(\beta)e{-}i\Omega_{PM}] \quad (3.99)$$

Using a photodiode to readout the reflected signal we measure the reflected power:

$$\begin{aligned} P_{det} = |E_{ref}^2| &\approx P_c|R(\omega_l)|^2 + P_\pm[R(\omega_l+\Omega)^2 + R(\omega_l-\Omega)^2] + \\ &+ \sqrt{P_c P_\pm}[R(\omega_l)R^*(\omega_l+\Omega)e^{-i\Omega t} - R(\omega_l)R^*(\omega_l-\Omega)e^{i\Omega t}) + \\ &+ R^*(\omega_l)R(\omega_l+\Omega)e^{i\Omega t} - R^*(\omega_l)R(\omega_l-\Omega)e^{-i\Omega t} + O(2\Omega)] \end{aligned}$$

Since the sidebands are created far from resonance, they are reflected ($R(\omega_l \pm \Omega)$=1) and the signal becomes:

$$\begin{aligned} P_{det} \approx P_c|R(\omega_l)|^2 + P_\pm[R(\omega_l+\Omega)^2 + R(\omega_l-\Omega)^2] + \\ + \sqrt{P_c P_\pm}[(R(\omega_l)^* - R(\omega_l))(e^{i\Omega t} - e^{-i\Omega t})] \end{aligned}$$

The first three terms give a DC term, whereas the last one oscillates at Ω_{PM} with an amplitude proportional to de the imaginary part of the cavity response function (see Fig. 3.3). To gain access to this imaginary part we just mix the signal term with the same oscillator that drives the phase modulation (accordingly phase shifted) and then lowpass the mixed signal. This leads to an error signal whose magnitude is proportional to the frequency detuning between the laser carrier frequency and the cavity resonance as long as they are detuned by $\Delta \leq \kappa$.

Figure (3.20) shows the characteristic profile of a PDH error signal for a laser frequency swept across the cavity resonance .

The PDH error signal is fed to two different PI servos. In the first PI the signal is high-passed to correct the laser wavelength with a bandwidth from 5kHz to 200kHz using an AOD

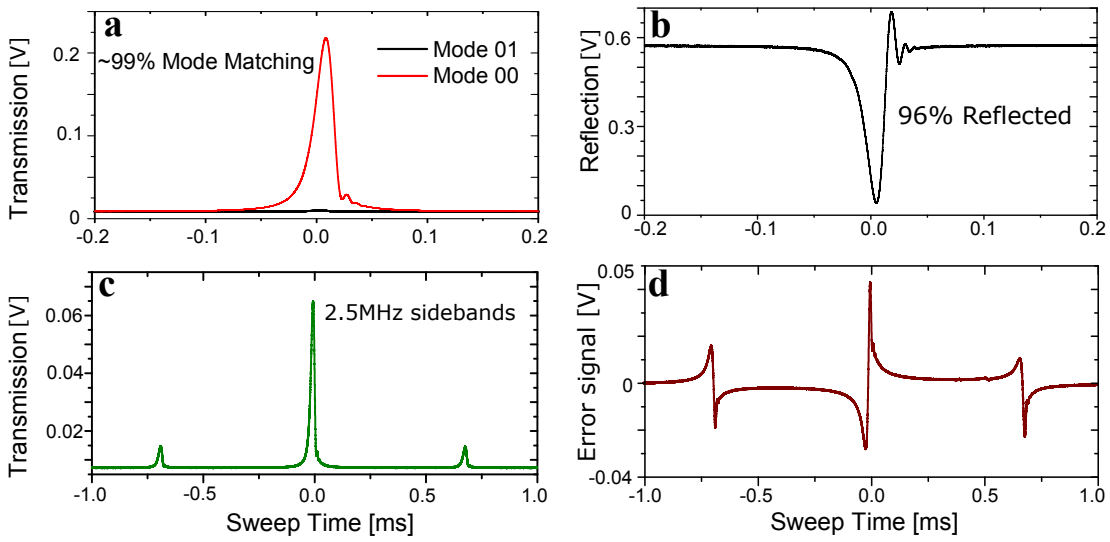

Figure 3.20: Characterization of the optical cavity. (a) Transmited intensity and (b) reflected intensity time trace for our cavity resonance swept at 20Hz. Our mode matching efficiency is around 99% (a) and shows a good impedance matching (b). (c)Cavity transmission of the PDH phase modulated beam featuring the two sidebands at ± 2.5 MHz. (d) PDH error signal. (e) Ringdown measurement of the High Finesse Cavity (blue solid line) and fit (red solid line) used to obtain the cavity photon lifetime $\kappa^{-1} = 20\mu$s.

in a retro-reflector configuration (Fig.3.19e). The other PI servo output signal is amplified and low-pass filtered to drive the laser built-in piezos (Fig. 3.19d). The gain parameters of each servo are manually tuned to obtain the best lock-stability.

Cavity Performance

The cavity lock performance is directly related to the quality of the PDH error signal. In order to have a high SNR error signal for a stable lock we must ensure that the field at the input mirror is properly mode matched with the TEM_{00} cavity mode. To understand the effects mode matching imperfections we can write the incident field $\varepsilon_{in}(r,t)$ as a sum of the TEM_{00} mode (nu_o) and the transverse ones ($\varepsilon'_{in}(t)(r,t)$):

$$\varepsilon(r,t) = \alpha_o \nu_o(r,t) e^{-iw_o t} + \varepsilon'_{in}(r,t) \tag{3.100}$$

which allows us to define a mode matching efficiency η_{cav} as the ratio between the intensity coupled into the cavity and the total intensity I_{in} [121]:

$$\eta_{cav} = \frac{|\alpha|^2}{\alpha_{in}^2} \tag{3.101}$$

Figure 3.20 shows the transmitted power from sweeping the cavity resonance frequency across the TEM_{00} mode and the 2^{nd} brightest mode (TEM_{01}). From there we estimate a mode matching efficiency $\eta \approx 99\%$.
Therefore when the cavity is at resonance an imperfect mode matching ($\eta_{cav} < 1$) results into direct reflection of the the higher order modes onto the PDH photodiode and only a power $\eta_{cav} I_{in}$ couples to the cavity. The reflected intensity becomes:

$$I_{out} = \left(\frac{T-P}{T+P}\right)^2 |\alpha_o|^2 + \varepsilon'_{in} \tag{3.102}$$

Thus we can rewrite a corrected reflection coefficient as:

$$R_o = \eta_{cav}\left(\left(\frac{T-P}{T+P}\right)^2 - 1\right) + 1 \tag{3.103}$$

Figure (3.20) shows the reflected power from a cavity swept across the main resonance. We extract a reflectivity of $R_o \approx 96\%$. Note that in a PDH locking scheme the reflection from high order modes will also interfere with the phase modulation sidebands and add a DC term in the photodetector degrading the error signal. Figure (3.20 c,d) shows the transmited intensity of the phase modulated lock beam when swept across the cavity resonance and the corresponding PDH error error signal used to lock the cavity. The high quality of the error signal allows high stable cavity lock that can last for days.

To experimentally determine the cavity finesse we need the photon lifetime $(1/\kappa)$ and $\Delta\omega_{\text{FSR}}$ (Eq.3.23). The lifetime is obtained from a ringdown measurement. Namely we lock the laser frequency to the cavity resonance and then switch it off very while measuring the transmitted intensity. Fitting the exponential decay of the transmitted cavity field (Fig.3.20) gives a direct measurement of the intracavity photon lifetime $\kappa^{-1} = 20\mu s$ which corresponds to a FWHM $\kappa = 2\gamma_o = 50$kHz. To measure $\Delta\omega_{FSR}$ we amplitude modulate with an EOM the lock laser while sweeping its frequency across the cavity resonance. When the frequency of the amplitude modulation matches $\Delta\omega_{\text{FSR}}$ the amplitude modulation sidebands at $\pm 1\Delta\omega_{FSR}$ overlap together with the carrier in the transmission signal. This gives $\Delta\omega_{\text{FSR}} \approx 2\pi \cdot 6.16$GHz from where we extract a finesse $F = \Delta\omega_{\text{FSR}}/\kappa = 775.000$. Also from $\gamma_o \approx 25$ kHz see that we meet the resolved-sideband condition ($\kappa \ll \Omega_m$).

Cooling beam

The cooling beam in the experiment needs to be detuned from the cavity resonance by several linewidths, therefore we cannot use the same beam to lock and cool the particle. For cooling we use a second beam with the right detuning and orthogonally polarised to the lock

beam as in reference[62] to avoid beating between the two cavity fields. Although the fields are orthogonally polarized the cavity birefringence fluctuations (from pressure changes, thermal fluctuations from intracavity power) still induce a mix in the polarization and causes them to beat. In order to avoid these beats at $\Delta \sim \Omega_m$, we shift the second beam by an additional free spectral range so the beating occurs at ≈ 6GHz and is neither seen by our detectors or particle.

To maintain a fixed frequency between the beams we split the lock laser before phase modulation (Fig.3.21 a) and frequency shift specifically each beam. One beam (cooling) is frequency shifted by 70MHz using an AOD (Fig.3.21 b). The other beam (locking) is phase modulated in a free space EOM and then sent to a fibered amplitude EOM (Fig.3.21 b). The fiber EOM is driven at $\Delta\omega_{FSR} + 70$MHz$+\Omega_x$ at half-wave voltage to deplete the carrier into two strong sidebands. Since the locking beam consists of a carrier and two phase modulated sidebands, each of them creates two sidebands and gets depleted (Fig.3.21 c). Finally we use the upper amplitude modulation sidebands for a PDH lock, obtaining a locking beam and a cooling beam shifted by a FSR$+\Omega_x$. Regarding the lower sidebands, they are detuned by 140 MHz $+2\Omega_m$ from the closest resonance, resulting into a small DC contribution in the PDH photodiode (Fig.3.21 c). With this simple method we can bypass the need of a filtering cavity used in other approaches[62], avoiding extra locking steps and reducing the amount of optical elements in required in the setup.

Cavity Optomechanics with a levitated nanoparticle

Now that we have set our high Finesse cavity and mobile optical we aim to demonstrate optomechanical coupling between our trapped particle and cavity. We start by measuring the effect of the cavity optical forces onto our trapped particle.

Optomechanical Interaction

Using the cavity MobOT, we bring an optically levitated nanoparticle into the TEM_{00} cavity mode and we record the FFT of its motion along the cavity axis at $\Omega_x \approx 190$ kHz (Fig.

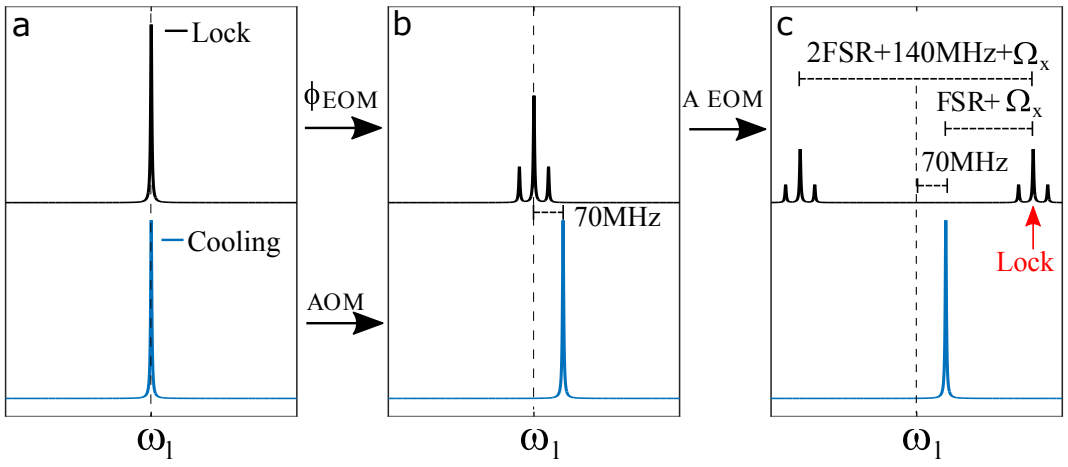

Figure 3.21: Representation of the cooling and locking beam components in the frequency domain centred at the laser frequency. The cooling beam (blue solid line) and the lock beam (black solid line) are split from the same laser beam (a). Then the lock beam is phase modulated to create the characteristic PDH sidebands and the cooling beam is frequency shifted by 70 MHz (b). Finally, the locking beam is amplitude modulated into two new sets of sidebands, totally depleting the carrier frequency (c). The laser is locked at the upper set of sidebands.

3.22)Then, we switch on the lock beam to drive the cavity standing wave and we study the trapped particle dynamics at three different positions. First we place it in the linear slope of the standing wave. At this point the optical force is constant, thus the FFT of the particle signal shows de same resonance frequency as without cavity field (Fig.3.22a). Secondly we move our particle to the node of the standing wave where it does not scatter photons and the gradient force of the cavity is at its minimum. At this point the cavity gradient force results into an inverted harmonic potential that expels the particle and decreases its resonance frequency down to 175 kHz (Fig.3.22a). Finally we do the opposite and bring the particle towards the standing wave antinode. At this point the harmonic potential of the tweezer and the cavity add up and increase the particle resonance frequency up to 205 kHz. The Mechanical frequencies along the other axis remain unaffected as long we set the right MobOT polarization. Note that this frequency shift measurement can also be used to estimate the intracavity power by means of Eq.(1.65), which gives ≈ 0.7 W.

With this configuration is useful to set an heterodyne detection with the signal leaking out of the cavity and see whether we can reach the theoretically predicted sensitivity. Such a

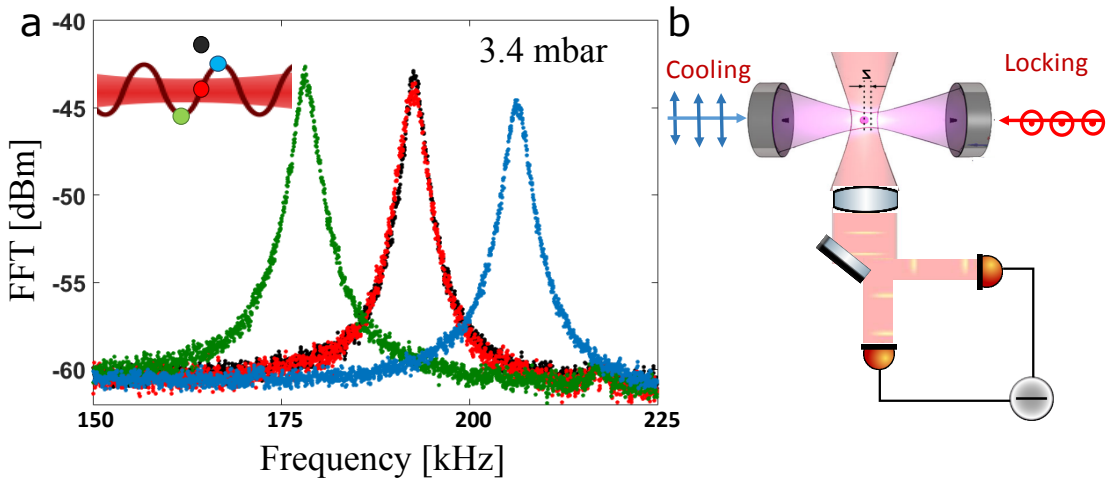

Figure 3.22: Changes in the particle resonance frequency along the x axis (Ω_x) at different points of the cavity standing wave. (a) FFT for particle motion at each position of the standing wave shown by the same coloured dot in the inset. (i.e. Red dots curve corresponds to FFT at the red dot position in the inset, etc.). (b) Scheme of the different optical fields in the experiment and BFP balanced detecion. For this experiment we used a 980 nm tweezer laser and a 0.15 NA collection optics.

measurement would also give access to the other motional quadratures and be an additional tool to infer T_{CM} using sideband thermometry[104].

Figure (3.23) shows a scheme of our heterodyne measurement implementation. Briefly, we pick the locking beam before phase modulation and frequency shift it by 70 MHz. This beam is then overlaped in a PBS with the transmited cavity lock beam and interfered and balanced using a half waveplate and a PBS. Figure 3.23 compares the FFT of the stokes sideband in the heterodyne measurement with our BFP detection. We clearly see that the SNR of the heterodyne measurement is lower than our BFP even with an unoptimized detection configuration that achieved 30 dBm less sensitivity than our current scheme.
The reason behind this low SNR is that, as we expected, the cavity lock beam carries a lot of noise from additional cavity length fluctuation sources, which ends up covering the particle signal. Moreover, the particle resonance frequency is larger than the cavity bandwidth so the it further lowpasses it. This observation agrees well with previous heterodyne and homodyne measurements of levitated nanoparticles inside optical cavities[62]. For this reason we decide to optimize and upgrade the BFP detection scheme instead of trying to improve our cavity

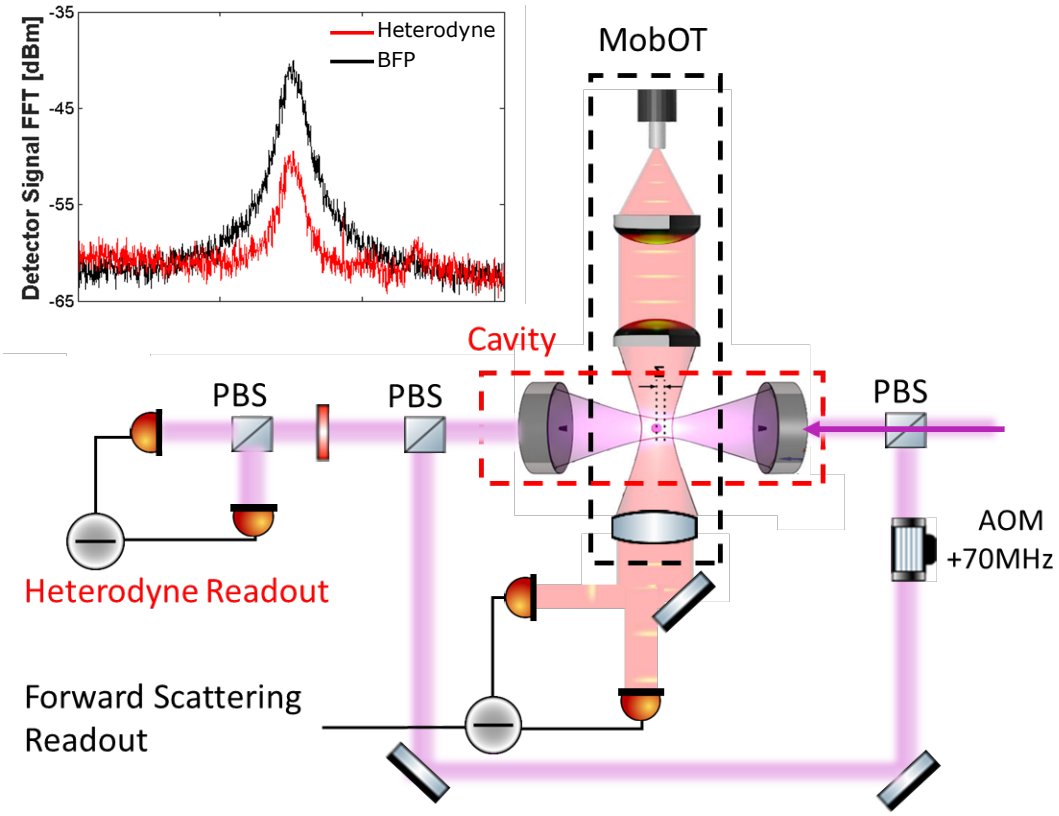

Figure 3.23: Comparison of Heterodyne and BFP detection schemes. The Heterodyne detection splits the lock beam and frequency shifts it by 70 MHz to act as reference beam. The reference beam is then overleaped with the cavity transmitted in a PBS and interfered by means of a λ_2 waveplate and a second PBS. The signal of each port is sent to a different photodiode in a balanced scheme. Top right corner shows the FFT of each measurement scheme centred at Ω_x and the background noise level scaled for SNR comparison.

readout.

Cavity Cooling of an Optically trapped nanoparticle

The next step of our experiment is to harness the optomechanical interaction of our system to perform resolved-sideband cooling of an optically levitated nanoparticle.

Using a weak beam the cavity is locked and the particle its positioned in the linear slope of the cooling beam and its motion recorded at 4 different powers of the cooling beam: 25, 50, 100, and 200 mW. The measurements are repeated each at lower pressures until the particle signal vanishes in the noise floor and during the experiment, the feedback is enabled for the remaining axis (y and z) for pressures below 0.1 mbar.

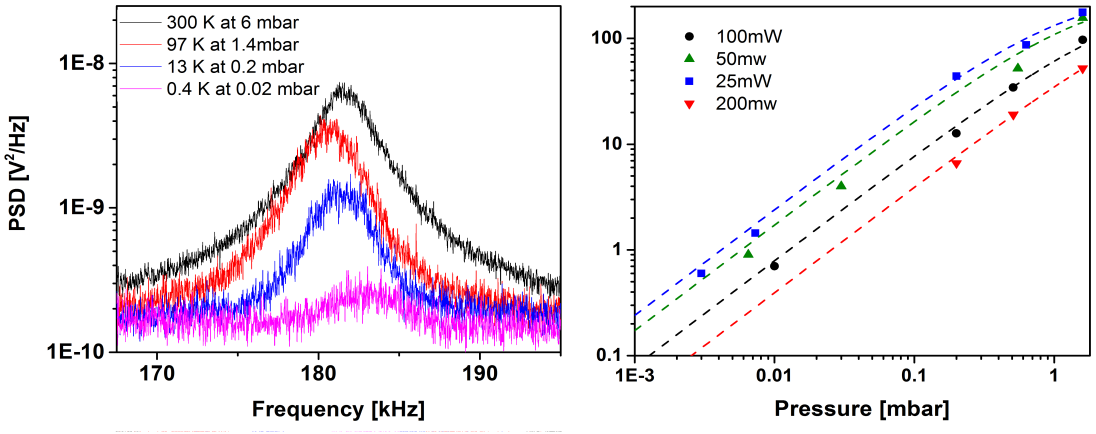

Figure 3.24: Resolved sideband cooling of the particle oscillations at Ω_x along the cavity axis. (a) shows the PSD of the photodiode signal for the particle motion along the cavity axis at different pressures with a 100 mW cooling beam with a detuning $\Delta = \Omega_x$. (b) Shows the T_{CM} achieved vs. the system pressure for different powers of the cooling beam: 25 mW (blue squares), 50mW (green triangles), 100 mW (black circles) and 200 mW (red inverted triangles). The dashed lines of the same color follow the predicted value of T_{CM} from Eqs.(1.40,3.79) using the measured linewidth .

Figure 3.24 shows the particle PSD along at three different pressures for a 100 mW cooling beam. First thing we notice is that the area of the curve decreases as we lower the pressure

in agreement with Eq.(3.78), demonstrating cavity cooling. The linewidth of the mechanical oscillations decreases very little despite lowering the pressure by more than 2 orders of magnitude, which is clear sign of a strong optomechanical dissipation. Fitting the linewidth and subtracting the viscous contribution from the residual molecules we obtain an average cooling rate $\Gamma_{opt} \approx 2\pi \cdot 2600$Hz which achieves $T_{CM} = 0.5$ K at 0.02 mbar. Lower pressures were not recorded as SNR was too low.

The cooling beam also induces a red-shift of the mechanical frequency at 1.4 mbar (red curve Fig. 3.24a). This agrees with the optomechanically induced frequency shift predicted by Eq.(3.89). However, as pressure drops and the cooling reduces the particle amplitude of motion, the frequency blue shifts. This phenomena is intrinsic of optical tweezers and appears in every cooling scheme (e.g. Fig. 3.18). It is caused by the negative sign in the duffing term of the optical force which decreases the stiffness as we get away from the trap center (Fig 1.6). The blue shift increases as pressure lowers and Ω_x ends up blue shifted .

In figure (3.24) we plot the measured T_{CM} vs. the system pressure for different powers of the cooling beam. At higher powers the system reaches lower temperatures as expected until we reach about 1 K where our signal banishes in the noise floor. From the average optical dissipation of each measurement we also show the theoretical prediction for the T_{CM} vs. pressure which agrees well with the measured temperatures. This means that the Γ_{opt} is constant at a given optical power and remains unaffected by pressure changes as expected.

To understand the influence of experimental imperfections in the cooling performance we investigate the effect of misplacing the trap center in the cavity profile. We bring our system to 4 mbar and set thr cooling beam to 100 mW of power. Then the particle is placed at 13 equally spaced positions between a node and the closest antinode of the cooling beam standing wave (Fig. 3.25a top) and the FFT of its oscillations is recorded (Fig. 3.25b). Figure (3.25a bottom) shows the estimated T_{CM} at each particle position. As expected, the lowest temperatures are achieved at the linear slope of the standing wave (≈ 133 nm from the antinode). However, significant cooling is still achieved even if the particle deviates ± 50 nm from this ideal spot.

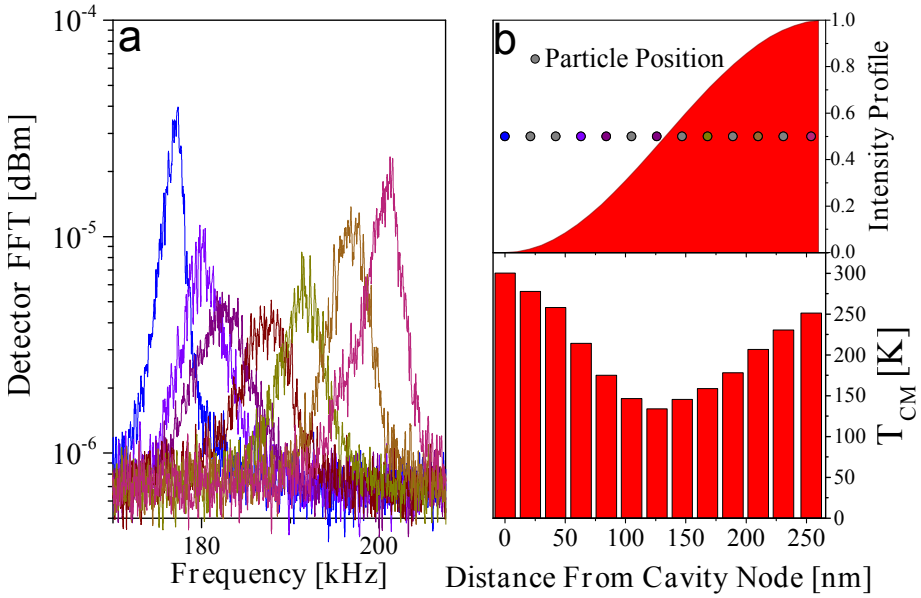

Figure 3.25: Cooling performance as a function of the optical trap misplacement in the cavity standing wave. (a) FFT for different trap positions in the standing wave of the cooling beam. (b) Position of the trap centre in the standing wave intensity profile versus the distance from the cavity node (top) and T_{CM} estimated for each position (bottom). The FFT color match the particle position colours.

Additionally, T_{CM} shows an assymetry for deviations towards and against the antinode. The reason is that despite both displacements result equally unfavourable for cooling, the particle interacts with more photons as it approaches the antinode and with less when it approaches the node. Thereby cooling gets worse for the later.

Figures (3.22 and 3.25a) also show that Ω_x shifts when misplaced in the cooling beam standing wave. Since the detuning on the cooling beam is fixed and is not corrected during the experiment, a mechanical frequency change also degrades the cooling performance.

To investigate this effect we plot T_{CM} versus the frequency mismatch between the cooling beam detuning (Δ) and the mechanical frequency (Ω_x) of our previous experiment (Fig3.25a,b). Then, we repeat our temperature measurements fixing the trap at the linear slope and only

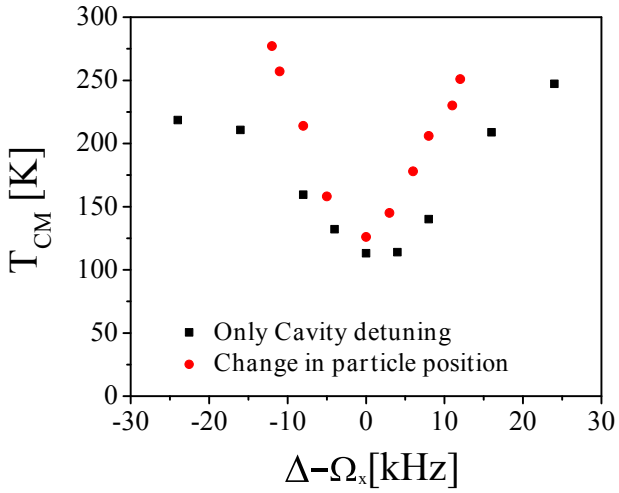

Figure 3.26: Center of mass temperature (T_{CM}) as a function of the frequency mismatch between the cavity detuning and the particle frequency ($\Delta - \Omega_x$). Black squares correspond to measurements for a particle siting in the linear slope of the cavity standing wave while manipulating the cavity detuning Δ and red circles correspond to a cavity with a fixed detuning and an optical trap placed at different position of the cooling beam standing wave.

changing the detuning of our cooling beam (Δ) to achieve the same mismatch ($\Delta - \Omega_x$). The results are compared in Fig. (3.26) and we find that, although frequency mismatching decreases the overall cooling performance, the effects of misplacing the trap are more significant, and thus critical for the performance of the experiment.

Conclusions and Outlook

In this section we have presented our efforts to develop an optical trap that couples to a high Finesse cavity. We aim to bring together the benefits of the two techniques: on the one hand the capability of optical tweezers to maintain optically trapped particles in high vacuum and on the other hand the high cooling rates provided by the optical cavity. Our experiments in the early development stage of the setup have already shown both confinement in high vacuum ($5 \cdot 10^{-6}$ mbar) and coupling to a cavity that provides high enough cooling rates to reach ground state according to our calculations.
These experiments also helped us to find the detection scheme that could reach higher sensi-

tivity in our setup which, in agreement with what has been reported so far in the literature of levitated nanoparticles, is the Backfocal Plane interferometry. With this knowledge we have upgraded the the trap in the setup to bring the system sensitivity closer to resolving ground state.

We also shown that decoupling the trapping and cooling mechanisms allows us to test the influence of experimental imperfections (misplacement of the optical trap in the cooling beam and mismatch between Δ and Ω_x) in the cooling performance, resulting in positioning as the most critical parameter.

Besides all the effort put into building a setup to bring a levitated nanoparticle to its motional ground state at room temperature, our experimental configuration also allows to implement further experiments, in particular in the field of thermodynamics. It would be interesting to reproduce the thermodynamic cycles and protocols described in Chapter 2 in the underdamped regime, as the MobOT allows fast and precise modulation of the optical potential. This would not be possible in a setup whose only optical field comes from the cavity, since the bandwidth at which the potential can be modulated is limited by $\gamma_o \approx 25kHz$.

Regarding our Mobile optical trap system, we believe it can be further implemented in levitating nanopartcile systems due to its simplicity, robustness and affordability. Finally, MobOTs also will enable experimental configurations where a levitated nanoparticle is brought close to other objects such as membranes, ions, etc.

If you cannot do great things, do small things in a great way.

Napoleon Hill

4

Optomechanics with plasmonic nanocavities

Miniaturization of the optical cavity can overcome the weak optomechanical coupling strength G of optically trapped systems for cavity optomechanics. In this chapter we will plasmonic nano-cavities to increase G by several orders of magnitude. Since the coupling strength is independent of the mechanical dissipation Γ, our experiments will be performed in liquid allowing the nanoparticles to reach the cavity by diffusion. In this overdamped regime will also use a binning calibration process to resolve the passive modulation of the optical potential caused by the particle fluctuations (SIBA) and study the optimal detuning regime to boost optical trapping performance.

Introduction

First experiments on plasmonic trapping were done in 2006 by Volpe et al. who used localised surface plasmons in gold pads to trap micron-sized dielectric nanoparticles[124]. Although first experimental implementations of plasmon-assisted trapping showed great potential[97,48,98], they remained limited, because of photothermal effects, to object sizes greater than 100 nm. To further improve the trapping efficiency, an alternative strategy inspired in Babinet's principle[18] can be adopted. This consists on replacing the plasmonic structure by its negative milled on a flat metalic surface. For example a gold pad is substituted by a hole in a gold film that acts as cavity and improves as well the heat dissipation through the film. In this strategy the trapped specimen also achieves a large overlap with the cavity field and play an active role in the trapping mechanism, the so called self-induced back-action (SIBA) effect[58]. In this regime the cavity resonance shifts adiabatically with the changes in the particle position, resulting in dynamic optical trap whose long-term stability requires much lower average intensities as compared to a static potential[58]. Following this approach, dielectric objects of tenths of nm size and individual biomolecules have been trapped with less than 10 mW of optical power[58,13,91]. The SIBA hypothesys has been indirectly validated by the enhanced trapping performance observed in the experiments, nevertheless direct observation of the optical potential modulation has never been observed.

Our aim in this chapter is to describe a nanoplasmonic trap from the cavity optomechanics perspective and show how this can be used to boost the nanocavity-nanoparticle interaction by trapping gold nanoparticles (GNP) as a large polarizability object. We will start by describing and simulating the optical response of GNP and nanocavities to estimate the optomechanical coupling strength of these systems. Then we will present the optical trapping experiments featuring the largest single photon optomechanical coupling for an optically trapped particle, which will allow us to directly resolve the dynamic modulation of the optical potential. Finally we will discuss which detuning regimes are most efficient for trapping and the interest of further developing nano-optical cavities for cavity optomechanics with optical traps.

The interaction of metals with optical fields is remarkably different from dielectric particles. This is caused by the presence of free electrons in the conduction band, whose optical response is not well described by the Lorentz model (Eq. 1.2). To account for their contribution to the polarizability we describe them using the Drude-Sommerfeld model[4]:

$$m_e \frac{\partial^2 r}{\partial t^2} + m_e \Gamma_e \frac{\partial r}{\partial t} = e E_o e^{-i\omega t} \tag{4.1}$$

where the damping term Γ_e is equal to the fermi velocity ν_f divided by electron mean free path l ($\Gamma_e = \nu_f / l$). Since electrons in the conduction band are unbound, this model considers that the only two forces experienced by the electrons are the driving electric field and a damping term.

Solving this equation, gives the dielectric function $\varepsilon(\omega)$of an electron gas:

$$\varepsilon_{Drude}(\omega) = 1 - \frac{\omega_p^2}{\omega^2 + i\Gamma\omega} \tag{4.2}$$

where $\omega_p = \sqrt{n_e e^2 / (m_e \varepsilon_o)}$ is the volume plasma frequency and n_e the density of free electrons.

Adding the contribution of the free electron gas and the bound electrons (see Lorentz Model in chapter 1) finally gives the dielectric function for gold:

$$\varepsilon_{gold} = 1 - \frac{\omega_p^2}{\omega^2 + i\Gamma_e\omega} + \frac{\tilde{\omega_p}^2}{(\omega_o^2 - \omega^2) - i\gamma_e\omega} \tag{4.3}$$

where m is the effective mass, γ_e the damping rate (mostly radiative) and $\tilde{\omega_p}^2$ is the plasma frequency for bound electrons. Thereby, the dielectric function of gold is just the sum over the bound and unbound electron densities properly weighted[17].

Figure 4.1 shows the real and imaginary part of the electric permitivity of gold measured

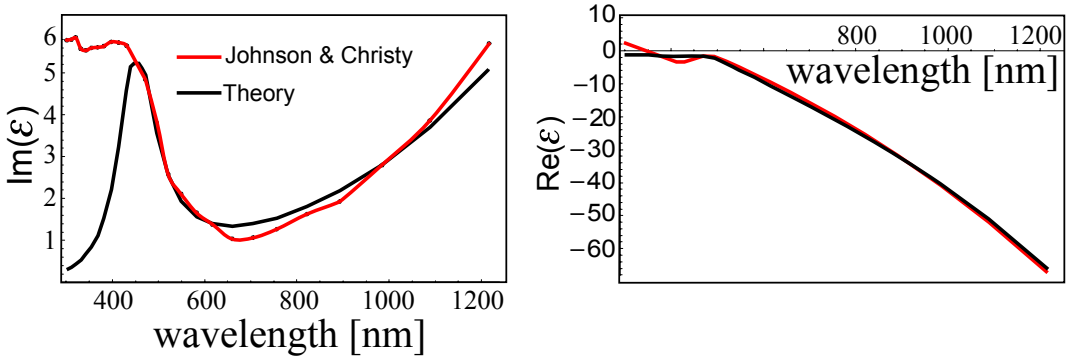

Figure 4.1: Dielectric function of gold: Experimental values (red solid line) extracted from reference[56] and Drude-Sommerfeld plus Lorentz model (black solid line). Figure adapted from[90].

experimentally in reference[56] and the model prediction (Eq.4.3). They show very good agreement down to wavelengths of 500nm, where the effects of more than 1 resonance frequency ω_o needs to be taken into account. Contrary to dielectrics, gold possesses a negative permitivity that leads to a high reflectivity accompanied by a strong absorption inside the metal. Although this limits the maximum optical power that can be used for trapping, it is partially compensated by the higher polarizabilities resulting from the large real and imaginary values of the permittivity. As a result the light-matter interaction in experiments using low power is stronger can be enhanced using metals.

Figure 4.2 compares the value of the normalized polarizability $(\varepsilon - \varepsilon_m)/(\varepsilon + 2\varepsilon_m)$ for a gold and a silica nanoparticles and we see that the former is about 4 times larger (1 vs. 0.26) for NIR wavelengths. The gold nanoparticle also features a plasmon resonance around 532 nm that increases its polarizability by an order of magnitude at expenses of larger absorption.

Plasmonic traps

When driven by an optical field the collective oscillations of the free electron cloud create charge density oscillations with distinct resonance frequencies (see Fig4.2), the so-called plasmons[90]. The negative oscillations respect to the positive lattice lead to a large enhancement of the near field at the interface of the metal and a dielectric[90]. This near field enhancement

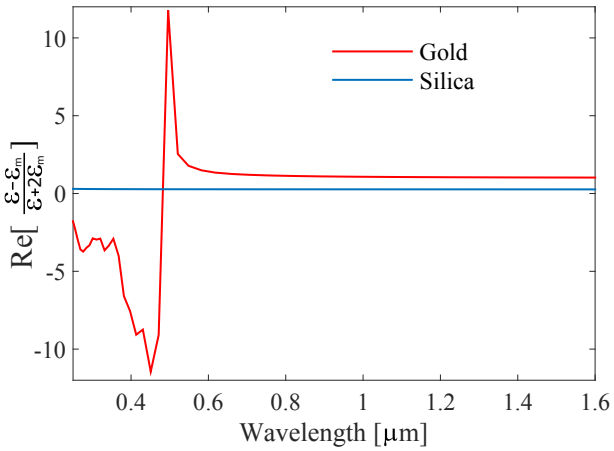

Figure 4.2: Normalized polarizability for silica (blue) and gold (red) in the visible and NIR regime. Gold nanoparticles feature 4 times larger polarizability than silica in the NIR regime. Additionally, the gold nanoparticle sustains a plasmon resonances at $\approx 532nm$, which further increases tenfold its polarizability. The calculations have been made using the experimental values from[56] for gold and[71] for silica.

on top of the field exponential decay leads to strong gradient optical forces, which can be used to trap high refractive index nanoparticles. These can be further enhanced by using the right geometry (pointy), that results in larger charge accumulations in smaller volumes. Consequently, a suitable geometry for our plasmonic cavity will feature a gap with pointy edges, such is the case of a bowtie nano-aperture (BNA).

Bowtie Nano Apertures

We use BNA previously designed by our group[13]. These cavities are fabricated by focused ion beam milling (FIB) in a 100 nm thick Au film evaporated on a coverslip (see Fig. 4.3a). The cavity parameters such as mode volume (V_m) and optical losses (γ_o) are given in principle by the material design. However, the end result varies depending on the fabrication parameters such as gold lattice quality and final shape of the structure. Figure (4.3b) shows the simulated transmittance spectra for a BNA of 85 nm gap and 180 nm length immersed in water for the visible-NIR range. Depending on the polarization of the excitation beam, the cavity features

two distinct resonances.

The stronger resonance is for the polarization along the small gap (transverse) which happens around $\approx$ 1000 nm while a weaker resonance appears around 700 nm for polarization along the large gap (longitudinal). Note also that around 600nm, which is the bound electrons resonance frequency, the absorption increases and the transmission drops to 0.

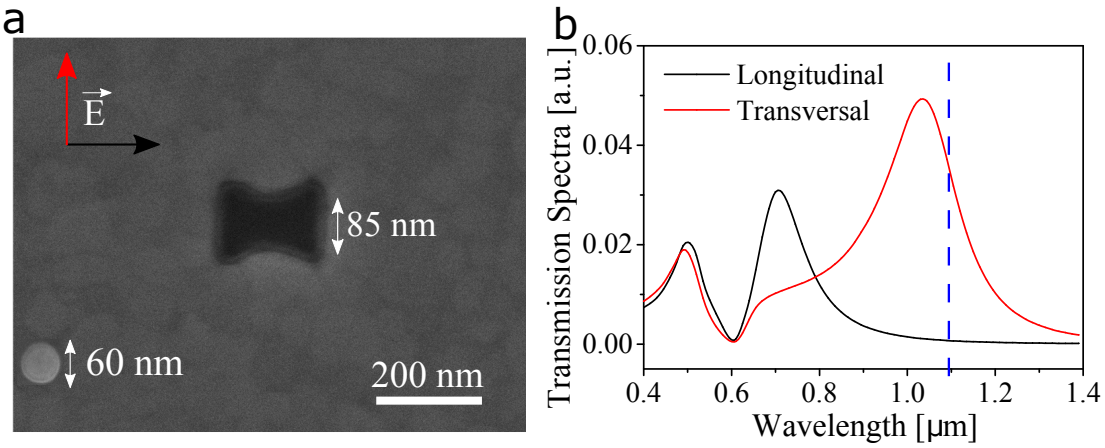

Figure 4.3: Bowtie Nanoaperture (BNA) in 100nm gold film. (a) Image taken with electron microscope showing a BNA in the center (85 nm gap) and a gold nanoparticle in the bottom left corner (60 nm diameter). (b) shows the simulated transmittance for the same BNA for longitudinal and transverse polarizations defined in (a). The dashed line corresponds to the laser wavelength of 1064 nm used in our experiments.

To deliver gold nanoparticles to the BNA the structure is sealed in a liquid chamber containing a dilute suspension of gold nanoparticles[*]. The liquid chamber consists of two thin coverslips separated by a thin layer of vacuum grease [†] at their edges. To screen from unwanted Van der Waals interactions between the gold nanoparticles and the gold substrate we use trimethylammoniun bromide (MTAB) at 10 mM. The optomechanical coupling strength is maximized by allocating particles that maximise the polarizability to optical mode volume ratio. Specifically we chose 60 nm diameter nanoparticles for our 85 nm BNA with resonance close to 1064 nm. Using gold instead of dielectric nanoparticles not only increases by

[*]BBI Solutions
[†]SG10 Corning

four times the cavity frequency shift, but they can also sustain their own plasmon oscillations further enhancing the cavity field.

We characterize the spectral response of the system performing finite element simulations with the RF module of the commercial Software COMSOL Multiphysics. The simulated geometry consists of semi-infinite glass and water media interfaced with a 100 nm thick gold film patterned with a BNA. Inside the cavity we implemented a spherical particle (radius 30nm), whose refractive index is changed from water ($n_w = 1.33$) for no particle in the cavity, to polystyrene ($n_p = 1.57$) and gold (based on Johnson and Christy' data[s6]). The illumination is provided by a monochromatic plane-wave propagating along the z-direction (perpendicular to the interface) and polarized along the 85 nm gap.

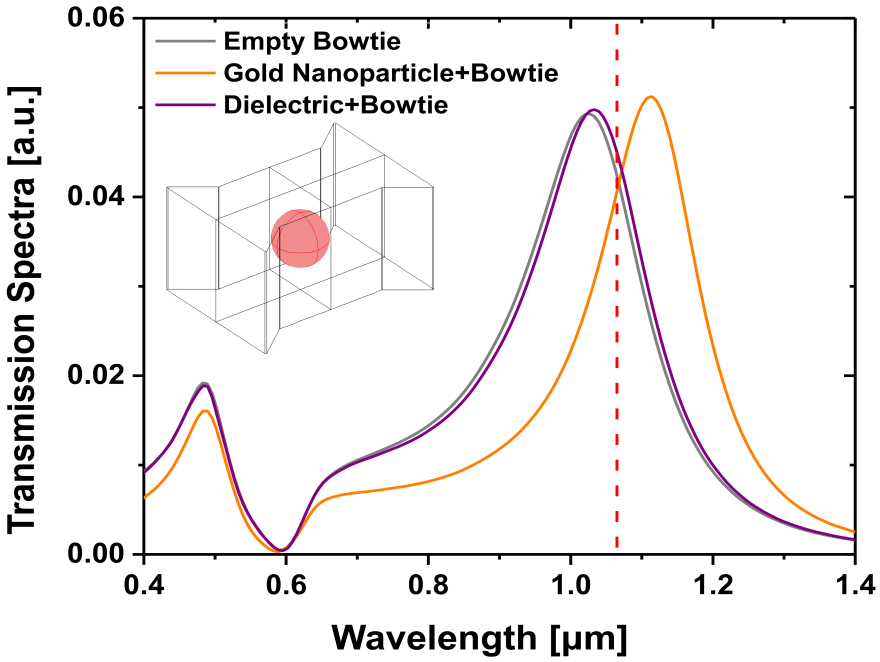

Figure 4.4: Simulated transmission spectra for a Bowtie nanoaperture milled in a 100nm gold film with an optically trapped gold particle (yellow solid line), dielectric particle (purple solid line) and without particle (grey solid line). The dashed line at 1064 nm shows the wavelength used to excite the structure in our experiments. The inset shows the simulated geometry.

Figure 4.4 shows the evolution of the calculated transmittance spectra of the BNA without any trapped object, with a polystyrene bead and a GNP. The red dashed-line corresponds

to the incident laser line at 1064nm. Calculations show a resonance shift of 100nm or $\delta\omega_c \approx 2\pi \cdot 12$ THz induced by the presence of the gold nanosphere. This is a exceedingly large frequency shift when compared with the case of a dielectric sphere or other optomechanical systems[8].

The fact that no other peaks appear in the spectra confirms that the introduction of the nanoparticle does not excite new modes in the visible-NIR spectra. The resonance in presence of the particle also features a narrower linewidth (113 nm for the empty BNA vs. 85 nm for the BNA in presence of a gold nanoparticle) due to the narrower gap between metal surfaces. This a linewidth results in an optical quality factor $Q \approx 10$ which agrees with the reported values for gold nanostructures[69,20] and sets the system into the bad cavity regime where its resonance shifts adiabatically with the particle motion.

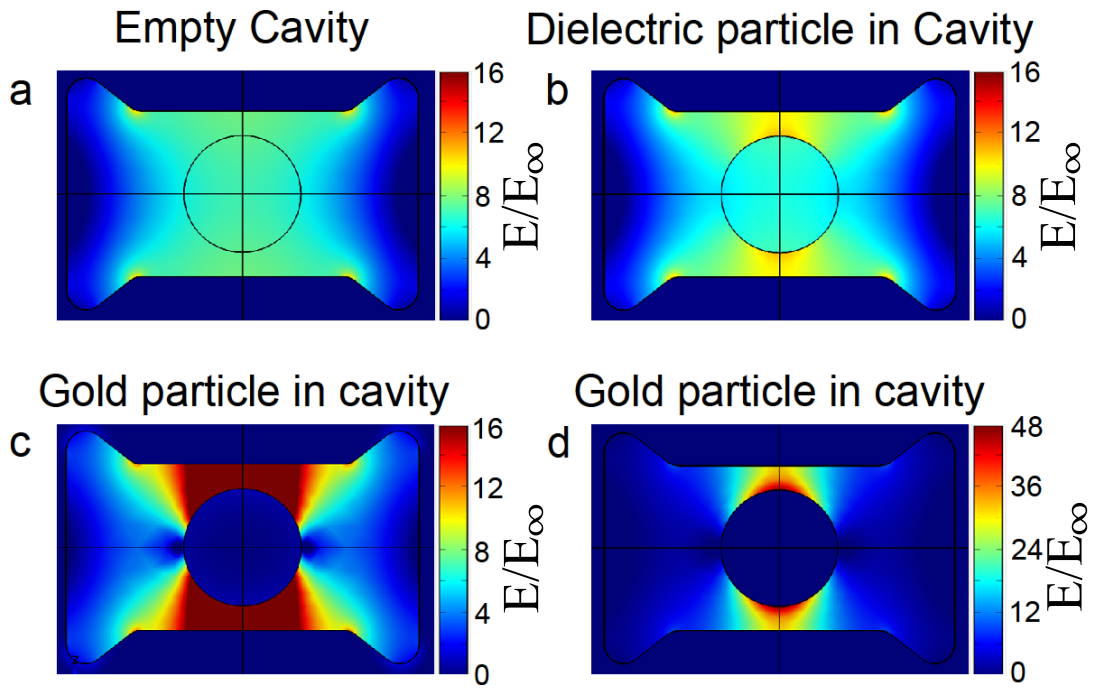

Figure 4.5: Calculated maps of the electric near field enhancement for an empty BNA (a), and a BNA hosting a dielectric (b) and a gold nanosphere (c,d) in its centre. (a-c) use the same scale for comparison of the mode profile.

Figure (4.5) shows the electric near field intensity enhancement at 1064 nm for an empty

BNA, a BNA with dielectric nanosphere and a BNA with a gold nanosphere. Since no other modes are excited the mode volume does not increase significantly between the three cases as expected. However, the presence of a higher polarizeable object increases significantly the intensity in the central gap region between the BNA walls and the particle. The near field enhancement plots also show that the field penetrates inside the particle for the dielectric case but not in the case of a metallic particle which explains the larger frequency shift. Finally the simulation also shows that the presence of a metalic nanoparticle increases the near field up to 4 times compared to the case of a dielectric of the same size (i.e. from a factor 10 to a factor 40 enhancement). This further increase optical trapping potential.

Self-Induced Backaction

The simulated spectra shows that trapping a GNP induces a shift $\delta\omega_c \approx 2\pi \cdot 12\text{THz}$ comparable to the cavity linewidth $\Gamma = 2\pi \cdot 10\text{THz}$. In these conditions the modulation of the optical potential due to SIBA should be observable[89]. Despite the large value of $\delta\omega_c$ is it is still much smaller than ω_c so we can still describe the particle-cavity interaction using a perturbative approach[89]:

$$\delta\omega_c(r) = \omega_c \frac{\alpha}{2V_m} f(r_p) \tag{4.4}$$

Therefore for an incident laser at frequency ω, a cavity with a Lorentzian resonance profile and an adiabatic response we can Taylor expand the intracavity intensity for the laser detuning Δ as:

$$I(\omega_c) = I_o \frac{(\Gamma/2)^2}{(\Delta - \delta\omega_c)^2 + (\Gamma/2)^2} \approx I_{opt} - \frac{2\delta\omega_c(r)\Delta}{\Delta^2 + (\Gamma/2)^2} I_{opt} + ... \tag{4.5}$$

where $I_{opt} = I_o(\Gamma/2)^2/(\Delta^2+(\Gamma/2)^2)$ is the empty cavity profile. This expression shows that in the lowest order approximation the system has two main contributions to the intracavity intensity. The first comes from the empty cavity I_{opt} resonance profile and the second

from the dispersive frequency shift $\delta\omega_c(r)$ that appears in presence of a particle. The later is related to the SIBA effect and determines how changes in the particle position modify the optical potential. Consequently the stiffness of the plasmonic trap κ_{tot} can be decomposed as the sum of two contributions:

$$\kappa_{tot} = \kappa_{opt} + \kappa_{SIBA} \tag{4.6}$$

with κ_{opt} depending on the cavityresonance profile and κ_{SIBA} originating from changes in the particle position that affect the intra-cavity field (second term in Eq.4.5).

Defining a SIBA parameter as in reference[89]:

$$\nu_{back} = \frac{\delta\omega_c(r)}{\Gamma} \tag{4.7}$$

The contributionκ_{SIBA} has an overall impact in the stiffness of the system when the value of ν_{back} values close to or larger than 1[89], meaning that the cavity resonance shift is large enough to produce a significant change in the amount of coupled photons. This is the case shown in our simulations where $\nu_{back} = 1.17$. Note that maximising ν_{back} for a fixed cavity linewidth is equivalent to maximise the optomechanical coupling strength $G = \partial\omega_c/\partial x$.

The optomechanical coupling G for this system can be estimated from the simulated spectra shown in Fig.(4.4) as $\delta\omega_c(r)/\delta x = 2\pi \cdot 150$GHz/nm, where $\delta x = 80$ nm is the distance that the particle needs to cover from the centre of the cavity to the outside. This value compares well with the one reported in a previous plasmonic optomechanical systems of similar dimensions[116] and is much greater than the typical values attained with other optomechanical systems[8,64].

Experimental Setup

The experimental setup consists on a upside-down home-made inverted microscope with the sample mounted on a nanopositioning stage. A continuous-wave 1064 nm Nd-YAG laser beam is focused onto the sample with a 40x microscope objective (0.65 NA). The power of

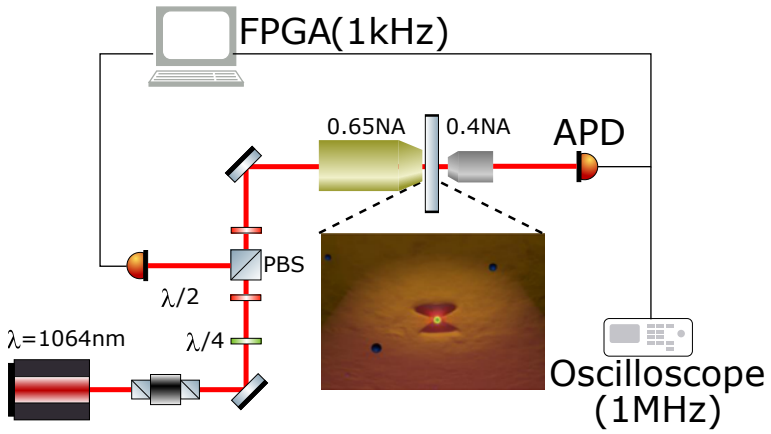

Figure 4.6: Schematic view of the experimental setup. A 1064 nm linearly polarized laser is focused onto the sample at the BNA position with a 0.65 NA objective. The beam intensity is controlled with $\lambda/4$ and a $\lambda/2$ waveplates and a PBS. The transmitted light is collected with a 0.4NA objective and sent to an APD. The signal is monitored in real time at 1 kHz using an FPGA DAQ card and the data is collected using a 1 MHz digital oscilloscope.

the excitation beam is controlled with a $\lambda/4$ and a $\lambda/2$ wavelplates before a PBS and it is limited to a maximum of 10 mW at the sample plane. The beam polarization is controlled using an additional $\lambda/2$ after the PBS. Finally the transmission of the trapping laser through the nanocavity is collected with a 20x NIR objective (0.40 NA) and sent to an avalanche photodiode (APD) (Fig. 4.7). The APD signal is recorded at 1 MHz with a high resolution digital oscilloscope [‡]. Trapping events are simultaneously monitored by splitting the APD signal to a 1 kHz sampling rate FPGA data acquisition card.

We align the polarization of the laser beam to the BNA aperture by maximising its transmission. Figure (4.7a) shows the transmissivity of the BNA as a function of the incoming beam polarization which is maximum when aligned along the 85 nm aperture. To fine tune the working point of the resonance spectra we build an array of 85 nm gap BNA with increasing length size. As the length of the BNA increases its resonance frequency slowly red-shifts. Figure (4.7b) shows the transmission for the different BNA of our array. The transmission increases with the length size of the BNA until optimum resonance is reached (BNA 11 in Fig.4.7), and then it decreases.

[‡]Keysight S-Series 12 bit

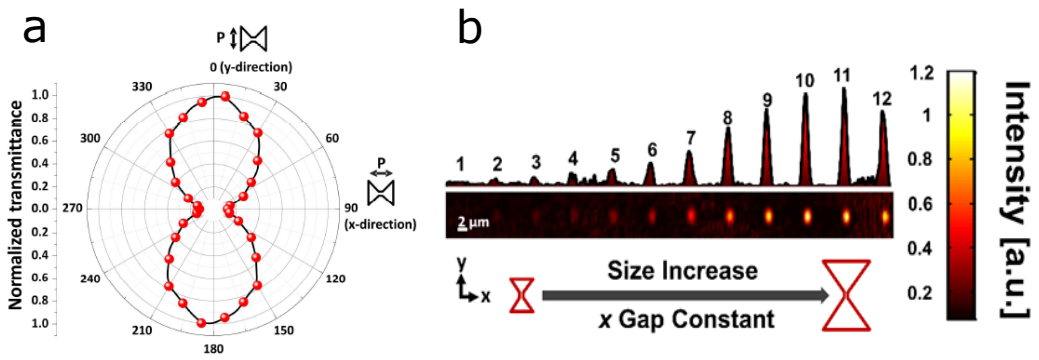

Figure 4.7: BNA transmission profiles. (a) Shows the normalized transmittance of a BNA for different incoming polarizations. (b)Experimental transmission map for different BNA with increasing size. The gap along the x axis is fixed at 85 nm while the dimension of the BAN increases along the array. The polarization of the laser is aligned along the x axis. The top profile shows the transmitted intensity as we sweep through the centre of the nano-array. The bottom plot shows a 2D colourmap of the BNA array transmission.

Experimental Results

When a GNP gets trapped in the nano-cavity a red-shift $\delta\omega_c \sim \Gamma$ leads to one of the three different situations depicted in Fig. (4.8a,b). We refer to these different regimes as: blue-shifted, resonant and red-shifted (Fig. 4.8a (i), (ii) and (iii)) respectively.

In the blue-shifted regime, the cavity mode is set blue-detuned by $\Delta \sim \Gamma$ from the excitation wavelength. As soon as an object is trapped, the resonance red-shifts towards the laser line increasing the local field and transmitted light (Fig. 4.8a (i)). This case is the one most reported in the literature[58,133,91,59].

Conversely in the red-shifted regime, the presence of the particle leads to a strong decrease in the coupled optical power (Fig.4.8a). In these conditions, trapping becomes highly inefficient due to the shallower optical potential that requires a higher trap power to keep the nanoparticle.

Finally in the resonant regime the cavity mode is set to be slightly blue-shifted $\Delta \sim \delta\omega_c(r)/2$ from the excitation laser. When trapping occurs, the system symmetrically red-shifts through the resonance resulting in the transmissions of empty and trapping states to be comparable (Fig. 4.8a(ii) and 4.4). This configuration is foreseen to be the most favourable for SIBA

trapping because, as the particle leaves the optical potential, the system crosses the resonance leading to an increase of photons coupled to the nano-cavity. Remarkably this regime has not been studied in previous plasmon trapping experiments[58,133,91,59] due to the low values of ν_{back} reached in experiments with dielectric particles.

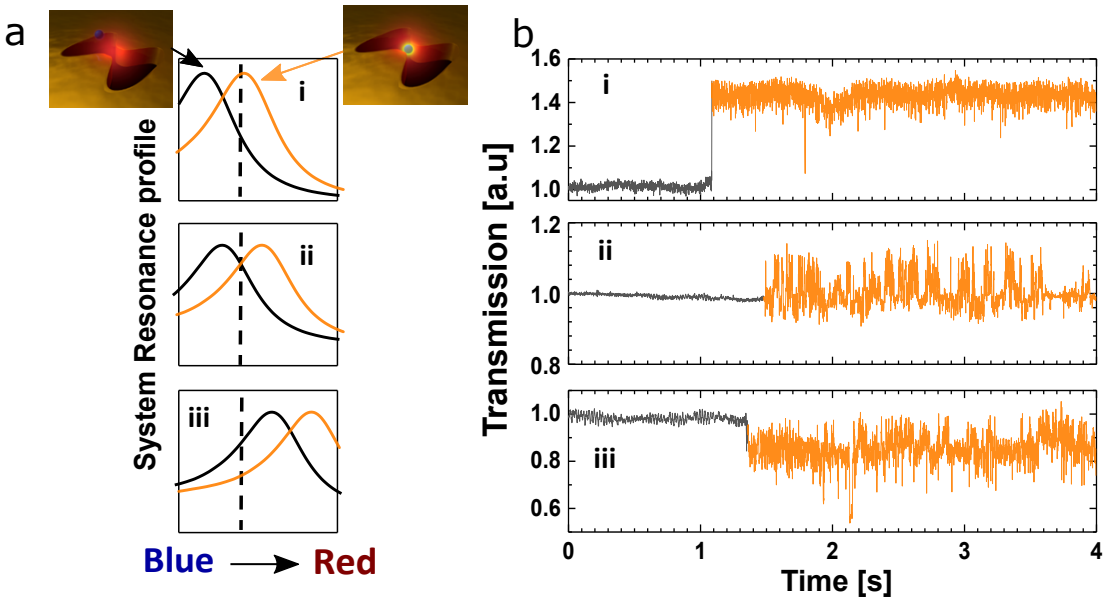

Figure 4.8: Experimental cavity resonance frequency shifts. (a) Shows the Cavity resonance shift for 3 possible detuning regimes: (i) blue-shifted, (ii) resonant and (iii) red-shifted. The black trace corresponds to an empty trap and the orange one to a trapped gold nanoparticle. The dashed line represents the excitation laser at 1064 nm. (b) Experimental transmission time traces for the three detuning regimes. Transmission intensity has been normalised to 1 for the transmission of the empty structure. We used the BNA labelled 8, 10 and 12 in Fig.(4.7) for the regimes i, ii and iii, respectively.

To experimentally reproduce these regimes we used the confocal scans presented in Fig. (4.7b) and selected BNA 8, 10 and 12 corresponding to the blue-shifted, resonant and red-shifted regimes, respectively. Figure (4.8b) shows an experimental time trace with a trapping event for each of these BNA. The black trace corresponds to the transmitted signal for an empty trap and in orange when a single GNP is trapped. As expected from the earlier classification the number of transmitted photons increases and decreases when the object is trapped under blue-shifted and red-shifted regimes, respectively. Similarly, the transmission oscillates around the empty trap value for the resonant regime. These results are in good agreement with the simulated frequency shifts shown in Fig.(4.4). In the following experiments we fo-

cus our attention on the blue-shifted and resonant regimes, i.e. (i) and (ii), to determine which is better suited for trapping at low powers.

Calibration of the optical potential

To characterize the optical potential we calibrated the stiffness of the system κ_{tot} following the power spectral method (see chapter 1). Figure(4.9) compares the PSD of a trapped particle (blue) with one of an empty trap (grey) for a 10s signal at 1.9 mW excitation laser power. From the fit of the PSD to a Lorentzian curve, we obtain $\kappa_{tot} = 4.51$fN/nm, which corresponds to a normalized value of 2.4 fN/nm for an optical intensity of 1 mW/μm^2. Due to the large polarizability of the GNP this normalized stiffness is the largest experimental value reported for plasmon trapping systems[65]. Although this approach provides a stiffness value for the trap it averages out any dynamic SIBA contribution due to the large acquisition time $\sim$s compared to the trap relaxation time $\tau = 1/f_c$. Therefore we need another calibration method if we want to deconvolve complex time dynamics of the trap.

To observe the modulation of the optical potential we apply the following binning procedure to the data. A bin time above the trap relaxation time of 80ms is chosen, resolving fluctuations in the trap stiffness while still providing a reliable trap calibration. The autocorrelation function for each bin is computed and then the trap relaxation time as described in Eq.(1.63) is obtained with a linear fit.

Figure (4.9) shows a sample of processed data for a $\sim$ 3s time-trace. Two different groups of autocorrelation curves can be distinguished: those corresponding to an empty trap (grey) and those with a single trapped GNP (blue). The linear fits are plotted in orange.

Post-selecting only trapping events, we use the values of τ to obtain the κ_{tot} for each bin and build a stiffness probability density function $\rho(\kappa_{tot})$ that contains the information about the modulation of the optical potential in the presence of the trapped particle.

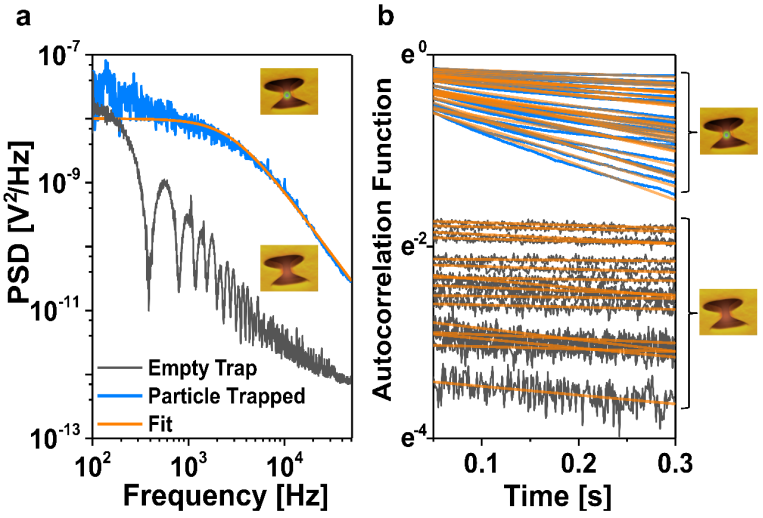

Figure 4.9: Calibration of a plasmonic cavity trap in the blue-shifted regime. (a) Power spectral density for an empty trap (grey), and a single GNP trapped (blue). The Lorentzian fit (orange) gives a trap stiffness of $\kappa_{tot} = 4.51$ fN/nm.The fits and the PSD have been computed using the tweezercalib2.1 software package[118](b) Normalizsed autocorrelation functions for a 3s time trace of a trapped particle jumping in and out of a trap at 0.26 mW/μm^2 for trapping (blue) and empty trap (grey) events. The linear fits (orange) are used to extract the relaxation time of the trap.

Figure (4.10) shows $\rho(\kappa_{tot})$ at three different optical intensities for the blue-shifted and resonant regimes. The experimental distributions in both regimes (orange points) are perfectly fit by a normalized sum (black line) of two lognormal distributions (blue and red), revealing two different distributions of κ_{tot}.

A radically different behaviour is observed between these two regimes. In the blue-shifted regime, $\rho(\kappa_{tot})$ is dominated by the red peak at high intensities (>0.6 mW/μm^2). In this situation the particle is highly confined, thus no significant modulation occurs and $\kappa_{tot} \approx \kappa_{opt}$. When the incident intensity decreases to $\approx$ 0.48mW/μm^2, κ_{opt} becomes weaker allowing the particle to explore a wider region of the potential away from the equilibrium position. As a result the overlap of the particle and the cavity mode decreases, blue-shifting the system resonance away from the excitation laser. This further decreases the stiffness of the optical potential and a new peak (blue), corresponding to the modulated potential, appears at lower κ_{tot} values (Fig. 4.10a). Note that in this case κ_{SIBA} is negative ($\kappa_{tot} = \kappa_{opt} + \kappa_{SIBA} < \kappa_{opt}$)

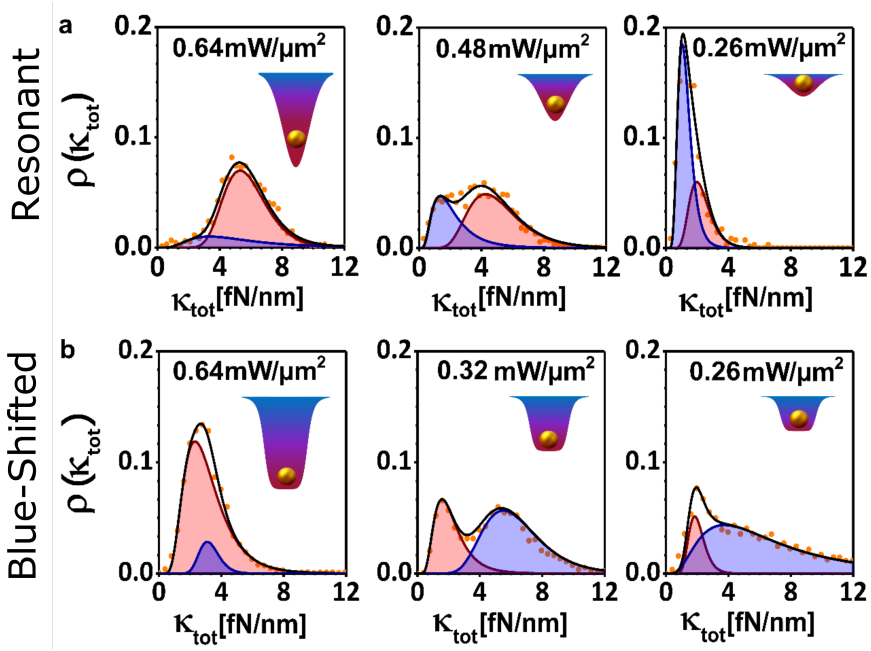

Figure 4.10: Probability distribution of the total stiffness κ_{tot} at different powers. (a) Blue-shifted regime and (b) resonant regime. The experimental distributions (orange dots) are fitted as the sum of two lognormal contributions (black line) at different optical intensities. The red peak represents the stiffness κ_{opt} and the blue peak $\kappa_{opt} + \kappa_{SIBA}$. Each distribution is obtained using between 5000 (higher intensities) and 2000 (lowest intensities) fitted values of τ. Insets show an impression of the GNP behaviour in the modulated potential, where the blue (red) well correspond to the blue (red) peak contributions ofκ_{tot}.

since the amount of photons in the cavity decreases when the particle leaves its centre (c.f. Fig. 4.8a(i)). Finally at low powers the GNP spends most of the time away from the trap equilibrium position as shown by the dominance of the blue peak which suggests that the particle is nearly free diffusing and only weakly trapped. This agrees with the fact that the trapping events last very short times, typically <1s, as seen in Fig. (4.9b). Figure (4.10a) insets illustrate the potential seen by the GNP in the blue-shifted regime. For small displacements from the trap centre (red area) the GNP experiences the restoring constant $\kappa_{tot} \approx \kappa_{opt}$. As it moves further away, the lower restoring constant $\kappa_{tot} = \kappa_{opt} + \kappa_{SIBA}$ reduces the local slope of the potential (blue area).

In the resonant regime, the red peak also dominates at high intensities, where barely no

modulation occurs ($\kappa_{tot} \approx \kappa_{opt}$). However, in this regime, when the laser intensity is lowered and the particle explores a larger region of the nanocavity, the system's resonance blue-shifts towards the laser line. Consequently, more photons couple into the nanocavity, modulating the potential ($\kappa_{tot} = \kappa_{opt} + \kappa_{SIBA}$) and increasing the optical forces that pull back the particle to the centre of the trap. This is demonstrated by the fact that in Fig. (4.10b) the new peak appears at higherκ_{tot} values ($\kappa_{tot} = \kappa_{opt} + \kappa_{SIBA} > \kappa_{tot}$) than the previous peak in Fi.(4.10a). Finally, at very low powers ($\approx 0.26\text{mW/m}^2$), the blue peak dominates and broadens to higher κ_{tot} values due to the larger modulation of the potential. This corresponds to a significant increase in the optical restoring forces, resulting in a more stable trap than in the blue-shifted regime under the same intensities. Figure (4.10b) insets illustrate the potential seen by the GNP in the resonant regime. For small displacements from the trap centre (red area) it experiences the restoring constant $\kappa_{tot} = \kappa_{opt}$t . As it moves further away, the restoring constant $\kappa_{tot} = \kappa_{opt} + \kappa_{SIBA}$ increases the slope of the potential (blue area).

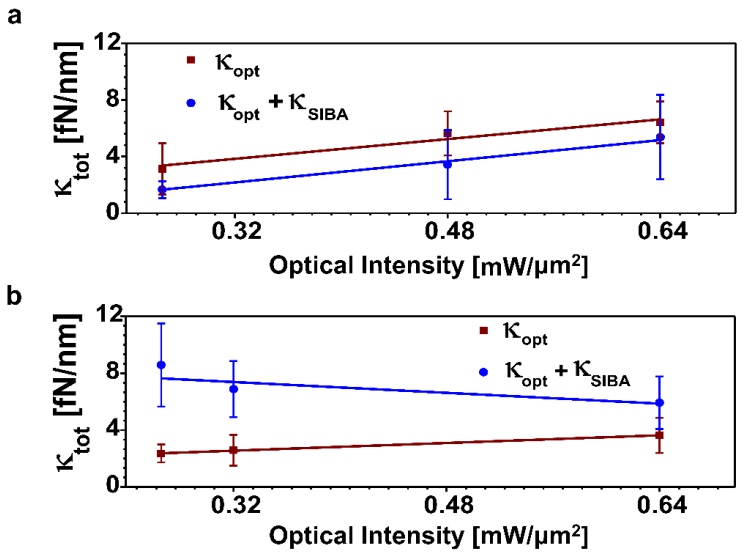

Figure 4.11: Stiffness as a function of the incident optical intensity. (a) For the blue-shifted regime and (b) for the resonant regime. Error bars are computed from the standard deviation in the Lognormal distributions.

To further understand the dependence of the SIBA effect with the optical power, we plot κ_{tot} as a function of the optical intensity for both detuning regimes (Fig. 4.11). In the blue-shifted regime (Fig.4.11a), we see that both κ_{opt} and $\kappa_{opt} + \kappa_{SIBA}$ increase linearly with the

optical excitation power, in agreement with previous observations in this regime[65].
In the resonant regime (Fig. 4.11) κ_{opt} still grows linearly with the intensity, but the $\kappa_{opt} + \kappa_{SIBA}$ contribution becomes inversely proportional to the intensity. This demonstrates that as power is lowered the SIBA effect becomes stronger until it becomes the main trapping mechanism, in agreement with the dominance of the blue peak at low powers in Fig. (4.10). In other words, the relative trapping efficiency of each detuning regime is highly dependent of the optical intensity conditions: at high optical intensities the blue-shifted regime gives a stiffer trap, conversely the resonant regime becomes the most efficient as power decreases reaching a stiffness up to 4 times higher compared to the blue-shifted.

Single photon optomechanical coupling

The single photon optomechanical coupling of the system can be estimated from the experimentally calibrated stiffness and simulated optomechanical coupling strength. For $\kappa_{tot} = 4.51$fN/nm we obtain a mechanical resonance frequency of $\Omega_m = 1.43$ MHz which is an order of magnitude larger than those obtained in the diffraction limited optical traps with dielectric objects presented in chapter 3. This huge increase is both caused by the larger polarizability of gold and the strong gradient of the evanescent field. Combining the resulting $x_{zpf} \approx 3.9pm$ with $G \approx 2\pi \cdot 150$ GHz/nm gives a single photon optomechanical coupling:

$$g_o \approx 2\pi \cdot 580MHz \tag{4.8}$$

This value is $\sim 10^8$ times larger than the $g_o \approx 0.5$ found for our optically levitated particles in a macroscopic Fabry-Perot resonator and it is the largest value of g_o reported in an experiment exceeding by one order of magnitude the strongest coupling rates reported in the literature[116] and by 2 orders of magnitude the rates in photonic crystals[96]. Unfortunately, such large coupling rate is achieved in presence of even higher optical losses from the metal ($g_o/\kappa \ll 1$), which in the end make the system unsuitable for the study of quantum optomechanical effects even if brought to vacuum.

Conclusions and outlook

We have presented an optomechanics approach to optical trapping experiments using plasmonic nano-cavities. This has allowed us to identify the parameters that determine both the optomechanical interaction and trapping performance, which have been optimized by using gold nanoparticles with a high V/V_{mod} ratio. Since the fundamental optomechanical coupling strength G parameter is independent of the system's mechanical dissipation experiments have been performed in a liquid environment to simplify the particle delivery to the nanostructure. Reaching a coupling strength comparable to the optical linewidth $G \sim \Gamma$ has allowed to observe the reconfigurable nature of the optical potential and demonstrate the optomechanical origin of SIBA. We have also assessed the detuning regime that maximizes the trapping efficiency for plasmonic cavities. These results are crucial for trapping and manipulation of objects that are extremely sensitive to photo-damage such as biological samples and fluorescent single emitters.

From the G value and the calibrated optical potential we have obtained unprecedented high values for the single photon optomechanical coupling g_o [8]. Unfortunately the use of plasmonic cavities has also led to a dramatic increase of the optical losses making them unsuitable for the single photon optomechanics regime. Alternatively one could consider engineering nano-cavities with higher optical Q factors using photonic crystals or metals with lower losses such as silver. An improvement by 3 orders of magnitude while maintaining similar coupling rates bring optically trapped particles suitable systems into the single photon optomechanics regime.

Live can only be understood backwards; but it must be lived forwards.

Soren Kierkegaard

5

Conclusions and Outlook

Since Arthur's Ashkin first optical manipulation experiments, optical trapping techniques have allowed to study microscopic systems by probing and exerting forces on them. Along this thesis we have developed and validated new techniques to extend the capabilities of optical trapping experiments to diverse fields, namely non-equilibrium stochastic thermodynamics and cavity optomechanics. In this section we summarise the our conclusions and outlook for the work presented in each chapter:

STOCHASTIC THERMODYNAMICS

In our stochastic thermodynamics experiments we have demonstrated the possibility to use random forces with a Gaussian white noise spectra in order implement an additional thermal bath whose temperature can be tuned up to several thousands of K. By means of different experiments, we have demonstrated that such a thermal bath provides a consistent temperature for both equilibrium and non-equilibrium processes. In one of these experiments we also found the work distribution for isothermal compressions/expansions, which is a rele-

vant thermodynamic process involved in heat engine cycles. Using our approach it is possible to implement arbitrary stiffness vs. temperature (pressure vs. temperature) curves using an optical trap as an analogy of a piston with a single gas molecule, thus allowing to study the efficiency of heat engines in the microscale. Using this same thermal bath approach two experimental heat engines have been recently implemented: a Carnot cycle with a colloidal particle[76] and an Otto cycle with an single ion in a Paul trap[103] both showing unique features not comparable with their macroscopic counterparts. Some recent proposals also suggested to extend the study of thermodynamics with optical traps to the underdamped regime by following a cavity optomechanics approach[32].

We expect that, using the techniques presented in this chapter, it will be possible to implement and test some open questions such as optimal protocols in both overdamped and underdamped regime and in the long term optimize the efficiency of microscopic heat engines in order to bring them from toy models to actual functional devices.

Cavity Optomechanics with levitated nanoparticles

We have presented our efforts in the field of levitated cavity optomechanics to develop an optical trap that couples to a high Finesse cavity to pursue the ground state cooling of a levitated nanoparticle. With this approach we aim to bring together the benefits of two techniques: on the one hand the capability of optical tweezers to maintain optically trapped particles in high vacuum and on the other hand the high cooling rates provided by the optical cavity. Our experiments in the early development stage of the setup have already shown both confinement in high vacuum ($5 \cdot 10^{-6}$ mbar) and coupling to a cavity that provides high enough cooling rates to reach ground state according to our calculations.
These experiments also helped us to find the detection scheme that could reach higher sensitivity in our setup which, in agreement with what has been reported so far in the literature of levitated nanoparticles, is the Backfocal Plane interferometry. With this knowledge we have upgraded the the trap in the setup to bring the system sensitivity closer to resolving ground state.

We also shown that decoupling the trapping and cooling mechanisms allows us to test the influence of experimental imperfections in the cooling performance, resulting in positioning as the most critical parameter.

Besides all the effort put into building a setup to bring a levitated nanoparticle to its motional ground state at room temperature, our experimental configuration also allows to implement further experiments, in particular in the field of thermodynamics. It would be interesting to reproduce the thermodynamic cycles and protocols described in Chapter 2 in the underdamped regime, as the MobOT allows fast and precise modulation of the optical potential. This would not be possible in a setup whose only optical field comes from the cavity, since the bandwidth at which the potential can be modulated is limited by $\gamma_o \approx 25kHz$.

Regarding our Mobile optical trap system, we believe it can be further implemented in levitating nanopartcile systems due to its simplicity, robustness and affordability. Finally, MobOTs also will enable experimental configurations where a levitated nanoparticle is brought close to other objects such as membranes, ions, etc.

Cavity optomechanics with plasmonic nanocavities

We have presented an optomechanics approach to optical trapping experiments using plasmonic nano-cavities. This has allowed us to identify the parameters that determine both the optomechanical interaction and trapping performance, which have been optimized by using gold nanoparticles with a high V/V_{mod} ratio. Since the fundamental optomechanical coupling strength G parameter is independent of the system's mechanical dissipation experiments have been performed in a liquid environment to simplify the particle delivery to the nanostructure.

Reaching a coupling strength comparable to the optical linewidth $G \sim \Gamma$ has allowed to observe the reconfigurable nature of the optical potential and demonstrate the optomechanical origin of SIBA. We have also assessed the detuning regime that maximizes the trapping

efficiency for plasmonic cavities. These results are crucial for trapping and manipulation of objects that are extremely sensitive to photo-damage such as biological samples and fluorescent single emitters.

From the G value and the calibrated optical potential we have obtained unprecedented high values for the single photon optomechanical coupling g_o [8]. Unfortunately the use of plasmonic cavities has also led to a dramatic increase of the optical losses making them unsuitable for the single photon optomechanics regime. Alternatively one could consider engineering nano-cavities with higher optical Q factors using photonic crystals or metals with lower losses such as silver. An improvement by 3 orders of magnitude while maintaining similar coupling rates bring optically trapped particles suitable systems into the single photon optomechanics regime.

References

[1] Abramowitz, M. and Stegun, I. A. (1964). *Handbook of mathematical functions: with formulas, graphs, and mathematical tables*. Number 55. Courier Corporation.

[2] Alemany, A., Mossa, A., Junier, I., and Ritort, F. (2012). Experimental free-energy measurements of kinetic molecular states using fluctuation theorems. *Nature Physics*, 8(9):688–694.

[3] Andrews, D. L. (2011). *Structured light and its applications: An introduction to phase-structured beams and nanoscale optical forces*. Academic Press.

[4] Ashcroft, N. W. (1976). Nd mermin. *Solid state physics*.

[5] Ashkin, A. (1970). Acceleration and trapping of particles by radiation pressure. *Physical review letters*, 24(4):156.

[6] Ashkin, A. (1978). Trapping of atoms by resonance radiation pressure. *Physical Review Letters*, 40(12):729.

[7] Ashkin, A. and Dziedzic, J. (1971). Optical levitation by radiation pressure. *Applied Physics Letters*, 19(8):283–285.

[8] Aspelmeyer, M., Kippenberg, T. J., and Marquardt, F. (2014). Cavity optomechanics. *Reviews of Modern Physics*, 86(4):1391.

[9] Bachor, H.-A. and Ralph, T. C. (2004). *A guide to experiments in quantum optics*. Wiley.

[10] Baker, C., Hease, W., Nguyen, D.-T., Andronico, A., Ducci, S., Leo, G., and Favero, I. (2014). Photoelastic coupling in gallium arsenide optomechanical disk resonators. *Optics express*, 22(12):14072–14086.

[11] Batchelor, G. and Green, J.-T. (1972). The hydrodynamic interaction of two small freely-moving spheres in a linear flow field. *Journal of Fluid Mechanics*, 56(02):375–400.

[12] Beresnev, S. A., Chernyak, V. G., and Fomyagin, G. A. (1990). Motion of a spherical particle in a rarefied gas. Part 2. Drag and thermal polarization. *Journal of Fluid Mechanics*, 219(1):405–421.

[13] Berthelot, J., Aćimović, S., Juan, M., Kreuzer, M., Renger, J., and Quidant, R. (2014). Three-dimensional manipulation with scanning near-field optical nanotweezers. *Nature nanotechnology*.

[14] Bérut, A., Arakelyan, A., Petrosyan, A., Ciliberto, S., Dillenschneider, R., and Lutz, E. (2012). Experimental verification of landauer's principle linking information and thermodynamics. *Nature*, 483(7388):187–189.

[15] Blickle, V. and Bechinger, C. (2012). Realization of a micrometre-sized stochastic heat engine. *Nature Physics*, 8(2):143–146.

[16] Block, S. M., Schnapp, B. J., and Goldstein, L. S. (1990). Bead movement by single kinesin molecules studied with optical tweezers. *Nature*, 348(6299):348.

[17] Bohren, C. F. and Huffman, D. R. (2008). *Absorption and scattering of light by small particles*. John Wiley & Sons.

[18] Born, M. and Wolf, E. (1980). *Principles of optics: electromagnetic theory of propagation, interference and diffraction of light*. Elsevier.

[19] Bose, S., Jacobs, K., and Knight, P. (1997). Preparation of nonclassical states in cavities with a moving mirror. *Physical Review A*, 56(5):4175.

[20] Bosman, M., Zhang, L., Duan, H., Tan, S. F., Nijhuis, C. A., Qiu, C.-W., and Yang, J. K. (2014). Encapsulated annealing: Enhancing the plasmon quality factor in lithographically–defined nanostructures. *Scientific reports*, 4:5537.

[21] Braginsky, V., Vorontsov, Y. I., and Khalili, F. Y. (1977). Quantum features of a ponderomotive meter of electromagnetic energy. *Zhurnal Eksperimentalnoi i Teoreticheskoi Fiziki*, 73(4):1340–1343.

[22] Carnot, S. (1978). *Réflexions sur la puissance motrice du feu*. Number 26. Vrin.

[23] Caves, C. M. (1980). Quantum-mechanical radiation-pressure fluctuations in an interferometer. *Physical Review Letters*, 45(2):75.

[24] Chan, J., Alegre, T. M., Safavi-Naeini, A. H., Hill, J. T., Krause, A., Gröblacher, S., Aspelmeyer, M., and Painter, O. (2011). Laser cooling of a nanomechanical oscillator into its quantum ground state. *Nature*, 478(7367):89–92.

[25] Chang, D. E., Regal, C., Papp, S., Wilson, D., Ye, J., Painter, O., Kimble, H. J., and Zoller, P. (2010a). Cavity opto-mechanics using an optically levitated nanosphere. *Proceedings of the National Academy of Sciences*, 107(3):1005–1010.

[26] Chang, D. E., Regal, C. A., Papp, S. B., Wilson, D. J., Ye, J., Painter, O., Kimble, H. J., and Zoller, P. (2010b). Cavity opto-mechanics using an optically levitated nanosphere. *Proceedings of the National Academy of Sciences*, 107(3):1005–1010.

[27] Clerk, A. A., Devoret, M. H., Girvin, S. M., Marquardt, F., and Schoelkopf, R. J. (2010). Introduction to quantum noise, measurement, and amplification. *Reviews of Modern Physics*, 82(2):1155.

[28] Cohadon, P.-F., Heidmann, A., and Pinard, M. (1999). Cooling of a mirror by radiation pressure. *Physical Review Letters*, 83(16):3174.

[29] Collin, D., Ritort, F., Jarzynski, C., Smith, S. B., Tinoco, I., and Bustamante, C. (2005). Verification of the crooks fluctuation theorem and recovery of rna folding free energies. *Nature*, 437(7056):231–234.

[30] Crooks, G. E. (1999). Entropy production fluctuation theorem and the nonequilibrium work relation for free energy differences. *Physical Review E*, 60(3):2721.

[31] Crooks, G. E. and Jarzynski, C. (2007). Work distribution for the adiabatic compression of a dilute and interacting classical gas. *Physical Review E*, 75(2):021116.

[32] Dechant, A., Kiesel, N., and Lutz, E. (2015). All-optical nanomechanical heat engine. *Physical review letters*, 114(18):183602.

[33] Drever, R., Hall, J. L., Kowalski, F., Hough, J., Ford, G., Munley, A., and Ward, H. (1983). Laser phase and frequency stabilization using an optical resonator. *Applied Physics B*, 31(2):97–105.

[34] Elimelech, M. and O'Melia, C. R. (1990). Effect of electrolyte type on the electrophoretic mobility of polystyrene latex colloids. *Colloids and Surfaces*, 44:165–178.

[35] Evans, D. J. and Searles, D. J. (1994). Equilibrium microstates which generate second law violating steady states. *Physical Review E*, 50(2):1645.

[36] Fabre, C., Pinard, M., Bourzeix, S., Heidmann, A., Giacobino, E., and Reynaud, S. (1994). Quantum-noise reduction using a cavity with a movable mirror. *Physical Review A*, 49(2):1337.

[37] Fonseca, P., Aranas, E., Millen, J., Monteiro, T., and Barker, P. (2016). Nonlinear dynamics and strong cavity cooling of levitated nanoparticles. *Physical review letters*, 117(17):173602.

[38] Gallavotti, G. and Cohen, E. (1995). Dynamical ensembles in nonequilibrium statistical mechanics. *Physical Review Letters*, 74(14):2694.

[39] Gardiner, C. W. et al. (1985). *Handbook of stochastic methods*, volume 3. Springer Berlin.

[40] Garnier, N. and Ciliberto, S. (2005). Nonequilibrium fluctuations in a resistor. *Physical Review E*, 71(6):060101.

[41] Geiselmann, M., Marty, R., De Abajo, F. J. G., and Quidant, R. (2013). Fast optical modulation of the fluorescence from a single nitrogen-vacancy centre. *Nature Physics*, 9(12):785–789.

[42] Geraci, A. A., Papp, S. B., and Kitching, J. (2010). Short-range force detection using optically cooled levitated microspheres. *Physical review letters*, 105(10):101101.

[43] Gieseler, J. (2014). Dynamics of optically levitated nanoparticles in high vacuum.

[44] Gieseler, J., Deutsch, B., Quidant, R., and Novotny, L. (2012). Subkelvin parametric feedback cooling of a laser-trapped nanoparticle. *Physical Review Letters*, 109(10):103603.

[45] Gieseler, J., Quidant, R., Dellago, C., and Novotny, L. (2014). Dynamic relaxation of a levitated nanoparticle from a non-equilibrium steady state. *Nature Nanotechnology*, 9(5):358–364.

[46] Gittes, F. and Schmidt, C. F. (1998). Interference model for back-focal-plane displacement detection in optical tweezers. *Optics letters*, 23(1):7–9.

[47] Glauber, R. J. (1963). Coherent and incoherent states of the radiation field. *Physical Review*, 131(6):2766.

[48] Grigorenko, A., Roberts, N., Dickinson, M., and Zhang, Y. (2008). Nanometric optical tweezers based on nanostructured substrates. *Nature Photonics*, 2(6):365–370.

[49] Gröblacher, S., Hammerer, K., Vanner, M. R., and Aspelmeyer, M. (2009). Observation of strong coupling between a micromechanical resonator and an optical cavity field. *Nature*, 460(7256):724–727.

[50] Hansen, P. M., Tolić-Nørrelykke, I. M., Flyvbjerg, H., and Berg-Sørensen, K. (2006). tweezercalib 2.0: Faster version of matlab package for precise calibration of optical tweezers. *Computer physics communications*, 174(6):518–520.

[51] Hernández, J. V., Kay, E. R., and Leigh, D. A. (2004). A reversible synthetic rotary molecular motor. *Science*, 306(5701):1532–1537.

[52] Jackson, J. D. (1999). *Classical electrodynamics*. Wiley.

[53] Jacobs, K., Tombesi, P., Collett, M., and Walls, D. (1994). Quantum-nondemolition measurement of photon number using radiation pressure. *Physical Review A*, 49(3):1961.

[54] Jain, V., Gieseler, J., Moritz, C., Dellago, C., Quidant, R., and Novotny, L. (2016). Direct measurement of photon recoil from a levitated nanoparticle. *Physical Review Letters*, 116(24):243601.

[55] Jarzynski, C. (1997). Nonequilibrium equality for free energy differences. *Physical Review Letters*, 78(14):2690.

[56] Johnson, P. B. and Christy, R.-W. (1972). Optical constants of the noble metals. *Physical review B*, 6(12):4370.

[57] Jones, P., Maragó, O., and Volpe, G. (2015). *Optical tweezers: Principles and applications*. Cambridge University Press.

[58] Juan, M. L., Gordon, R., Pang, Y., Eftekhari, F., and Quidant, R. (2009). Self-induced back-action optical trapping of dielectric nanoparticles. *Nature Physics*, 5(12):915–919.

[59] Juan, M. L., Righini, M., and Quidant, R. (2011). Plasmon nano-optical tweezers. *Nature Photonics*, 5(6):349–356.

[60] Kepler, J. (1619). De cometis libelli tres.

[61] Kern, W. (2012). *Thin film processes II*, volume 2. Academic press.

[62] Kiesel, N., Blaser, F., Delić, U., Grass, D., Kaltenbaek, R., and Aspelmeyer, M. (2013). Cavity cooling of an optically levitated submicron particle. *Proceedings of the National Academy of Sciences*, 110(35):14180–14185.

[63] Kippenberg, T., Spillane, S., and Vahala, K. (2004). Kerr-nonlinearity optical parametric oscillation in an ultrahigh-q toroid microcavity. *Physical review letters*, 93(8):083904.

[64] Kippenberg, T. J. and Vahala, K. J. (2008). Cavity optomechanics: back-action at the mesoscale. *science*, 321(5893):1172–1176.

[65] Kotnala, A. and Gordon, R. (2014). Quantification of high-efficiency trapping of nanoparticles in a double nanohole optical tweezer. *Nano letters*, 14(2):853–856.

[66] Kuhn, S., Stickler, B. A., Kosloff, A., Patolsky, F., Hornberger, K., Arndt, M., and Millen, J. (2017). Optically driven ultra-stable nanomechanical rotor. *arXiv preprint arXiv:1702.07565*.

[67] Li, T., Kheifets, S., Medellin, D., and Raizen, M. (2010a). Measurement of the instantaneous velocity of a Brownian particle. *Science*, 328(5986):1673–1675.

[68] Li, T., Kheifets, S., Medellin, D., and Raizen, M. G. (2010b). Measurement of the instantaneous velocity of a brownian particle. *Science*, 328(5986):1673–1675.

[69] Lilley, G., Messner, M., and Unterrainer, K. (2015). Improving the quality factor of the localized surface plasmon resonance. *Optical Materials Express*, 5(10):2112–2120.

[70] Lindeberg, J. W. (1922). Eine neue herleitung des exponentialgesetzes in der wahrscheinlichkeitsrechnung. *Mathematische Zeitschrift*, 15(1):211–225.

[71] Malitson, I. (1965). Interspecimen comparison of the refractive index of fused silica*. *Josa*, 55(10):1205–1209.

[72] Mancini, S., Man'ko, V., and Tombesi, P. (1997). Ponderomotive control of quantum macroscopic coherence. *Physical Review A*, 55(4):3042.

[73] Mancini, S. and Tombesi, P. (1994). Quantum noise reduction by radiation pressure. *Physical Review A*, 49(5):4055.

[74] Martínez, I. A., Devailly, C., Petrosyan, A., and Ciliberto, S. (2017a). Energy transfer between colloid via critical interactions. *arXiv preprint arXiv:1701.05914*.

[75] Martínez, I. A., Raj, S., and Petrov, D. (2012). Colored noise in the fluctuations of an extended dna molecule detected by optical trapping. *European Biophysics Journal*, 41(1):99–106.

[76] Martínez, I. A., Roldán, É., Dinis, L., Petrov, D., Parrondo, J. M., and Rica, R. A. (2016). Brownian carnot engine. *Nature physics*, 12(1):67–70.

[77] Martínez, I. A., Roldán, É., Dinis, L., and Rica, R. A. (2017b). Colloidal heat engines: a review. *Soft Matter*, 13(1):22–36.

[78] Martínez, I. A., Roldán, É., Parrondo, J. M., and Petrov, D. (2013). Effective heating to several thousand kelvins of an optically trapped sphere in a liquid. *Physical Review E*, 87(3):032159.

[79] Mazolli, A., Neto, P. M., and Nussenzveig, H. (2003). Theory of trapping forces in optical tweezers. *Proceedings of the Royal Society of London. Series A: Mathematical, Physical and Engineering Sciences*, 459(2040):3021–3041.

[80] Mestres, P., Berthelot, J., Aćimović, S. S., and Quidant, R. (2016). Unraveling the optomechanical nature of plasmonic trapping. *Light: Science & Applications*, 5(7):e16092.

[81] Mestres, P., Berthelot, J., Spasenović, M., Gieseler, J., Novotny, L., and Quidant, R. (2015a). Cooling and manipulation of a levitated nanoparticle with an optical fiber trap. *Applied Physics Letters*, 107(15):151102.

[82] Mestres, P., Berthelot, J., Spasenović, M., Gieseler, J., Novotny, L., and Quidant, R. (2015b). Publisher's note:"cooling and manipulation of a levitated nanoparticle with an optical fiber trap"[appl. phys. lett. 107, 151102 (2015)]. *Applied Physics Letters*, 107(18):189901.

[83] Mestres, P., Martinez, I. A., Ortiz-Ambriz, A., Rica, R. A., and Roldan, E. (2014). Realization of nonequilibrium thermodynamic processes using external colored noise. *Physical Review E*, 90(3):032116.

[84] Mestres, P. and Petrov, D. (2011). Real-time detection of changes in the electrophoretic mobility of a single cell induced by hyperosmotic stress. *European Biophysics Journal*, 40(9):1081–1085.

[85] Metzger, C. H. and Karrai, K. (2004). Cavity cooling of a microlever. *Nature*, 432(7020):1002–1005.

[86] Millen, J., Deesuwan, T., Barker, P., and Anders, J. (2014). Nanoscale temperature measurements using non-equilibrium brownian dynamics of a levitated nanosphere. *Nature Nanotechnology*, 9(6):425–429.

[87] Millen, J., Fonseca, P., Mavrogordatos, T., Monteiro, T., and Barker, P. (2015). Cavity cooling a single charged levitated nanosphere. *Physical review letters*, 114(12):123602.

[88] Neuman, K. C. and Block, S. M. (2004). Optical trapping. *Review of scientific instruments*, 75(9):2787–2809.

[89] Neumeier, L., Quidant, R., and Chang, D. E. (2015). Self-induced back-action optical trapping in nanophotonic systems. *New Journal of Physics*, 17(12):123008.

[90] Novotny, L. and Hecht, B. (2012). *Principles of nano-optics*. Cambridge university press.

[91] Pang, Y. and Gordon, R. (2011). Optical trapping of a single protein. *Nano letters*, 12(1):402–406.

[92] Protter, P., Talay, D., et al. (1997). The euler scheme for lévy driven stochastic differential equations. *The Annals of Probability*, 25(1):393–423.

[93] Ranjit, G., Atherton, D. P., Stutz, J. H., Cunningham, M., and Geraci, A. A. (2015). Attonewton force detection using microspheres in a dual-beam optical trap in high vacuum. *Physical Review A*, 91(5):051805.

[94] Regal, C., Teufel, J., and Lehnert, K. (2008). Measuring nanomechanical motion with a microwave cavity interferometer. *Nature Physics*, 4(7):555–560.

[95] Richards, B. and Wolf, E. (1959). Electromagnetic diffraction in optical systems. ii. structure of the image field in an aplanatic system. In *Proceedings of the Royal Society of London A: Mathematical, Physical and Engineering Sciences*, volume 253, pages 358–379. The Royal Society.

[96] Riedinger, R., Hong, S., Norte, R. A., Slater, J. A., Shang, J., Krause, A. G., Anant, V., Aspelmeyer, M., and Gröblacher, S. (2016). Non-classical correlations between single photons and phonons from a mechanical oscillator. *Nature*, 530(7590):313–316.

[97] Righini, M., Volpe, G., Girard, C., Petrov, D., and Quidant, R. (2008). Surface plasmon optical tweezers: tunable optical manipulation in the femtonewton range. *Physical review letters*, 100(18):186804.

[98] Righini, M., Zelenina, A. S., Girard, C., and Quidant, R. (2007). Parallel and selective trapping in a patterned plasmonic landscape. *Nature Physics*, 3(7):477–480.

[99] Roldán, É., Martínez, I. A., Dinis, L., and Rica, R. A. (2014). Measuring kinetic energy changes in the mesoscale with low acquisition rates. *Applied physics letters*, 104(23):234103.

[100] Roldan, E., Martinez, I. A., Parrondo, J. M., and Petrov, D. (2013). Universal features in the energetics of symmetry breaking. *arXiv preprint arXiv:1310.5518*.

[101] Romero-Isart, O., Juan, M. L., Quidant, R., and Cirac, J. I. (2010a). Toward quantum superposition of living organisms. *New J. Phys.*, 12(3):033015.

[102] Romero-Isart, O., Juan, M. L., Quidant, R., and Cirac, J. I. (2010b). Toward quantum superposition of living organisms. *New Journal of Physics*, 12(3):033015.

[103] Roßnagel, J., Dawkins, S. T., Tolazzi, K. N., Abah, O., Lutz, E., Schmidt-Kaler, F., and Singer, K. (2016). A single-atom heat engine. *Science*, 352(6283):325–329.

[104] Safavi-Naeini, A. H., Chan, J., Hill, J. T., Gröblacher, S., Miao, H., Chen, Y., Aspelmeyer, M., and Painter, O. (2013a). Laser noise in cavity-optomechanical cooling and thermometry. *New Journal of Physics*, 15(3):035007.

[105] Safavi-Naeini, A. H., Gröblacher, S., Hill, J. T., Chan, J., Aspelmeyer, M., and Painter, O. (2013b). Squeezed light from a silicon micromechanical resonator. *Nature*, 500(7461):185–189.

[106] Sakurai, J. J., Tuan, S.-F., and Commins, E. D. (1995). *Modern quantum mechanics, revised edition*. AAPT.

[107] Saleh, B. E., Teich, M. C., and Saleh, B. E. (1991). *Fundamentals of photonics*, volume 22. Wiley New York.

[108] Searles, D. J. and Evans, D. J. (1999). Fluctuation theorem for stochastic systems. *Physical Review E*, 60(1):159.

[109] Seifert, U. (2005). Entropy production along a stochastic trajectory and an integral fluctuation theorem. *Physical review letters*, 95(4):040602.

[110] Seifert, U. (2012). Stochastic thermodynamics, fluctuation theorems and molecular machines. *Reports on Progress in Physics*, 75(12):126001.

[111] Sekimoto, K. (1998). Langevin equation and thermodynamics. *Progress of Theoretical Physics Supplement*, 130:17–27.

[112] Sekimoto, K. (2010). *Stochastic energetics*, volume 799. Springer.

[113] Speck, T. (2011). Work distribution for the driven harmonic oscillator with time-dependent strength: exact solution and slow driving. *Journal of Physics A: Mathematical and Theoretical*, 44(30):305001.

[114] Teufel, J., Donner, T., Castellanos-Beltran, M., Harlow, J., and Lehnert, K. (2009). Nanomechanical motion measured with an imprecision below that at the standard quantum limit. *Nature nanotechnology*, 4(12):820–823.

[115] Teufel, J., Donner, T., Li, D., Harlow, J., Allman, M., Cicak, K., Sirois, A., Whittaker, J. D., Lehnert, K., and Simmonds, R. W. (2011). Sideband cooling of micromechanical motion to the quantum ground state. *Nature*, 475(7356):359–363.

[116] Thijssen, R., Kippenberg, T. J., Polman, A., and Verhagen, E. (2015). Plasmomechanical resonators based on dimer nanoantennas. *Nano letters*, 15(6):3971–3976.

[117] Tipler, P. A. and Mosca, G. (2007). *Physics for scientists and engineers*. Macmillan.

[118] Tolić-Nørrelykke, I. M., Berg-Sørensen, K., and Flyvbjerg, H. (2004). Matlab program for precision calibration of optical tweezers. *Computer physics communications*, 159(3):225–240.

[119] Tonin, M., Bálint, S., Mestres, P., Martìnez, I. A., and Petrov, D. (2010). Electrophoretic mobility of a growing cell studied by photonic force microscope. *Applied Physics Letters*, 97(20):203704.

[120] Toyabe, S., Sagawa, T., Ueda, M., Muneyuki, E., and Sano, M. (2010). Experimental demonstration of information-to-energy conversion and validation of the generalized jarzynski equality. *Nature Physics*, 6(12):988–992.

[121] Uehara, N., Gustafson, E. K., Fejer, M. M., and Byer, R. L. (1997). Modeling of efficient mode-matching and thermal-lensing effect on a laser-beam coupling into a mode-cleaner cavity. In *Photonics West'97*, pages 57–68. International Society for Optics and Photonics.

[122] Vale, R. D. and Milligan, R. A. (2000). The way things move: looking under the hood of molecular motor proteins. *Science*, 288(5463):88–95.

[123] Van Kampen, N. G. (1992). *Stochastic processes in physics and chemistry*, volume 1. Elsevier.

[124] Volpe, G., Quidant, R., Badenes, G., and Petrov, D. (2006). Surface plasmon radiation forces. *Physical review letters*, 96(23):238101.

[125] Vovrosh, J., Rashid, M., Hempston, D., Bateman, J., and Ulbricht, H. (2016). Controlling the motion of a nanoparticle trapped in vacuum. *arXiv preprint arXiv:1603.02917*.

[126] Vuletić, V. and Chu, S. (2000). Laser cooling of atoms, ions, or molecules by coherent scattering. *Physical Review Letters*, 84(17):3787.

[127] Wang, G., Sevick, E. M., Mittag, E., Searles, D. J., and Evans, D. J. (2002). Experimental demonstration of violations of the second law of thermodynamics for small systems and short time scales. *Physical Review Letters*, 89(5):050601.

[128] Wolf, E. (1959). Electromagnetic diffraction in optical systems. i. an integral representation of the image field. In *Proceedings of the Royal Society of London A: Mathematical, Physical and Engineering Sciences*, volume 253, pages 349–357. The Royal Society.

List of Publications

- P. Mestres, J. Berthelot, S. S. Aćimović, R. Quidant
  Unraveling the optomechanical nature of plasmonic trapping.
  Light: Science & Applications 5 (7), e16092, (2016).

- P. Mestres, J. Berthelot, M. Spasenović, J. Gieseler, L. Novotny, R. Quidant.
  Cooling and manipulation of a levitated nanoparticle with an optical fiber trap.
  Applied Physics Letters 107 (15), 151102, (2015).

- P. Mestres, I.A. Martinez, A. Ortiz-Ambriz, R.A. Rica, E. Roldan
  Realization of nonequilibrium thermodynamic processes using external colored noise.
  Physical Review E 90 (3), 032116, (2014).

- E. Marcos, P. Mestres, R. Crehuet
  Crowding induces differences in the diffusion of thermophilic and mesophilic proteins: a new look at neutron scattering results.
  Biophysical journal 101 (11), 2782-2789, (2011).

- V. Méndez, W. Horsthemke, P. Mestres, D. Campos.
  Instabilities of the harmonic oscillator with fluctuating damping.
  Physical Review E 84 (4), 041137, (2011).

- P. Mestres and D. Petrov.
  Real-time detection of changes in the electrophoretic mobility of a single cell induced by hyperosmotic stress.
  European Biophysics Journal, 40(9):1081–1085, (2011).

- M. Tonin, S. Bálint, P. Mestres, I.A. Martìnez, D. Petrov.
  Electrophoretic mobility of a growing cell studied by photonic force microscope.
  Applied Physics Letters 97, 203704, (2010).